ARCHIVES
OF CIVIL AND MECHANICAL
ENGINEERING

Investigation into hybrid abrasive and electrodischarge machining

LUCJAN DĄBROWSKI, MIECZYSŁAW MARCINIAK

Warsaw University of Technology, al. Niepodległości 222, 00-663 Warszawa

The features and the effects of hybrid machining have been described in this paper. The grinding process has been assisted by electric discharges (AEDG – Abrasive Electrodischarge Grinding). The experiments have been performed with the electrodischarge machine tool from the Charmilles Technologies (model FORM - 2LC ZNC), equipped with extra grinding wheel made of metal bond CBN grains and functioning as one of the electrodes put into motion via pneumatic drive. Qualitative assessment of the AEDG has been presented as productivity characteristics and quantitative estimation has been given based on the roughness measurements.

Keywords: *hybrid machining, grinding, EDM, AEDG*

1. Introduction

The investigation is aimed at providing a technological solution for reducing the unfavourable process of gumming the active surface of a grinding wheel as well as easing the metal bond level lowering. The economic criteria responsible for high cost of the ultra-hard abrasives and high operational durability of the CBN grains account for lower grain concentration than required by standards established for conventional grinding wheels. In the active surface of a grinding wheel for the grinding pin presented in Figure 1, average distances between the exposed CBN grains are significantly larger than typical sizes of the grains.

For example, the concentration of the CBS grains in the bond is usually determined as the ten-fold level of the per cent volume share of the abrasive material [1]. Hence, concentration specified as 100 that that in pore-free bond only 10% share of abrasive grains is present in the unit volume of abrasive layer. Assuming uniform distribution of grains typically sized a [μm] in a given volume of abrasive layer, we can calculate average inter-grain distance as $l_z = 2a$ [2]. This distance is almost twice as long as the equivalent distance for standard ceramic tools of the structure number $N = 14$. When the height distribution for the active surface of a grinding wheel grain peaks is taken into account, one can estimate the distance between the active grains as $l_z^{'} > 2a$. In the case of the grinding pins with the wheel diameters ranging from 8 to 10 mm, the high rotational speed setting $n = 1000$ rev/min results in quite low values of $v_s = 5$ m/s. For such a low grinding speed and for the increased distances l_z between grains cutting edges, chips of larger thickness h_{max} are removed on the wheel periphery:

$$h_{\max} = C\, v_f\, l_z'/v_s, \tag{1}$$

where $C = \sin(\phi)$, ϕ is the working angle.

The model mechanism for machined material transport is presented in Figure 2, where isolated singular abrasive grains are fixed in the tool bond. The generated chip is forced into the bond. Its dynamic contact with the bond favours adhesive occlusion thus impairing condition for the chip detachment from the grain surface of attack.
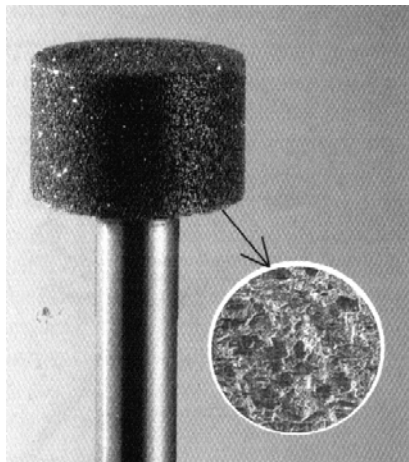

Fig. 1. CBN grinding wheel with metal bond mounted on the grinding pin
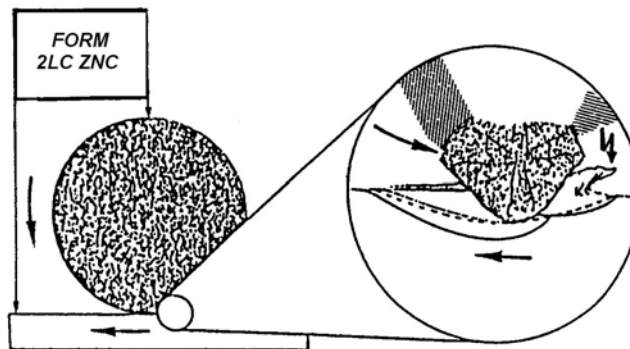and the enlarged active surface fragment with visible grain layout

Fig. 2. Simulation of hybrid micro-cutting and electric erosion within the range of a single cutting grain

When analyzing the course of the process one can conclude that directing concentrated energy flux into face of chip approaching the bond would counteract the AWS gumming by the machined material. Such a kind of effect on material in the machin-

ing zone can be attributed to electric discharges. When comparing momentary electric discharges of $t_e = 10^{-5}–10^{-7}$ s [3] with practically registered times of active grain contacts with machined material $t_k = (3–10)\ 10^{-4}$ s we concluded that average number i of momentary discharges during the chip generation is $i > 1$.

2. Experiments

Figure 3 presents a fragment of working chamber of the electrodischarge machine tool FORM - 2LC ZNC with the extra equipment mounted: pneumatic grinder, grinding pin with CBN wheel and the sample made of bearing steel (Polish type denoted as ŁH15) of Rockwell hardness number 62. The grinder and grinding wheel are fastened to vertical column of the ED machine tool instead of the tool electrode. This unit is connected to the standard machine tool pulse generator along with the part to be machined.
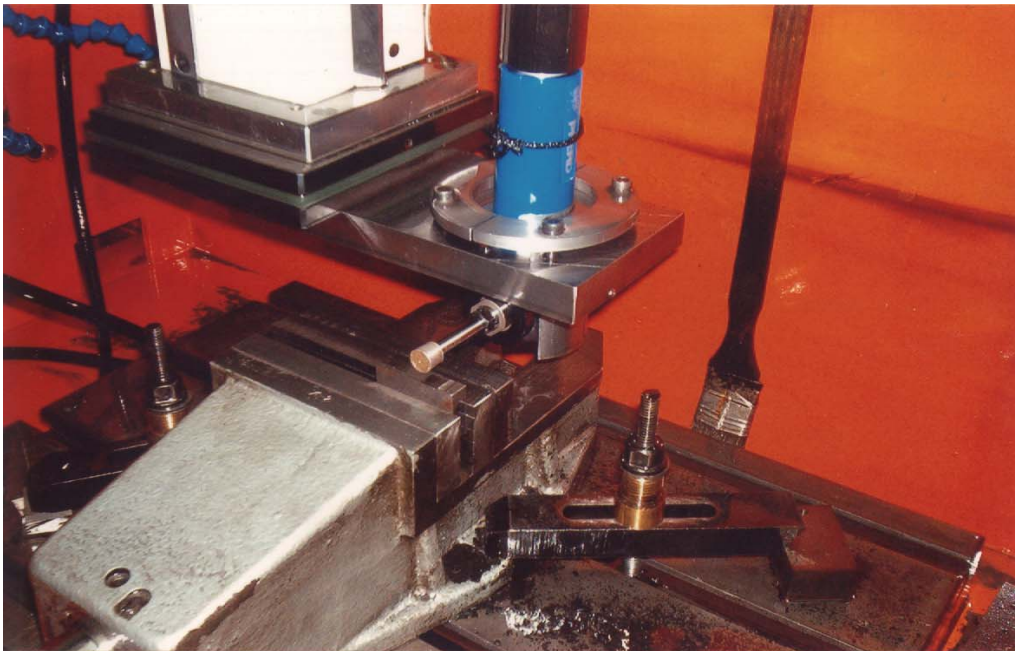

Fig. 3. View of experimental setup for investigating the hybrid
electro-erosion–abrasive machining on the FORM - 2LC ZNC

Two possibilities of supplying power for the electric discharge circuit have been offered by the EDM machine tool generator: RC type and transistor type. The transistor type which was used in the experiments can generate pulses which are not dependent on the spark gap condition and it is featured by wide range of adjustment for dis-

charge time, break time between pulses and amperage. The Box–Benken experimental design, type PS/DS-P, was used for handling the experimental results and three independent variables were selected [4]: amperage I [A], rotational speed of grinding speed v_s [m/s] and feed rate v_f [m/min]. Essential data for three-level experimental plan have been collected in Table 1.

Table 1. Key data for three-level experimental plan

Parameters	Independent variables			Results
	−1	0	+1	
X_1 I [A]	2	4	8	$Ra = f(I, v_s, v_f)$
X_2 v_s [m/s]	1.2	2.5	4.1	
X_3 v_f [m/min]	0.23	0.43	0.86	

Kerosene has been added to the area of machining during conventional and combined abrasive-electrodischarge grinding of flat surface performed according to diagram in Figure 4a. Surface roughness Ra [µm] measurements have been carried out for three zones 1, 2 and 3 on the ground surface of flat specimen as shown in Figure 4b. The linear material removal rate Q_l [mm/min] has been determined based on specimen height changes in predetermined time of grinding.
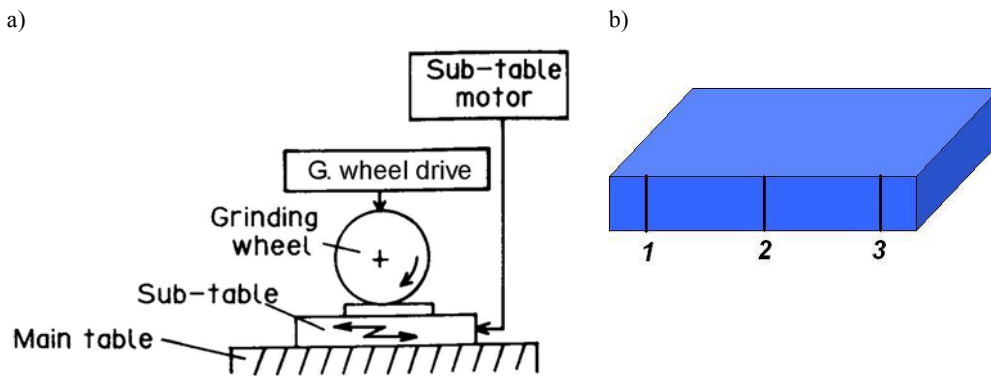

Fig. 4. Longitudinal grinding diagram for flat surface (a), shape of the specimen ground and zones for surface roughness measurements (b)

The averaged surface roughness measurement results for individual points of two-factor experimental design for the values v_s and v_f as shown in Table 1 have been submitted to statistical processing using special multiple regression calculations by computer program REG6M [5]. The influence of machining parameters on the changes of roughness of the surface which was ground without electric discharges is

described by the following regression equation taking form of polynomial with multiple correlation ratio $R = 0.815$ and Fisher value $F = 5.92$ ($F_c = 3.49$):

$$Ra = 2.59 - 0.098 \cdot v_f - 0.067 \cdot v_s \ [\mu m], \tag{2}$$

where: v_f – tangential feed rate, v_s – wheel speed.

The graphical image of Equation (2) is presented in Figure 5 which leads to conclusion that for the applied range v_f and v_s the obtained surface roughness $Ra_{min} = 2.15 \ \mu m$. Due to the influence of increasing feed rate on surface roughness value the sizes of CBN grains belonging to B252 [μm] group were crucial in this case and their increase meant more load on the wheel and a decrease of the back engagement a_p.
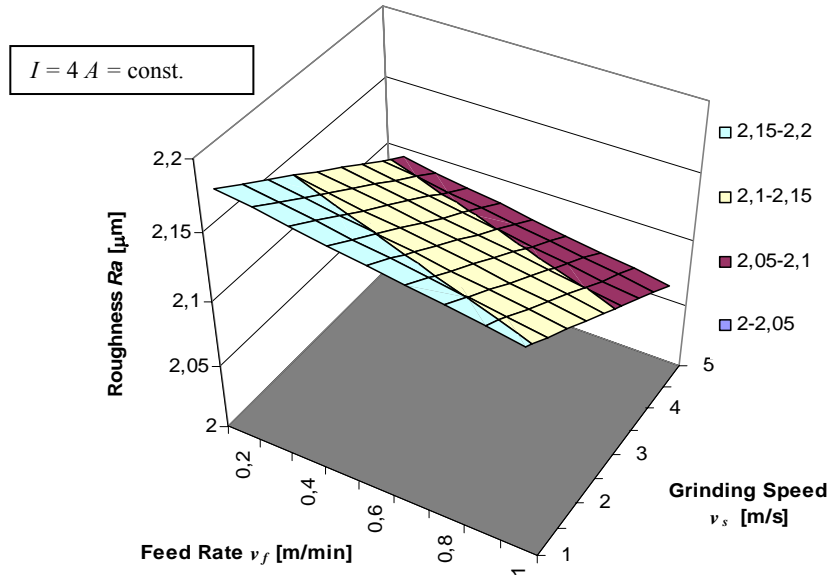

Fig. 5. Influence of grinding parameters v_s, v_f on the surface roughness

Three-dimensional experimental plan has been used for assessing the influence of hybrid grinding on the surface roughness (Table 1). The experimental results have also been statistically processed and the regression equation has been derived (3) with multiple correlation ratio $R = 0.840$ and Fisher value $F = 6.414$ ($F_c = 3.49$)

$$Ra = 1.38 + 0.21 \cdot I - 0.023 \cdot v_s - 0.039 \cdot v_f \ [\mu m]. \tag{3}$$

It can be concluded from Figure 6 that roughness height after grinding process assisted by electroerosion machining with the current I [A] is lower within all investi-

gated range of parameters than surface roughness shown in Figure 5 and its lowest value is $Ra_{min} = 1.50$ μm. Further increase in the current results in an increase of roughness height due to intensive electric erosion in points where discharges take place.
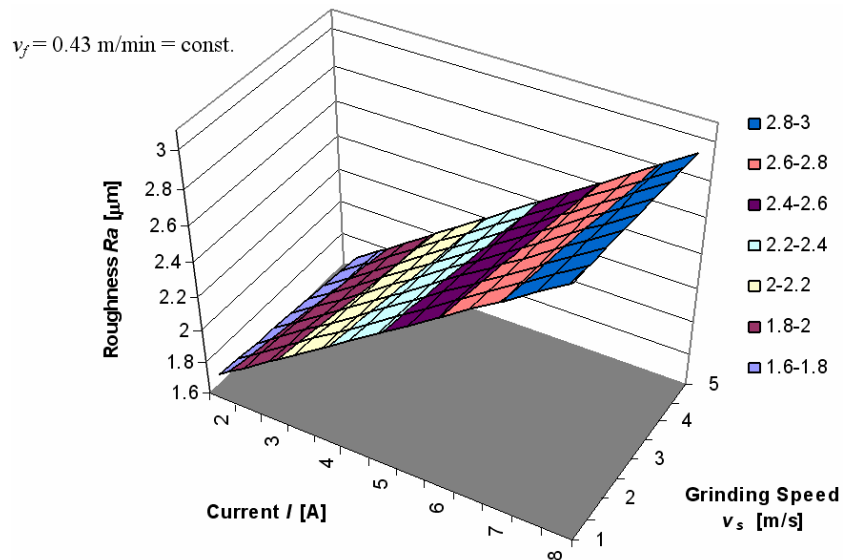

Fig. 6. Influence of the current I [A] and grinding velocity on the surface roughness changes

Table 2 gives the lowest surface roughness Ra_{min} values obtained in the grinding experiments, hybrid grinding (AEDG) and electro-erosion grinding (EDM) obtained for the work electrode shape identical to that used for the CBN grinding wheels.

Table 2. Comparison of the lowest roughness height Ra_{min} values
after three types of machining variety: conventional grinding,
electro-erosion grinding (EDM) and hybrid grinding (AEDG)

Current [A]	0	2	4	8
	Surface roughness Ra [μm]			
Grinding	2.06	–	–	–
EDM	–	3.38	3.46	3.32
AEGD	–	1.40	1.48	2.59

Comparative data presented in Table 2 confirm the prevalence of hybrid machining over both conventional grinding and electrodischarge machining when it comes to lowering the roughness height.

Comparative analysis of linear material removal rate for all machining types clearly demonstrates synergy of mechanical process for material removal and electro-discharge process (Figure 7).
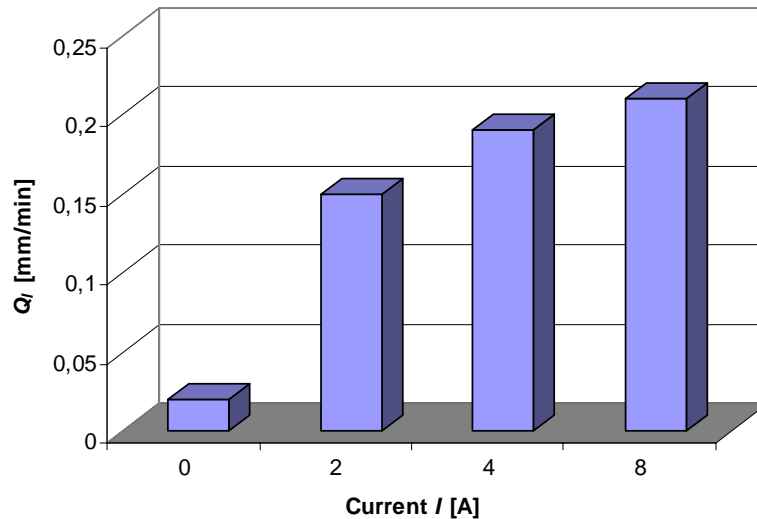
Fig. 7. Comparison of linear productivity for grinding (I = 0 A) and the AEDG (for I = 2, 4, 8 A)

These results are strongest for the AEDG with the current I = 8 A, where linear material removal rate Q_l = 0.21 mm/min and linear material removal rate in the individual impact of the EDM by rotating electrode and of grinding amounted respectively to 0.11 mm/min and 0.02 mm/min which is equivalent to ca. 60% of the hybrid productivity.

3. Summary

The productivity and roughness results obtained in grinding process assisted by the EDM make it possible to conclude that application of this hybrid machining variant is reasonable in the following case:

• allowance removal by hybrid machining,

• surface smoothing by grinding (after the EDM detachment) until the roughness typical of the given grain size of the grinding wheel is obtained.

Design of stands for hybrid machining can be based on the EDM machine tool design and it gives real chance for its industrial application.

References

[1] Oczoś K. E., Porzycki J.: *Szlifowanie*, WNT, Warszawa, 1996.
[2] Marciniak M.: *Proces szlifowania w ujęciu fenomenologicznym*, Prace Naukowe, Mechanika, z. 179, Oficyna Wydawnicza PW, Warszawa, 1999.

[3] Gołąbczak A.: *Metody kształtowania właściwości użytkowych ściernic*, Monografia, Wydawnictwo Politechniki Łódzkiej, Łódź, 2004.

[4] Polański Z.: *Planowanie doświadczeń w technice*, PWN, Warszawa, 1984.

[5] Filipowski R.: *Identyfikacja badanego procesu liniowym równaniem regresji w oparciu o rachunek macierzowy*, Zastosowania matematyki w budowie maszyn, V Ogólnopolskie Seminarium Naukowe, Koszalin, 1994.

Badanie procesu hybrydowej obróbki ścierno-elektroerozyjnej

Przedstawiono charakterystykę i skutki obróbki hybrydowej, w której szlifowanie jest wspomagane wyładowaniami elektrycznymi (*AEDG – Abrasive Electrodischarge Grinding*). Badania przeprowadzono na drążarce elektroerozyjnej firmy Charmilles Technologies (typ FORM-2LC ZNC) wyposażonej dodatkowo w szlifierkę z napędem pneumatycznym ze ściernicą trzpieniową z regularnego azotku boru (CBN) ze spoiwem metalowym jako elektrodą. Ocenę ilościową efektywności obróbki AEGD przedstawiono w postaci wyników badań wydajności, a jakościową – na podstawie pomiarów chropowatości powierzchni.

The effect of transverse forces on creeping buckling of viscoelastic compressed columns

Z. KOWAL

Kielce University of Technology, Al. Tysiąclecia PP 3, 25-314 Kielce

Based on viscoelastic analogy and Laplace's transformation, a constitutive equation for creeping buckling of standard viscoelastic compressed bar model is derived taking into consideration non-dilatational strains. The equation derived is solved and critical bearing capacities as well as creep coefficients of compressed bars of a standard model are determined. The table illustrates time displacements as well as displacement speed and acceleration. The significance of minimal critical bearing capacities and shock specific values with critical characteristics are analyzed.

It is shown the conversion from standard model to the Kelvin–Voight and Maxwell models as well as Timoshenko's elastic model.

Keywords: *creeping buckling, viscoelastic compressed bars, effect of transverse force*

1. Introduction

The viscous properties of steel in the area of effort and operational temperature of building structures are negligibly small. However, at increasing temperature, fire or in the steel structures of skeletal boilers they can be significant.

The polymer-fibre composites offer the greatest variety of viscoelastic materials due to the variety of the physical proprieties of well-known plastics which make up the fibre binders [11]. The rheological features depend on the volume and diameter of fibre in composite. The larger the volume of the fibre in composite, the greater the contact stress concentration in the composite matrix on the surface of fibres [4] and the better elastic properties of composite. The bars properly constructed from fibre composites reinforced with elastic fibres reveal technically unrestricted elasticity [6].

A series connection of the Kelvin–Voigt model and spring are assumed to be a standard model of the viscoelastic quasi-homogeneous material of building material treated as a solid body (Figure 1). This testifies to the occurrence of immediate dislocations in real structural units and in the model, and then to an increase of dislocations with time.

The standard model can be reduced successively to Voigt's and Maxwell's models, and ultimately to the model of an ideally elastic body. The possibility of transforming the temporary stiffness $K(t)$ of the standard model can be easily found by examining the temporary deformation $\varepsilon(t)$ from the formula:

$$\varepsilon(t) = (\sigma/E_1)f(t), \tag{1}$$

where:

$f(t)$ – the function of time,

σ = const.

The temporary deformation of a standard model is as follows [4]:

$$\varepsilon(t) = (\sigma/E_1)f(t), \quad f(t) = 1 + (E_1/E_2)\,[1 - \exp(-E_2\,t/\eta)]. \tag{2}$$

The temporary deformation of the Kelvin–Voigt model will be obtained if we assume $E_1 = \infty$:

$$\varepsilon(t) = (\sigma/E_2)f(t), \quad f(t) = 1 - \exp(-E_2\,t/\eta). \tag{3}$$

The temporary deformation in Maxwell's model will be obtained if we assume $E_2 = 0$:

$$\varepsilon(t) = (\sigma/E_1)f(t), \quad f(t) = 1 + E_1\,t/\eta. \tag{4}$$

Deformation in Hook's elastic model will be obtained by assuming $\eta_3 = 0$, $E_2 = \infty$:

$$\varepsilon(t) = (\sigma/E_1)f(t) = \sigma/E_1, \quad f(t) = 1. \tag{5}$$
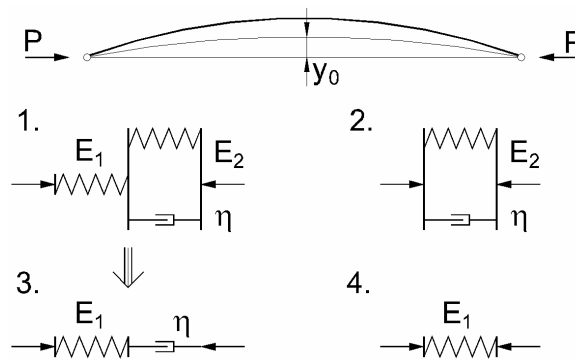

Fig. 1. Conversion from the viscoelastic model of standard solid body to Hook's model

The module of transverse elasticity G of composite bars is many times smaller than the module of longitudinal elasticity E. For example, in wooden poles the quotient E/G is equal to ca. 30. Therefore, the influence of shape deformations on the critical strength of fibre composites cannot be neglected [5]. Timoshenko [10] estimated the influence of transverse forces on critical strength (6) of elastic compressed bars as follows:

$$\sigma_{cr} = \sigma_e G/(\sigma_e + G), \tag{6}$$

where:

$\sigma_e = \omega^2 E i^2 / l^2 = \pi^2 E / \lambda^2$ – the Euler critical strength,

$\lambda = l_w/i = (\pi/\omega) l/i$ – the bar slenderness ratio,

ω – the coefficient dependent on bar boundary conditions.

On the basis of elastic-viscoelastic analogy [1], [8], [9], critical load bearing capacities of axially compressed viscoelastic bars were determined regardless of the effect of non-shape deformation in [2].

The differential equation for creeping buckling of a standard bar model, taking into consideration the effect of shape deformations, has been derived below.

2. Differential equation for creeping buckling

Buckling should be understood here as the displacement concurrent with the change of the equilibrium state from static to movement equilibrium.

Let us write down the well-known [10] differential equation for the buckling of elastic bars taking into account shape deformations:

$$EJy^{IV} - P(EJ/AG)y^{IV} + Py^{II} = 0, \tag{7}$$

where:

EJ – flexural stiffness of section,

AG – transverse stiffness of section.

Relation $EJ/AG = Ei^2/G = d^2$ is constant both in elastic and viscoelastic bars. Then Equation (7) will be written in the following form:

$$EJy^{IV} - Pd^2 y^{IV} + Py^{II} = 0. \tag{8}$$

Based on the theory [8] we know that the sectional moments and forces in elastic and viscoelastic bars are the same if only the load, shape and boundary conditions are identical. The Laplace transformation of Equation (8) versus the time t can be presented as:

$$E(p)JW^{IV}(x, p) - Pd^2 W^{IV}(x, p) + PW^{II}(x, p) = 0, \tag{9}$$

where:

$W(x, p)$ – transform of displacement versus the time t,

p – the symbol of differential operations with time.

The transform $E(p)$ of the conventional elasticity modulus of a standard viscoelastic material model [8] has the form:

$$E(p) = (E_1 p + E_1 E_2/\eta) \, / \, [p + (E_1 + E_2)\,/\eta], \tag{10}$$

where:

E_1, E_2 – moduli of elasticity (Figure 1),

η – the coefficient of viscosity.

Introducing the transform $E(p)$ of a conventional modulus into Equation (9), we can present the transform (9) as:

$$E_1 J p w^{IV} + c J w^{IV} - p P d^2 w^{IV} - b P d^2 w^{IV} + p P w^{II} + b P w^{II} = 0, \tag{11}$$

where:

$b = (E_1 + E_2)\,/\eta,$

$c = E_1 E_2\,/\eta.$

The reciprocal transformation of Equation (11) has the form (12) and is a constitutive equation for creeping buckling of a compressed standard viscoelastic bar:

$$E_1 J \dot{w}^{IV} + c J w^{IV} - P d^2 \dot{w}^{IV} - b P d^2 w^{IV} + P \dot{w}^{II} + b P w^{II} = 0, \tag{12}$$

where:

$w = w(x, t)$ – the temporary displacement,

$\dot{w}$ – the displacement velocity.

Equation (12) can be solved by distributing the variables x and t with the help of function (13):

$$w = y(x)\exp^{(-at)}, \qquad \dot{w} = -ay(x)\exp^{(-at)}, \qquad \dot{w} = a^2 y(x)e^{-at}. \tag{13}$$

A special feature of function (13) is such that for $a > 0$ the transverse displacement y_0 disappears and the bar tends to equilibrium of a straight bar. In the case $a = 0$ for $P = N_{kr}$, the bent bar preserves static equilibrium. In the case $a < 0$, the form of equilibrium is changed into accelerated movement equilibrium.

The differential equation for creeping buckling obtained from (12) is as follows:

$$[J(c - aE_1) + Pd^2\,(a - b)]y^{IV} + P(b - a)y^{II} = 0. \tag{14}$$

It can be reduced to the well-known form:

$$y^{IV} + k^2 y^{II} = 0, \tag{15}$$

where $k^2 = P(a - b)/[J(c - E_1 a) + Pd^2\,(a - b)]$.

The well-known solution of Equation (15) can be presented in the following form:

$$k^2 = \omega^2\,/\,l^2. \tag{16}$$

In solution (16), ω is the coefficient of the Euler elastic critical load bearing capacity dependent on boundary conditions in formula $N_e = \omega^2 EJ/l^2$. From Equation (16) we determine the coefficient a in the function of transverse creep of the viscoelastic model of a bar:

$$a = [\omega^2 cJ - Pb(l^2 + d^2\omega^2)]/[\ \omega^2 E_1 J - P(l^2 + d^2\omega^2)]. \tag{17}$$

After inserting the coefficients b and c into (17) and rearranging it, we obtain the formula for the coefficient of creeping buckling:

$$a = (N_{kr} - P)(E_1 + E_2)/\eta(N_{1kr} - P). \tag{18}$$

Based on formula (18) we arrive at the shock critical load bearing capacity N_{1kr} of creeping buckling:

$$N_{1kr} = \omega^2 E_1 J/(l^2 + d^2\omega^2), \tag{19}$$

and the critical load bearing capacity N_{kr} concurrent with neutral equilibrium in formula (15):

$$N_{kr} = N_{1kr} E_2/(E_1 + E_2). \tag{20}$$

The critical strength of $\sigma_{kr} = N_{kr}/A$ concurrent with neutral equilibrium assumes the form:

$$\sigma_{kr} = \sigma_{1e} E_2 G/(G + \sigma_{1e})(E_1 + E_2), \tag{21}$$

where $\sigma_{1e} = \pi^2 E_1/\lambda^2$.

Creeping buckling occurs under the load P within the following interval:

$$N_{kr} < P < N_{1kr}. \tag{22}$$

Table 1. Examples of the temporary displacement, velocity and acceleration of buckling $a = -0.1$/sec

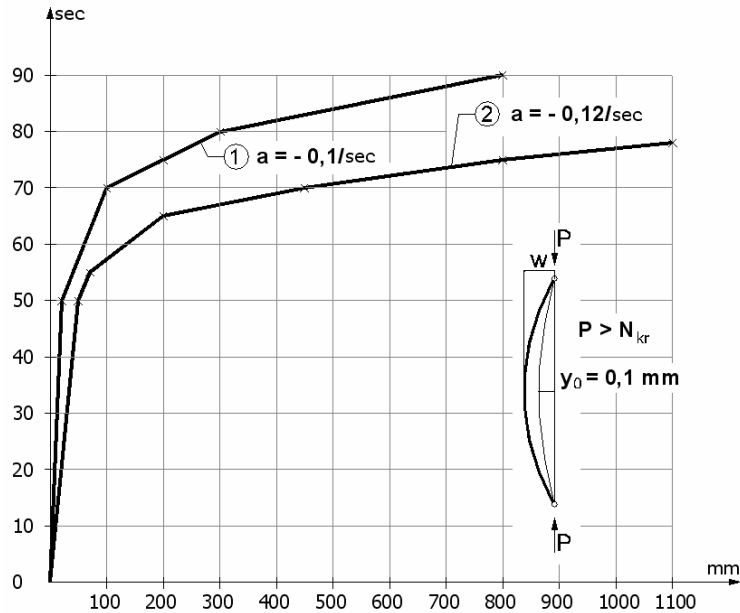| t	0	10	20	30	40	50	60	70	80	sec
w	0.1	0.27	0.74	2	5.46	14.8	40.3	110	298	mm
$\dot{w}$	0.01	0.03	0.074	0.2	0.55	1.48	4.03	11	29.8	mm/sec
$\ddot{w}$	0.001	0.003	0.007	0.02	0.05	0.15	0.4	1.1	2.98	mm/sec^2
$a = -0.12$/sec with influence of transverse forces										
t	0	10	20	30	40	50	60	70		sec
w	0.1	0.33	1.1	3.66	12.2	40.3	134	445		mm
$\dot{w}$	0.012	0.043	0.13	0.44	1.46	4.84	16.1	53.3		mm/sec
$\ddot{w}$	0.0014	0.005	0.076	0.053	0.17	0.58	1.93	6.4		mm/sec^2

Fig. 2. Example of the temporary displacement

Now we shall determine the displacement, velocity and acceleration y_0 of the temporary displacement from formulas (13) assuming that $y(x) = y_0$. In Table 1, we present the examples of the temporary displacement, speed and acceleration of creeping buckling for $y_0 = 0.1$ mm as well as $a = -0.1$/sec and $a = -0.12$/sec.

Figure 2 shows the curves representing of the temporary displacement of creeping buckling. They illustrate the change of creeping speed in the model taking into account the influence of shape deformations on critical load bearing capacity.

3. Estimation of controlled time of reversible creeping buckling

As shown in Figure 2 the controlled creeping displacement of a bar as a function of time is limited to the occurrence of elastic deformations or brittle fracture. After the occurrence of a material limit effort, the process of uncontrolled destruction of a compressed bar begins. The interval of controlled time of creeping buckling after reaching the overload $P > N_{kr}$ constitutes a special warning time permitting us to avoid the catastrophe [7].

3.1. The warning time of overloaded viscoelastic–plastic bars

Let us assume that the material of the bar has a clear yield point R_e and it can be described provisionally by Prandl's model.

The area of reversible creeping buckling as the displacement concurrent with the movement equilibrium will be determined from Equation (23) of the limit critical effort of the section of a compressed bar loaded with axial force contained in the interval (22):

$$\sigma = P/A + Pw_0r/J \leq R_e, \tag{23}$$

where r is the distance of the most strenuous place of intersection from weight axis. Displacement limit w_{gr} is

$$w_{gr} = (R_e A/P - 1)i^2/r, \tag{24}$$

where $i = J/A$ stands for the sectional ray of inertia.

The time of transverse creep t_1 necessary for the beginning of material plasticity or for exceeding the compressive strength will be determined from the transcendental equation

$$w_{gr} = (AR/P - 1)i^2/y_0 = y_0 e^{-at}. \tag{25}$$

The interval of the time of movement necessary for achieving the limit effort R_e of the material of a compressed bar in the most strenuous section can be estimated as follows:

$$t = [\ln(RA/P - 1)i^2/ry_0]/a. \tag{26}$$

Example 1. There is given a bar aroused by transverse displacement $y_0 = 0.005$ and 0.1 mm. The coefficient a of creeping speed is $-0.12/$sec, $AR_e/P = 2$, $i^2/ry_0 = 350$.

The interval of the time of movement necessary for the occurrence of catastrophe under the load $P = AR_e/2$ is:

$$t = \ln[(2-1)350]/0.12 = 5.858/0.12 = 48.8 \text{ sec.}$$

The limit transverse displacement w_{gr} is:

$$w_{gr} = y_0 e^{-at} = 0.1 e^{0.12 \times 48.8} = 35 \text{ mm.}$$

Figure 2 shows limit co-ordinates ($w = 35$ mm, $t = 48.8$ sec) of reversible creeping buckling. In warning time of 48.8 sec, it is theoretically possible to take the load off and to avoid a catastrophe [7].

According to the above mentioned algorithm, we can also estimate the warning time in the case of exceeding the compressive strength R of other models of bars. In mines, overloaded pine stamps, which support the ceiling of the excavation site, generate sound warning signals that allow the miners to escape from danger zone.

3.2. The warning time of overloaded viscoelastic–brittle bars

Let us consider the case of compressed bars of a small compressive strength $R_r < R_s$. In such a case, the time of controlled creeping buckling under load in the interval (22) can be estimated using formulae (28), (28a)

$$\sigma = Pwr/J - P/A \le R. \tag{27}$$

Limit displacement is:

$$w_{\mathrm{gr}} = (RA/P+1)i^2/r = y_0 e^{-at}, \tag{28}$$

the warning interval of time t_1 will be determined from the formula: $w_{\mathrm{gr}}/y_0 = e^{-at}$

$$at = \ln[(RA/P+1)i^2/ry_0]. \tag{28a}$$

Example 2. There is given a compressed bar aroused by transverse displacement $y_0 = 0.005$ and 0.1 mm. An interval of the time of movement between 0 and the occurrence of catastrophe under the load $P = RA/2$ as a result of brittle failure in tensile zone is as follows:

$$t = [\ln(2+1)350]/0.12 = 58 \text{ sec}.$$

The controlled limit displacement w_{gr} is:

$$w_{\mathrm{gr}} = 0.1e^{+0.12 \times 58} = 105 \text{ mm}.$$

4. Transition from a standard model to a smaller model

4.1. The eigenvalues of compressed bar in the Kelvin–Voigt model

If E_1 tends to infinity, then Kelvin's standard model (Figure 1, model 1) tends to Voigt's model (Figure 1, model 2). The critical load bearing capacity of the Kelvin–Voigt bar model, with regard to the influence of transverse forces, can be determined from the transformation of formula (20):

$$N_{\mathrm{kr}} = \omega^2 E_2 J/(l^2 + d^2\omega^2). \tag{29}$$

The critical strength in the Kelvin–Voigt bar model will be determined from the transformation of formula (21) by assuming $E_1 = \infty$:

$$\sigma_{\mathrm{kr}} = \sigma_e G/(\sigma_e + G), \tag{30}$$

where:

$\sigma_e = \pi^2 E_2 / \lambda^2$ – the Euler critical strength,

$\lambda = l_w / i = (\pi/\omega)l/i$.

The difference compared to Timoshenko's solution [10] can be explained by the fact that the critical load bearing capacity (29) and the critical strength (30) in the Kelvin–Voigt model is concurrent with neutral equilibrium, and the creep dislocation occurs under the load P greater than critical load $P > N_{kr}$. However, the critical load bearing capacity according to Timoshenko's model is concurrent with equilibrium bifurcation for $P = N_{kr}$.

The coefficient of the creep speed a under load $P > N_{kr}$ can be determined from the transformation of formula (18):

$$a = (N_{kr} - P)E_2 / N_{kr}\,\eta. \tag{31}$$

Time displacement will be determined as follows:

$$w = y_0 \exp(P - N_{kr})E_2 t / \eta N_{kr}. \tag{32}$$

4.2. The specific values of a compressed bar in Maxwell's model

The transition from the standard model to the creeping buckling of Maxwell's bar model will be obtained from $E_2 = 0$. The coefficient of creep a obtained by the transformation of formula (18) is:

$$a = -PE_1 / (N_{kr} - P)\eta. \tag{33}$$

The eigenvalue N_{kr} that occurs in Equation (33) defining the coefficient of creeping buckling a:

$$N_{kr} = \omega^2 E_1 J / (l^2 + d^2 \omega^2) \tag{34}$$

is not a structural critical load bearing capacity, but a critical eigenvalue which shows at what load bearing capacity a shock buckling will occur. The classic creeping buckling occurs under as small load as $P > 0$ contained in the following interval:

$$0 < P < N_{kr}. \tag{35}$$

Cases of creeping buckling, which are manifested after a long time, occur in engineering when loads are small, $P > 0$, and elastic stiffness of material is high.

4.3. The transition to critical load bearing capacity of Timoshenko's model

The transition to Timoshenko's solution [10] will be obtained by inserting $E_2 = \infty$ and $\eta = 0$ into the standard model. Then the coefficient of creep is equal to zero.

However, the critical load bearing capacity of elastic bar, taking account of the shape deformations, in accordance with Timoshenko's solution, is associated with unstable, bifurcation equilibrium, and assumes the form:

$$N_{1kr} = \omega^2 E_1 J/(l^2 + d^2\omega^2) = N_e GA/(N_e + GA). \tag{36}$$

The critical strength is $\sigma_{kr} = \sigma_e G /(\sigma_e + G)$.

5. Conclusions, remarks and recommendations

In static analysis of compressed bars from natural or artificial composites, it is necessary to take into account the viscoelastic properties of material and time of structure's operational life.

The smallest model of the solid body which permits us to analyse the temporary phenomena occurring in limit states of load bearing capacity and to use the compressed bars in buildings is the three-parameter model referred to as the standard model of a viscoelastic solid body.

The models of viscoelastic bodies better reflect the physical proprieties of many materials and constitute a better basis for the mathematical prognosis of the creeping buckling of compressed bars (columns) in states of limit load bearing capacity. This concerns especially the polymer fibre composites and wood, whose shape stiffness GA and bended stiffness EJ differ significantly.

The significant impact of transverse forces generating shape deformation on critical load bearing capacity and the velocity of creep displacement of composite compressed bars is the greater, the greater the relation E / G.

The model of viscoelastic bodies has also the relevance for the analysis of the stability of compressed steel bars at elevated temperatures, particularly at fire temperatures.

The solution to the problem of creeping buckling of standard model bars with regard to the impact of shape deformations also permits us to determine simply the eigenvalues of the bars in Kelvin–Voigt's model and Maxwell's model as well as the transition to elastic load bearing capacity and Timoshenko's critical load bearing capacity (Hook's model).

References

[1] Alfrey T.: *Non-homogeneous stresses in viscoelastic media*, Quart. Appl. Math., 1944, 2, 113.
[2] Kowal Z.: *Wyboczenie pełzające osiowo ściskanych prętów*, III Sympozjon Poświęcony Reologii, T.1, Wrocław, 1966, 209–218.

[3] Kowal Z., Surkont B.: *Wyznaczanie losowych przemieszczeń i sił wewnętrznych w lepko-sprężystych strukturach przestrzennych*, VII Sympozjon Poświęcony Reologii, Wrocław, 1978, 146–156.

[4] Kowal Z.: *Koncentracja odkształceń i naprężeń stycznych w ściskanych prętach kompozytowych zbrojonych podłużnie włóknem*, Księga Jubil. Prof. Z. Kączkowskiego, Warszawa, 1996, 233–240.

[5] Kowal Z.: *Wpływ sił poprzecznych na nośność krytyczną i pełzanie lepkosprężystych prętów ściskanych*, XLIX Konferencja Naukowa KILiW PAN i KN PZITB, Krynica, 2003, t. II, 65–72.

[6] Kowal Z.: *Doświadczalne wyznaczanie nośności krytycznej kompozytowych prętów ściskanych na podstawie pokrytycznych przemieszczeń*, Przegląd Mechaniczny, 2002, 10.

[7] Krzysik F.: *Nauka o drewnie*, PWN, Warszawa, 1978.

[8] Nowacki W.: *Teoria pełzania*, Arkady, Warszawa, 1963.

[9] Lee E.H.: *Stress analysis in viscoelastic bodies*, Quart. Appl. Math., 1955, 8, 2, 183.

[10] Timoszenko S.P., Gere J.M.: *Teoria stateczności sprężystej*, Arkady, 1963.

[11] Ward J.M.: *Mechaniczne własności polimerów jako tworzyw konstrukcyjnych*, PWN, Warszawa, 1975.

Wpływ sił poprzecznych na wyboczenie pełzające lepkosprężystych prętów ściskanych

Na podstawie analogii sprężysto–lepkosprężystej i transformacji Laplace'a wyprowadzono równania konstytutywne wyboczenia pełzającego lepko–sprężystych prętów ściskanych o modeli standardowym z uwzględnieniem wpływu sił poprzecznych stowarzyszonych z wyboczeniem.

Rozwiązano wyprowadzone równanie konstytutywne i wyznaczono krytyczne wartości własne oraz współczynnik pełzania pozwalający na oszacowanie czasowej drogi, prędkości i przyspieszenia przemieszczeń poprzecznych. Wyznaczono minimalną oraz szokową nośność krytyczną. Pokazano przejścia od modelu standardowego do modelu Kelvina–Voigta, Maxwell'a oraz modelu Timoszenki, który pokazał wpływ sił poprzecznych na nośność krytyczną sprężystych prętów ściskanych.

Optimization of composite materials with cement-fly ash matrix

ALEKSANDER KAPELKO, RAFAŁ KAPELKO

Wrocław University of Technology, Wybrzeże Wyspiańskiego 27, 50-370 Wrocław

This paper analyses the issue of optimization of composite materials – Self-Compacting Concrete with cement–fly ash matrix. The characteristic and experimental testing of Self-Compacting Concrete are presented. The issue of optimization is outlined, the objective function is formulated and preferred solution is calculated, i.e. the point from the set of compromises, the one closest to ideal point, using STATISTICA (polynomial approximations) and MATHCAD (the least squares method) programs.

Keywords: *Self-Compacting Concrete, cement–fly ash matrix, mechanical and physical properties, optimization*

1. Introduction

A modern technology of Self-Compacting Concrete (SCC) has been applied in Poland for several years. Appropriately composed liquid self-compacting mixture has a self-vacuum process ability to compact under self-weight, without the components segregation or bleeding. As a result the mixture tightly fills out formworks or moulds.

It is high fluidity and stability (resistance to segregation) that allows self-compacting of concrete mixture. These properties are obtained by increasing the share of fine aggregate (sand) in aggregate composition, reduction $W/C \leq 0.5$, an increase in the amount of ash mineral supplements (stone dust, fly ash, granulated blast-furnace slag, silica fume) smaller than 80 μm and application of a proper content of high-effective superplasticiser of new generation (polycarboxylic-PC or on the base of polycarboxylic-PE) [1–7]. The content of microfillers along with concrete, meeting the requirements of objective standards, should vary from 500 kg/m^3 to 600 kg/m^3. What is important is the selection of superplasticiser compatible with cement that provides the mixture with the required fluidity, consistence stability and workability. In practice, it is difficult to achieve the mixture stability which is provided by: a) using dust fractions of high capacity, limitation of coarse aggregate and simultaneous reduction of water amount, b) obtaining the value $W/(C+A)$ resulting from required concrete persistence with simultaneous application of admixture increasing the cement paste viscosity [1–5].

This paper analyses the issue of optimization of Self-Compacting Concrete with cement–fly ash matrix with respect to durability of this material in water environment and variability of temperature [8–10].

2. Results and discussion

For the SCC concrete preparation the following components were used: mineral aggregate from Mietków mine (8–16 mm gravel, 2–8 mm gravel and 0–2 mm sand), Portland cement CEM I 52 N from Górażdże Cement Plant, superplasticiser of a new generation – polycarboxylic PC, fly ash VKN and tap water.

The mineral aggregates were experimentally combined in order to obtain an optimum aggregate composition characterized by maximum compactness and by minimum content of water retained by the aggregate [10]. Concrete mixtures with three various contents of cement (C) were prepared: 335 kg/m^3 (M1), 375 kg/m^3 (M2) and 425 kg/m^3(M3). Fly ash VKN (FA) (141 kg/m^3) was applied as the microfiller to all concrete mixtures. The appropriate content of water and superplasticiser (S) (0.93–0.96%) in cement mass was matched fly ash matrix and the aggregates, which ensures the concrete mixture consistency measured by the propagation diameter of the Abrams turned slump flow equal to ~ 68 cm, without components segregation [4, 5, 7, 10, 11]. The variability of $W/(C+FA)$ ratio was: 0.30, 0.32 and 0.34. Density of concrete mixtures ranged from 2260 kg/m^3 to 2290 kg/m^3. The content of coarse aggregate in concrete mixtures ranged from 981 kg/m^3 to 1064 kg/m^3.

The concrete compressive strength (f_c) after 28-day hardening under standard conditions was tested on 15 cubic samples with the side of 150 mm [11]. The tensile splitting strength (f_t) after 28-day hardening was recorded applying Brazilian method (6 cylindrical samples with the diameter and height equal to 160 mm for each type of concrete) [11].

Based on the values of the mean tensile splitting strength (f_{tm}) and the mean compressive strength (f_{cm}), the values of concrete brittleness were calculated. Material brittleness (k) is defined as a ratio of the mean tensile splitting strength of concrete (f_{tm}) to mean compressive strength of concrete (f_{cm}). Materials are considered to be brittle if their $f_{tm}/f_{cm} \leq 0.125$. Brittle materials include ordinary concrete, ceramics, glass and cast iron. The lower the ratio (k), the more brittle the material.

The modulus of elasticity (E_c) was determined for each concrete type based on 3 samples of 113 mm diameter and 300 mm height [6, 10].

The concrete resistance to freezing was tested using the typical method whereby the percentage of samples mass loss (Δm_F) was determined [12].

The test of water absorption (A_w) after 28-day hardening was carried out according to the norm [12].

The test of resistance to water penetration was determined under maximum water pressure of 1.2 MPa using 6 cylindrical specimens of a 300 mm diameter and 150 mm height for each concrete type [10, 12]. The water leakage did not occur. However, the differences in the depths (h_w) of water penetration into the specimen were observed.

The values of the tested properties of SCC concretes are presented in the Table.

Figures 1–3 present histograms of compressive strength for concretes M1, M2 and M3.

Table. The values of SCC concrete properties

Code of concrete mixture	M1	M2	M3
Mean compressive strength, f_{cm} [MPa]	53.7	56.5	63.3
Standard deviation, S_{15} [MPa]	3.3	2.7	4.3
Compressive strength class	C35/45	C40/50	C50/55
Mean tensile splitting strength, f_{tm} [MPa]	2.04	2.93	4.18
Brittleness, $k = f_{tm} / f_{cm}$	0.038	0.052	0.066
Mean modulus of elasticity, E_c [MPa]	33340	34600	36200
Mean mass loss after 150 cycles of freezing/thawing, Δm_F [%]	0.163	0.157	0.138
Mean water absorption, A_w [%]	4.89	4.72	4.56
Mean depth of water penetration under the pressure of 1.2 MPa, h_w [mm]	10	8	7
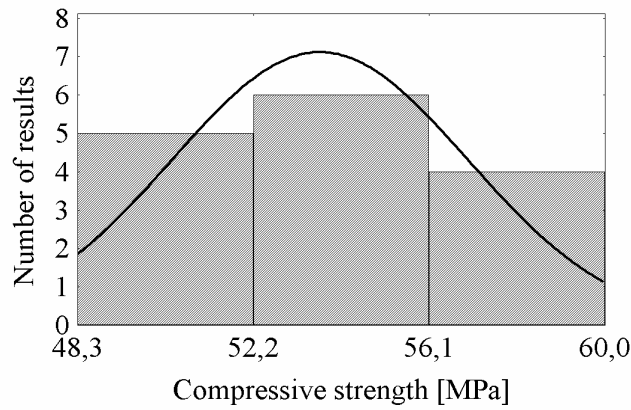
Fig. 1. Histogram of compressive strength of concrete M1
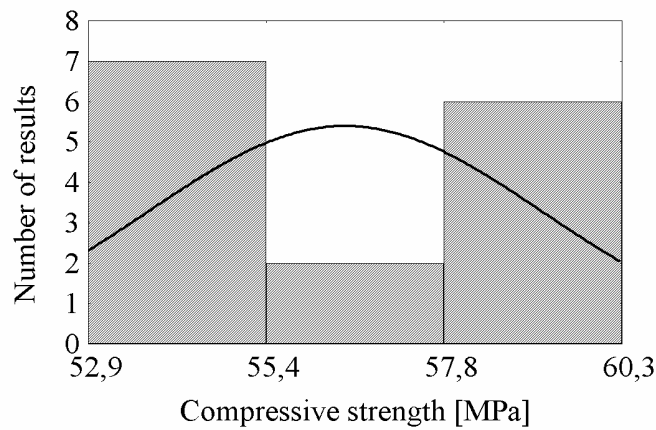
Fig. 2. Histogram of compressive strength of concrete M2
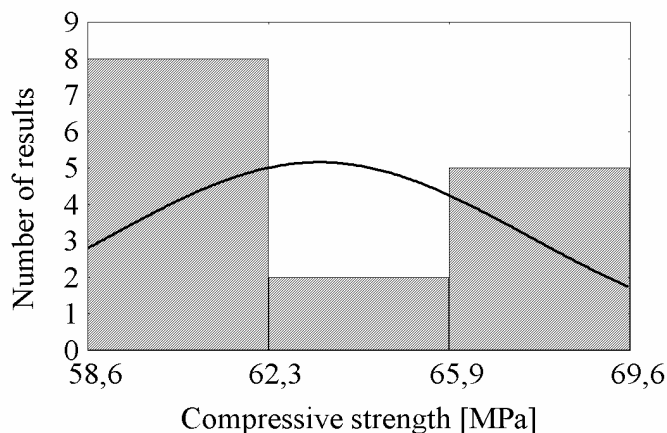
Fig. 3. Histogram of compressive strength of concrete M3

The analysed types of concrete SCC with fly ash matrix are characterised by high quality:

a) compressive strength (f_c) after 28-day hardening corresponds to the compression strength classes ranging from C35/45 to C50/55 [11],

b) water absorption (A_w) is low and in a range of 4.5% – 4.9% [12],

c) mass loss of concrete samples after 150 cycles of freezing and thawing (Δm_F) is very small and varies from 0.14% to 0.16%; according to the norm [12] a mass decrease should not exceed 5% of non-frozen sample mass,

d) concrete modulus of elasticity (E_c) is within the range of 33000 MPa–36000 MPa: the modulus value increases along with the increase of f_c.

e) the water penetration depth (h_w) under the pressure of 1.2 MPa is very small, ranging from 7 mm to 10 mm; this corresponds to the degree of resistance to water penetration $W > W12$ [12].

3. The issue of optimization

The following optimization criteria were considered:

a) maximum compressive strength of concrete : $f_c(x, y) = \max f_c$,

b) maximum tensile splitting strength of concrete : $f_t(x, y) = \max f_t$,

c) maximum modulus of elasticity of concrete: $E_c(x, y) = \max E_c$,

d) maximum resistance of concrete to freezing (denoted as a minimum percentage mass loss Δm_F of specimens after 150 cycles of freezing/thawing): $\Delta m_F(x, y) = \min \Delta m_F$,

e) maximum water absorption of concrete A_w (denoted as a minimum per cent of water absorbed under normal pressure related to the dry mass of specimen): $A_w(x, y) = \min A_w$,

f) maximum resistance to water penetration (water penetration through concrete under pressure) denoted as a minimum specimen penetration by water to under the pressure of 1.2 MPa: $h_w(x, y) = \min h_w$.

Decision variables for the above objective functions are as follows:

- x – share of cement and fly ash ($C+FA$) in concrete mixture (kg/m^3),
- y – W/($C+FA$) ratio i.e. the ratio of water content to cement plus fly ash in concrete mixture.

Decision variables x and y are within the following ranges:

$$476 \text{ kg/m}^3 \leq x \leq 666 \text{ kg/m}^3,$$

$$0.30 \leq y \leq 0.34.$$

The content of both aggregate and admixture in the concrete mixtures was not considered in the functions under analysis. The amounts of these components in the concrete mixtures do not differ significantly and do not influence radically the quality of mixtures and concrete.

4. Formulation of objective functions

The forms of the function from Chapter 3 were obtained as the results of experiments carried out on the basis described in Chapter 2. The analytical forms of the functions: f_c, f_t, E_c, Δm_F, A_w and h_w were approximations of experimental results expressed by polynomials of the second degree in relation to the variables x and y with use of STATISTICA program [13]. The graphical representations of these functions are presented in Figures 4–9.

The extrema of the functions considered were found with MATHCAD program [14]. They are as follows:

$$f_c(x, y) = 257.119 - 0.37\,x - 189.305\,y + 0.0004326\,x^2 - 0.473\,x\,y + 116.337\,y^2,$$

maximum $f_c(x, y)$:

$f_c = 66.95$ MPa for $x = 476 \text{ kg/m}^3$ and $y = 0.30$.

$$f_t(x, y) = 36.916 - 0.035\,x - 56.221\,y + 0.00005463\,x^2 - 0.106\,x\,y + 49.393\,y^2,$$

maximum $f_t(x, y)$:

$f_t = 5.07$ MPa for $x = 476 \text{ kg/m}^3$ and $y = 0.30$.

$$E_c(x, y) = -9784.91 + 181.635\,x - 43086.75\,y - 0.119\,x^2 - 108.126\,x\,y + 1362000\,y^2,$$

maximum $E_c(x, y)$:

$E_c = 36130$ MPa   for $x = 666$ kg /m^3 and $y = 0.30$.

$\Delta m_F(x, y) = -0.125 + 0.0004146\,x + 0.396y - 0.0000006419\,x^2 + 0.001\,x\,y - 0.519y^2$.

minimum $\Delta m_F(x, y)$:

$\Delta m_F = 0.138$ %   for $x = 666$ kg /m^3 and $y = 0.30$.

$A_w(x, y) = -8.827 + 0.017x + 17.835y - 0.00002434\,x^2 + 0.047\,x\,y - 23.038y^2$.

minimum $A_w(x, y)$:

$A_w = 3.74$ %   for $x = 476$ kg /m^3 and $y = 0.30$.

$h_w(x, y) = -91.915 + 0.097x + 161.409y - 0.0001367x^2 + 0.296\,x\,y - 137.447y^2$.

minimum $h_w(x, y)$:

$h_w = 1.6$ mm   for $x = 476$ kg /m^3 and $y = 0.30$.
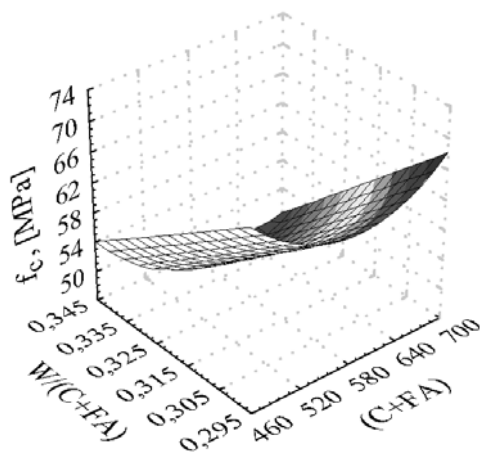
Fig. 4. Variation in compressive strength (f_c) of concrete based on the $W/(C+FA)$ ratio and the content of cement materials ($C+FA$)
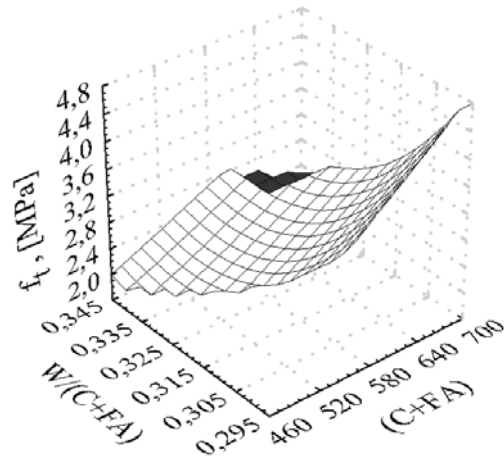
Fig. 5. Variation in tensile splitting strength (f_t) based on the $W/(C+FA)$ ratio and the content of cement materials ($C+FA$)
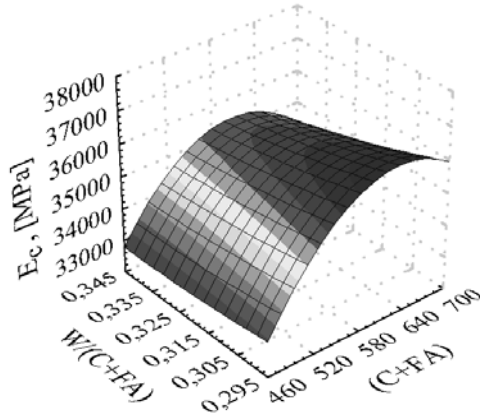
Fig. 6. Variation in modulus of elasticity (E_c) based on the $W/(C+FA)$ ratio and the content of cement materials ($C+FA$)
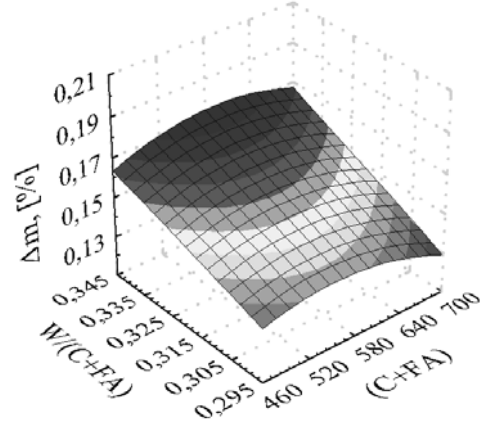

Fig. 7. Variation in mass loss after 150 cycles of freezing/thawing (Δm_F) based on the $W/(C+FA)$ ratio and the content of cement materials ($C+FA$)
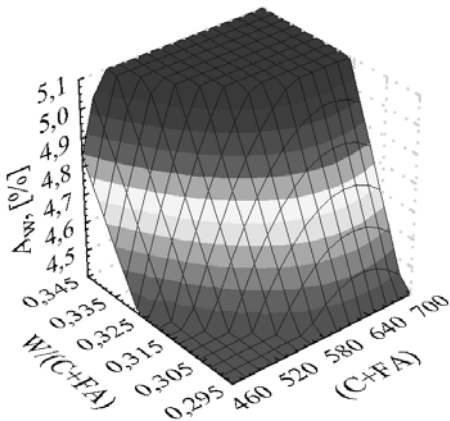

Fig. 8. Variation in water absorption (A_w) based on the $W/(C+FA)$ ratio and the content of cement materials ($C+FA$)
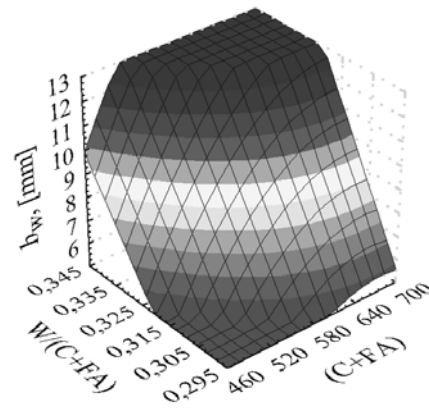

Fig. 9. Variation in water penetration depth under the pressure of 1.2 MPa (h_w) based on the $W/(C+FA)$ ratio and the content of cement materials ($C+FA$)

As the best solution we choose from the set of points the point that is nearest to ideal point. Its coordinates fulfil the following condition (the least squares method):

$$
\begin{aligned}
\Phi(x, y) = {} & [f_c(x, y)/f_c\max - 1]^2 + [f_t(x, y)/f_t\max - 1]^2 + [E_c(x, y)/E_c\max - 1]^2 \\
& + [\Delta m_F(x, y)/\Delta m_F\min - 1]^2 + [A_w(x, y)/A_w\min - 1]^2 + [h_w(x, y)/h_w\min - 1]^2 \\
& = \min \Phi.
\end{aligned}
$$

The solution to the above problem was calculated with MATHCAD program [14]. The solution was as follows:

$$f_c^{\mathrm{pr}} = 66.95 \text{ MPa},$$
$$f_t^{\mathrm{pr}} = 5.07 \text{ MPa},$$
$$E_c^{\mathrm{pr}} = 33600 \text{ MPa},$$
$$\Delta m_F^{\mathrm{pr}} = 0.142\%,$$
$$A_w^{\mathrm{pr}} = 3.74\%,$$
$$h_w^{\mathrm{pr}} = 1.6 \text{ mm}.$$

In the space of decision variables, the best point corresponds to the coordinates:

$$x = 476 \text{ kg/m}^3,$$
$$y = 0.30.$$

5. Conclusions

The solutions presented permit us to formulate the recipe for composite material with cement–fly ash matrix: optimal Self-Compacting Concrete (SCC) made of mineral aggregates from Mietków mine, Portland cement of resistance class 52.5N (CEM I 52.5 N), fly ash VKN, superplasticiser of a new generation and tap water. Optimal concrete SCC implies the greatest compressive strength, tensile splitting strength, modulus of elasticity and resistance to cyclic freezeing/thawing, the lowest water absorption and the greatest resistance to water penetration under pressure. Such a characteristic of the composite allows its durability in water environment and resistance to variable temperatures.

The solution seems to be fully reliable. It confirms intuitive, subjective opinion about examination of many kinds of usual and special concretes and gives the recipe for their composition [7, 10].

The SCC tested is characterised by more advantageous technical parameters if water to cement ratio is low. This was proved in the solution to the issue of SCC concretes optimization.

The assumption accepted in order to formulate the number and character of objective function, the number and character of decision variables and their limitations can be considered as satisfactory.

Solving the problem of optimization of the composition of self-compacting mixtures we did not consider the content of coarse aggregate or the complex aggregate and the quantity of superplasticiser of a new generation (Chapter 3).

It is necessary to determine the content of these components to obtain full recipe. This can be done by establishing the content of aggregate and the quantity of super-

plasticiser on the basis of the experiments and the measurement of concrete mixtures' density ranging from 2260 to 2290 kg/m^3.

The recipe for the self-compacting concrete mixture is the following:

- Portland cement CEM I 52,5 N   – $C = 335$ kg/m^3,
- fly ash VKN   – $FA = 141$ kg/m^3,
- tap water   – $W = 142.8$ kg/m^3,
- $W/(C+ FA) = 0.300$,
- $W/C = 0.430$,
- coarse aggregate (8–16 mm and 2–8 mm gravel) – $A_t = 1008$ kg/m^3,
- complex aggregate (8–16 mm, 2–8 mm gravel, 0–2 mm sand) – $A_c = 1662$ kg/m^3,
- superplasticiser of the newest generation (polycarboxylic (PC)) – $S = 3.12$ kg/m^3 (0.93% in relation to mass of cement),
- density of optimum self-compacting mixture equals 2284 kg/m^3.

The concretes tested are characterized by high compressive strength (compressive strength class from C35/45 to C50/55), low water absorption ($A_w < 5\%$), high resistance to freezing and thawing (degree of freezing/thawing resistance $F >$ F150), shallow water penetration under pressure (degree of resistance to water penetration $W >$ W12) and high modulus of elasticity ($E_c = 3.3 \cdot 10^4$ MPa – $3.6 \cdot 10^4$ MPa).

Self-compacting concretes tested experimentally are useful in freezeing/thawing conditions in exposure classes: XF1, XF2, XF3 [11].

References

[1] Okamura H., Ouchi M.: *Self-Compacting Concrete, Development, Present and Future*, Proc. RILEM Symposium on Self-Compacting Concrete, Stockholm, 1999 September.

[2] Bouzoubaâ N., Lachemi M.: *Self compacting concrete in corporating high-volumes of class F fly ash*: *preliminary results*, Cement and Concrete Research, March 2001,Vol. 31, No. 3, pp. 413–420.

[3] Ma Jianxin, Dietz J.: *Ultra high performance self compacting concrete*, Lacer, 2002, No. 7, pp. 33–42.

[4] XVII and XVIII Conference Materials "JADWISIN 2000" and "JADWISIN 2002", "Concrete and prefabrication", Vol. 2, Popowo, 10–13 April, 2000 and Vol. 1, Popowo, 10–12 April, 2002.

[5] Giergiczny Z., Małolepszy J., Szwabowski J., Śliwiński J.: *Cement with mineral additives in technology of new generation concrete*, Opole, 2002.

[6] Neville A.M.: *Properties of Concrete*, Polski Cement, Kraków, 2000.

[7] Hoła J., Kapelko A., Schabowicz K.: *Non-destructive assessment of the strength of Self-Compacting Concrete*, Technologies for sustainable development in regions, TECHSTA 2004, 4-th International Conference, Prague, 18–20 February, 2004, pp. 113–118.

[8] Brandt A.M.: *Optimization methods applied in material design of composites with cement matrices*, Komitet Inżynierii Lądowej i Wodnej IPPT PAN, Warszawa, 1994.

[9] Konderla P., Mokanek T.: *Comparision of two methods for the analysis of composite material*, Sympozjon *Kompozyty, konstrukcje warstwowe*, Wrocław–Szklarska Poręba,

Polskie Towarzystwo Mechaniki Teoretycznej i Stosowanej – Oddział we Wrocławiu, 2000, pp. 73–82.

[10] Kapelko A., Kapelko R.: *Optimization of composite materials with cement–fly ash matrix*, III Sympozjon *Kompozyty, konstrukcje warstwowe*. Wrocław–Karpacz, Polskie Towarzystwo Mechaniki Teoretycznej i Stosowanej – Oddział we Wrocławiu, 2004, pp. 47–54.

[11] PN-EN 206-1:2003 Concrete – Part 1: *Specification, performance, production and conformity.*

[12] PN-88/B – 06250, *Ordinary concrete.*

[13] Stat Soft, Inc. (1997), STATISTICA for Windows [Computer program manual], Tulsa, USA, WEB: http://www.statsoft.com.

[14] Mathcad User's Guide with Reference Manual Mathcad 2001 Professional, Bagshot, United Kingdom, WEB: http://www.mathsoft.com.

**Optymalizacja materiałów kompozytowych
o matrycy cementowo-popiołowej**

Przedstawiono wyniki badania jakości betonów samozagęszczalnych (SCC) o matrycy cementowo-popiołowej. Badano następujące właściwości betonów: wytrzymałość na ściskanie (f_c), wytrzymałość na rozciąganie (f_t), moduł sprężystości (E_c), nasiąkliwość (A_w), mrozoodporność (F) i wodoszczelność (W) w aspekcie trwałości materiału w środowisku wodnym i w zmiennych temperaturach. Testowane betony charakteryzują się dużą wytrzymałością na ściskanie (odpowiadającą klasom wytrzymałości od C35/45 do C50/55), małą nasiąkliwością ($A_w < 5\%$), dużą odpornością na mróz (stopień mrozoodporności $F > F150$), małą przepuszczalnością wody pod ciśnieniem (stopień wodoszczelności $W > W12$) oraz dużym modułem sprężystości podłużnej ($E_c = 3.3 \cdot 10^4 - 3.6 \cdot 10^4$ MPa).

Badane betony samozagęszczalne są w pełni przydatne do użytkowania w warunkach korozji mrozowej w klasach ekspozycji XF1, XF2, XF3. Na podstawie otrzymanych wyników badań mieszanek betonowych i betonów oraz analizy wyników przeprowadzono optymalizację materiału kompozytowego SCC (*Self-Compacting Concrete*) o matrycy cementowo-popiołowej. Sformułowano zagadnienie optymalizacji i określono postać funkcji celu. Korzystając z programu STATISTICA, otrzymano analityczne postacie funkcji, a ich ekstrema znaleziono, stosując program MATHCAD. Otrzymane rozwiązanie optymalizacji betonu SCC o matrycy cementowo-popiołowej umożliwiło ustalenie receptury samozagęszczalnej mieszanki betonowej.

Principles of surface treatment with high-pressure hybrid jet

P. BORKOWSKI

Technical University of Koszalin, Racławicka 15-17, 75-620 Koszalin

The high-pressure hybrid jet treatment is a new technology that has grown recently in popularity. Such technology is based on a high-pressure abrasive-water jet with addition of dry-ice pellets. Theoretical basis of treatment taking account of the kinetics and thermodynamics of solid particles and their distributions and pressure in hybrid jet is discussed. Based on theoretical results we undertook research in order to explain very complicated and specific erosion mechanism of the surface treated with hybrid jet.

Keywords: *high-pressure hybrid jet, surface treatment*

Nomenclature

c, c_s – specific heat and sublimation heat of ice, respectively,
d – diameter of a spherical grain model,
m – solid particle weight,
n – flow rate of solid particles,
p – water pressure,
r – radius of a spherical grain model,
t_1, t_2 – time of ice particle flow during pneumatic and water jet transportation,
u – water jet velocity, $u = (2p/\rho)^{0.5}$,
v – solid particle velocity in a stream,
w – coefficient of multiplying gas–solid CO_2 volume,
z – coefficient of volume of sublimated ice pellets,
C_D – coefficient of hydrodynamic drag,
D_o – jet diameter at a sprinkler outlet,
D_x – jet diameter under consideration,
E_k – kinetic energy of solid particle,
K – constant, $K = (8r\rho):(3C_D\rho_w)$,
L – length of suction hose,
L_s – stand-off distance,
L_T – length of sprinkler tube,
S – surface of ice particles,
T_a, T_w – temperature of air and water, respectively,
T_i, T_{ie} – initial and final ice temperature, respectively,
V – volume of dry-ice particle,
V_g – gaseous CO_2 volume in sublimation process,
α_1, α_2 – coefficient of heat absorption from ice particle during pneumatic and water jet transportation,
δ – effectiveness of sublimation process,

η – coefficient of jet efficiency,
ρ, ρ_w – solid particle density and water density, respectively.

1. Introduction

Surface treatment using a high-pressure hybrid water-abrasive-ice jet consists in bulk microtreating the surface with abrasive grains and ice particles transported by a water jet. Due to a high rate of this jet, often aerated to a considerable degree, the solid particles are adequately supplied with energy necessary to perform a treatment operation. A number of the surface processing technologies based on the above principle have been previously suggested. Another, the adoption of the ice jet technology is based on the adequate proportion of abrasive and ice particles characterized by specific usable properties.

The first component of that hybrid jet, i.e. abrasive grains, has been used for almost a quarter of century as an abrasive water jet and for this reason it is well known [6, 12, 25, 29]. A noticeable interest in high-pressure cryogenic jets [9, 19, 22, 30], abrasive-cryogenic jets [5, 14, 18] and ice jets [2, 15] has been aroused in recent years. A high-pressure ice jet is created by ice particles driven by a stream of air [16, 17], other gas or water [10, 11] displaced with a great velocity. Ice particles for such jets are produced by freezing the water droplets [20] or by crushing larger ice particles [21, 27] or are obtained from dry ice pellets [28]. This technology of ice generation has been widespread lately. Usually dry-ice pellets are accelerated by compressed air, hence, the components of this ice jet escape into the atmosphere leaving only the particles of disposable impurities. In such conditions, the sublimation of gaseous CO_2 has no influence on erosion mechanism. When a surface is subjected to hybrid jet treatment, in which a stream of water is an acceleration medium, such a sublimation process is of a great importance [4].

It is possible to increase the efficiency of surface treatment with a hybrid jet including dry-ice pellets, which is of a great importance, especially when fairly hard impurities are to be disposed of. Thus, this paper is devoted to physical basis of a high-pressure hybrid water-abrasive-ice jet.

2. Kinetics of high-pressure water-ice jet

In order to create a high-pressure hybrid water-abrasive-ice jet of high-quality erosion properties, it is necessary to know the solid particle behaviour. Therefore the velocity of abrasive and ice particles in the sprinkler outlet, especially in the erosion area, and their kinetic energy have to be known.

Kinetic energy (E_K) of abrasive and ice particles in the erosion zone can be calculated from the following expression:

$$E_K = \frac{2}{3}\pi \cdot r^3 \rho_0 v^2 .$$

(1)

Under steady-state conditions of fluid flow, the thrust force of a jet counterbalances the aerodynamic resistance of ice particles causing its acceleration. On that basis [2, 9] it is possible to derive expression describing the maximum velocity of particles in a steady-state jet:

$$v = \left(\frac{u^2 t}{ut + K} \right) \cdot \left(\frac{D_0}{D_x} \right)^2 \eta \, . \tag{2}$$

Evaluation of D_0, D_x, η from formula (2) can exclusively be made by experimental method [9, 13].

Diagrams of kinetic energy for abrasive and ice particles in the erosion area being 250 mm distant from the sprinkler tube outlet are presented in Figure 1. As shown in this figure, an increase in the sprinkler tube length and in the water pressure causes substantial increase in the kinetic energy of abrasive and ice particles. The above results revealed that for different dimensions of abrasive grains (SiO_2 #60) and dry-ice pellets and thus for their different density, the kinetic energy of dry ice pellets is 300–500 times higher than that of abrasive particles.
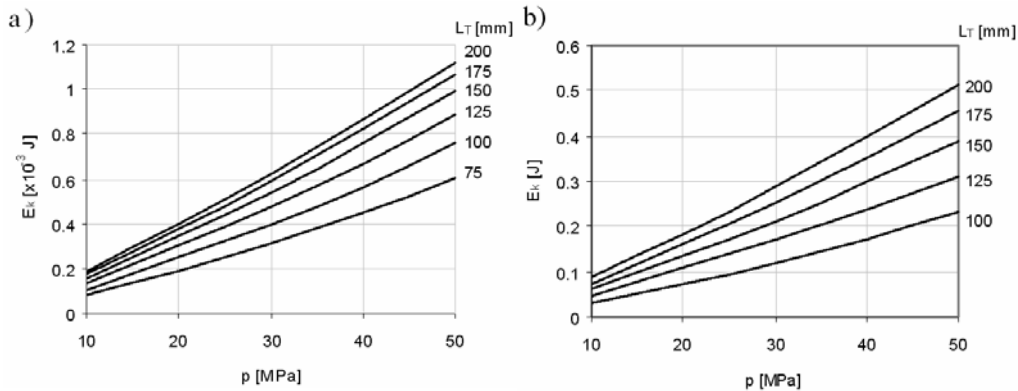

Fig. 1. Influence of the sprinkler tube length and the water pressure on the kinetic energy of solid particles carried by jet of 10% water content: a – sand quartz #36, b – dry-ice pellets

3. Final temperature of dry-ice particles

In order to evaluate the suitability of ice particles for cleaning, first of all one has to get to know a temperature which they have at respective stages of the process creating the water-abrasive-ice jets.

To derive the equation allowing calculating the final temperature of ice particles on the basis of the well known Newton's heat equation, the energy balance should be drawn up. After transformation of the energy balance and calculation of final tem-

perature of ice particles that undervent "heating up" by air during their transport from a container to a sprinkler and then with high-pressure water jet, it is possible to derive [7, 8] the following equation:

$$T_{ie} = T_w - \left[(T_w - T_a) + (T_a - T_i) \cdot e^{\frac{-\alpha_1 S}{c\rho V} t_1} \right] \cdot e^{\frac{-\alpha_2 S}{c\rho V} t_2} . \tag{3}$$

Taking Equation (3) into consideration a series of calculation of thermodynamical states of ice particles were made which enabled us to determine suitability of ice particles for the process of cleaning as is shown in Figure 2.
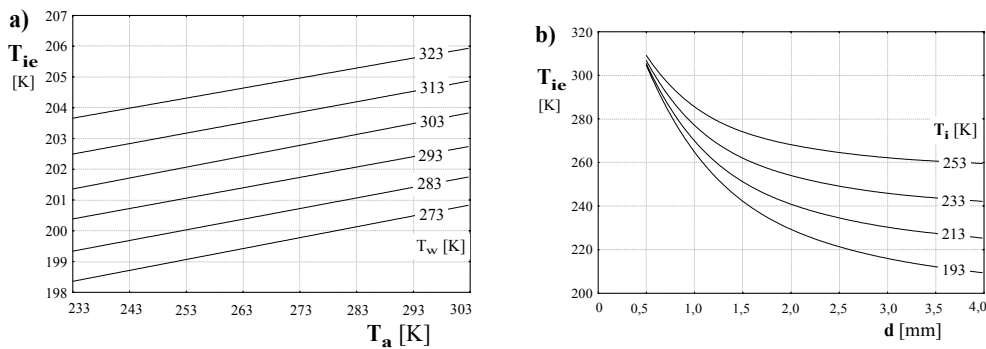
Fig. 2. Final temperature of dry-ice pellets vs. temperature of air and water (a), initial ice temperature and ice particles diameter (b). Work conditions: $p = 20$ MPa, $L = 5$ m, $L_s = 250$ mm

Based on the analysis of Figure 2 one can state that an initial temperature of ice particles is considered to be the factor whose effect on a final temperature of ice particle is the strongest. The next factors affecting considerably a final temperature of ice particle are their sizes and the distance from a water-ice jet outlet to a sprinkler tube and the workpiece. A slighter influence on the final temperature exerts a temperature of water and next the water pressure which affects a jet rate and therefore the time of "heating up" the ice particles. The final temperature of ice is slightly influenced by a temperature of air, and the slightest effect has the length of a suction pipe.

4. Sublimation effect of ice particles

Dry ice pellets accelerated in a high-pressure water jet collide with each other and with internal surfaces of pipes and a sprinkler and are impinged by abrasive grains as well. Due to all these collisions dry ice pellets undergo a partial sublimation, and therefore such a high-pressure hybrid jet "smokes" with gaseous CO_2. However, the most intensive sublimation of dry ice pellets occurs in an erosion zone because of their

collision with the working surface. Thus, a severe deformation of ice pellets or their disintegration is responsible for their very rapid sublimation, usually nearly explosive in character. This process is so impetous because the volume of gaseous CO_2 is 800 times larger compared to its volume in dry ice pellets [2, 4].

Considering this specific character of the ductile impingement of dry ice pellets onto the working surface one can assume that kinetic energy of these pellets is totally transformed into the energy of the ice sublimation. That makes it possible to determine the volume of sublimated dry-ice pellets during such collisions. It is expressed by the following relation:

$$z = \frac{E_k}{c_s m}.$$ (4)

Based on Equation (4), it was found that depending on the pressure of water the volume of dry-ice pellets was sublimated in 1.4–7.3% [1]. Then, the volume of gaseous CO_2 obtained from the sublimated dry-ice pellets is expressed by the following formula:

$$V_g = \frac{V E_k}{c_s m} \delta \cdot w.$$ (5)

The results of calculations made on the basis of the above relation are presented in Figure 3. Such a great volume of gaseous CO_2 generated rapidly in the area of contact of dry-ice pellets with the working surface produces a very dynamic increase in the gas pressure. This allows the cracks in the surface layer of the workpiece to grow and disrupt.
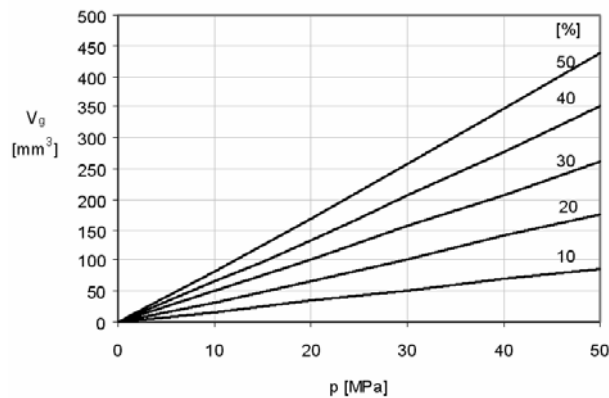

Fig. 3. Gaseous volume of dry-ice pellets sublimation vs. water pressure
and effectiveness of sublimation process

5. Pressure distribution in a jet

The structure of a high-pressure water jet depends on total pressure [23] and abrasive grain distribution [24]. The research of the water jet pressure distribution was carried out using a special piezoelectric dynamometer [3, 13].
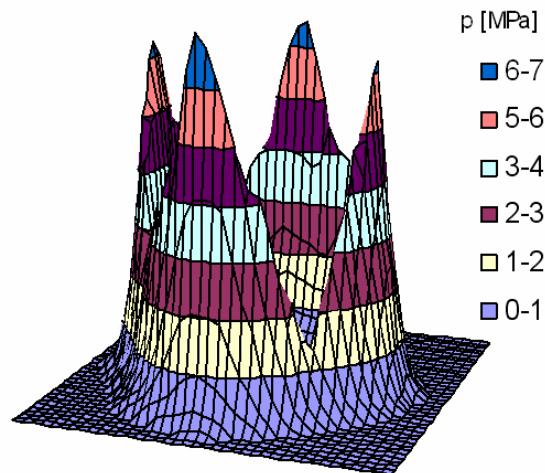

Fig. 4. Total pressure distribution in hybrid jet. Spray gun equipped with 4-hole nozzle. Working conditions: $p_n = 25$ MPa, sand quartz #36, dry-ice pellets, $L_s = 400$ mm

The high-pressure hybrid abrasive-ice-water jet forms a coating in the shape of a tube with significantly increased water concentration in its external layers. The spatial pressure distribution (Figure 4) shows distinct preferred directions characterized by the highest pressure of the hybrid water jets. The number of such elementary jets is equal to the number of water holes arranged in sprinkler nozzles. A few times lower pressure prevails between these preferred directions in external layers of the jet. However, the definitely lowest pressure occurs in internal layers of hybrid abrasive-ice water jets.

6. Distribution of solid particles in a jet

The second very important factor that determines the high-pressure hybrid jet structure is the distribution of abrasive and ice particles. The abrasive grain distribution in a cross-section of the jet was examined by an adequate counting of scratches made by grains remaining on the workpiece surface treated with the abrasive-water jet. This is the latest ten-circular stratified-cellular method [6], which is an updated version of the previous ten-circular stratified method [24] developed by Mazurkiewicz et al., and its improvement is presented in [13].
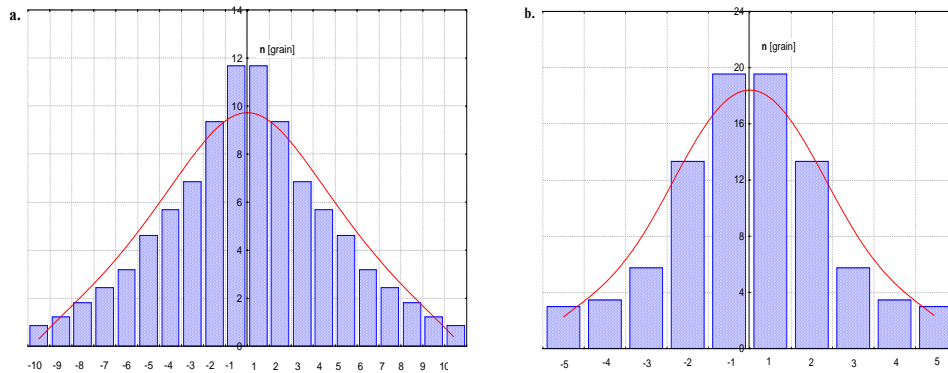
Fig. 5. The distribution of a abrasive grains (a) and ice particles (b) in the hybrid jet created in 4-hole concentric nozzle. Working conditions: $p = 25$ MPa, sand quartz #36, dry-ice pellets

Some examples of experimental results are shown in Figure 5. It is seen from these spatial plots that the highest number of abrasive grains flow along the axis of an abrasive-water jet, where the lowest total pressure prevails. On increasing the distance from the axis, the flow rate of abrasive grains was decreased. The lowest number of grains were in the external jet layers, where the highest pressure prevailed. Definitely, the highest density of solid particles distribution is characteristic of the internal layers of a hybrid jet, where the water pressure is the lowest. It was also confirmed that an increase in the number of water holes in a sprinkler nozzle leads to an increase in flow rates of solid particles.

However, taking into consideration the size of ice particles, their number is considerably smaller than that of abrasive particles. For example, in practical conditions of a hybrid jet formation, the consumption of abrasive grains is 100 kg/h and consumption of dry-ice particles reaches 150 kg/h. In such conditions, one ice grain erosion is accompanied by approximately 70 abrasive grains. Therefore the above proportions are important for treatment mechanism.

7. Mechanism of surface treatment

Analyses of the interaction between the abrasive-ice grains and workpiece should be carried out taking account of the fact that the total jet pressure and the flow rate of such grains exert the strongest influence on the errosiveness of a hybrid jet. Thus, the abrasive and ice jet distribution determines the performance and quality of surface treatment. A high pressure prevailing in external layers of hybrid jet, despite a low concentration of solid particles, is responsible for intensive treatment of material surfaces. Then, the internal jet layers caused the eroded surface to become smooth marking a great number of small scratches made by solid particles at the lowest pressure.

The effects of steel sheet surface shaping using high-pressure hybrid jet presented in the form of geometrical surface structure images (SSG) [26] are shown in Figure 6. Outer image of such a surface is presented in Figure 6a, while its view above average surface is shown in Figure 6b. The image with cut-off surface is given in Figure 6c, while traces of pits are presented in Figure 6d, showing those pits in the form of up-lifted 'negative' image reverse. Sharp edges of these pits confirm the assumption that material cracks and gaps are due to impingements of abrasive grains. In consequence of all those collisions, cracks are wedging off in the form of water shock wave as an effect of violent sublimation of ice pellets. This causes that this hybrid jet treatment mechanism is very complicated and requires explanation.
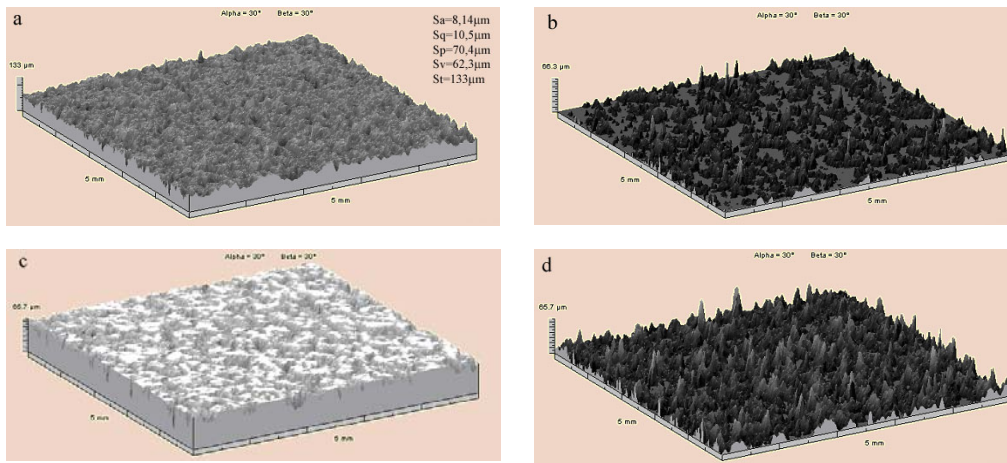

Fig. 6. Examples of geometrical surface (St3S steel) structure (SSG) treatment with hybrid jet (p = 30 MPa): a – a general SSG view, b – view of top outer surface layer, c – view of bottom surface layer showing pits, d – negative view of pit's size and shape

Details of the surface treated with high-pressure hybrid jet comprising abrasive grains and ice particles are shown in SEM micrographs (Figure 7). Abrasive grains impinging on the surface cause erosion of small chips (Figure 7a) resulting in numerous pits and cracks. Besides, the ice particles impinge on a great area, but their impact on the surface is significantly milder than that of abrasive grains. These ice grains partially sublimate producing a great volume of condensed gaseous CO_2 that penetrates violently the cracks. Such an explosive influence of ice gaseous CO_2 and water drops affects the growth of small cracks and sometimes even tear out new chips (Figure 7 b). Because of the above the treatment mechanism is very complicated.

It was found on the basis of a thorough analysis of the process of erosion on the surface treated with a high-pressure hybrid water-abrasive-ice jet that the physical mechanism of the treatment was very complicated and specific. A simplified version of such a model of erosion is illustrated in Figure 8. It was revealed that the a big dry-

ice pellet 1 impinging onto the working surface 2 makes it deformed squeezing out the flashes 3 around the crater. This great caving includes a huge number of marks 4 produced by relatively fine abrasive grains. This impingement made the part of the dry-ice pellets undergo the sublimation and generate the gaseous CO_2 of the volume 800 times larger. Due to the explosive character of the generation of that gas, the cracks and gaps 5 were growing under the influence of previous collisions of abrasive grains. Consequently, the particles 6 detached from the workpiece took the form of new characteristic chips (Figure 7b).
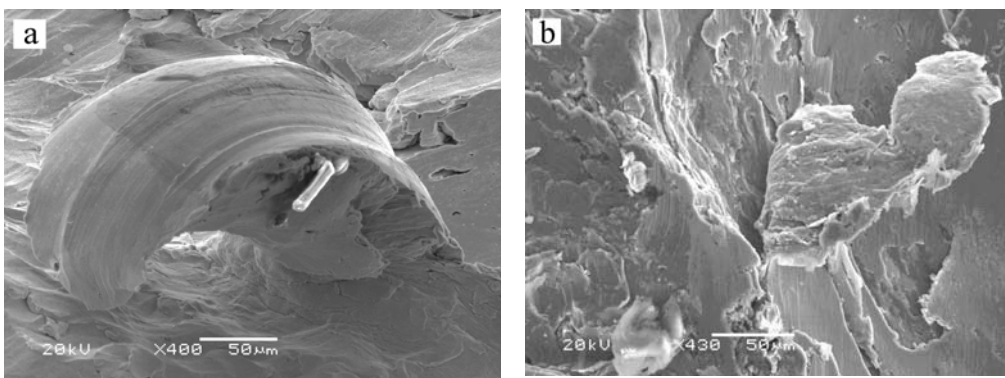
Fig. 7. Surface of the brass treated with high-pressure hybrid jet with exposed:
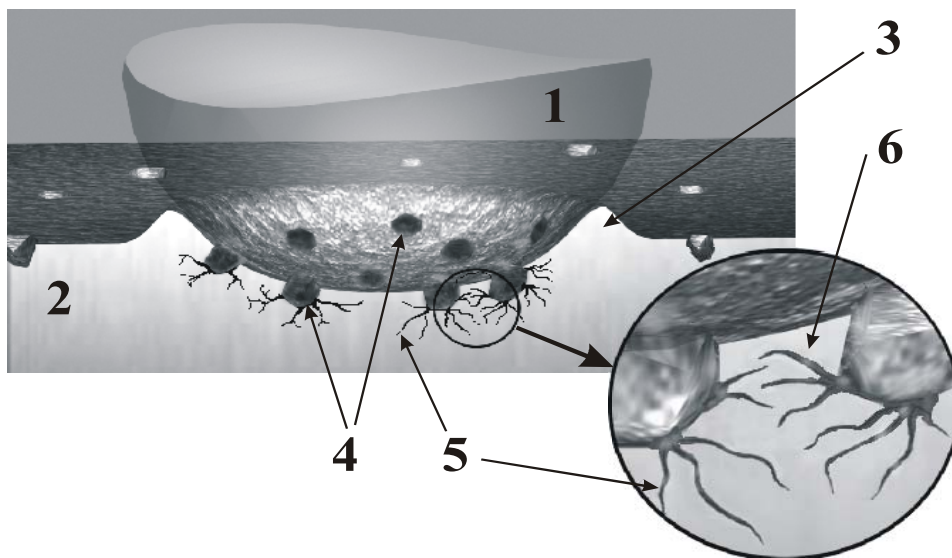a – typical chip, b – chip created as the effect of sublimated gaseous CO_2

Fig. 8. Model of surface erosion using hybrid water-abrasive-ice jet (transparent ice model)

A sudden character of that process is nearly explosive, while the treatment zone is smoggy due to condensed gaseous CO_2. Water plays also important part in this process, since it is a medium penetrating the cracks obtained, hence being responsible for disaggregation of the material. This mechanism generally results in uniform spalling of particles splitted off the workpiece surface. Such an erosion mechanism is especially favourable for decoating of brittle layers from material surface.

8. Conclusions

Theoretical analysis of problems connected with the solid particle motion in the high-pressure hybrid water-abrasive-ice jet and the effect of their action on the workpiece allowed drawing a few conclusion of more general character:

• The erosion efficiency of a hybrid jet achieved by means of the sprinkler with the optimized 4-hole construction nozzle, like all the quantities discussed above, increase along with an increases in the water pressure and the sprinkler tube length, whereas an influence of the jet aeration ratio is rather insignificant.

• The maximum velocity of abrasive grains at the sprinkler outlet is close to the flow velocity of water jet carrying them; however, these grains in the erosion area of the workpiece reach the velocity exceeding 270 m/s, while for dry-ice pellets this velocity is lower by approximately 30%–50%. Owing to this, the kinetic energy of abrasive grains is close to 1×10^{-3} J, while the kinetic energy of dry ice pellets is 300–500 times higher.

• Effectiveness of surface treatment with the hybrid jet depends on the quality of ice particles. For this reason it is recommended to use the ice of the highest quality and also the lowest possible temperature of a high-pressure water jet so that the quality of ice particles accelerated by it declined as low as possible.

• The lowest pressure occurs in internal layers of hybrid jets, whereas much more higher pressure is characteristic of external layers with clearly separated elementary jets whose number is equal to the number of water holes in the sprinkler nozzles.

• The highest number of solid particles flow along the axis of hybrid jet, while the lowest their number flow in external layers of the jet where the highest pressure prevails.

• The flow rate of abrasive grains (#36) during such high-pressure hybrid jet treatment ranges from 90,000 to 150,000 grains per second, while the number of ice pellets is 70 times lower. This is very important for the grain distribution characteristic and erosion mechanism, and also for surface treatment intensity.

• The hybrid jet structure determines the performance and quality of surface treatment. A high pressure in external layers of hybrid jets results in efficient treatment of material surfaces, whereas the internal jet layers cause the treated surface to become smooth.

• This kind of treatment allows us to obtain a considerably high smoothness of surface, which can be obtained by precise grinding. However, the heterogeneity of the hybrid jet structure could be responsible for the wavy effect on the surface.

• The mechanism of the erosion process on the surface treated with a high-pressure hybrid water-abrasive-ice jet is very complicated and specific because a large number of small-size abrasive grains are accompanied with large particles of dry-ice pellets. Therefore the impingements make the part of the dry-ice pellet undergo the sublimation and generate gaseous CO_2 with the volume 800 times larger. Due to the explosive character of that gas generation, the cracks and gaps widen under the influence of the previous collisions of abrasive grains. Consequently, the particles detached from the workpiece take the form of new chips.

References

[1] Borkowski P.: *Physical basis of high-pressure hybrid water-abrasive-ice jet application for surface treatment*, WJTA American Waterjet Conference, Houston, Texas, 2003, Paper 4-A.

[2] Borkowski P.: *Basis of highpressure water-ice jet creation and application for surface treatment*, Surface Treatment VI, Computer Methods and Experimental Measurements for Surface Treatment Effect, Greece, 2003, pp. 85–96.

[3] Borkowski P.: *Fundamentals of surface treatment with high-pressure abrasive-water jet*, 7th Pacific Rim International Conference on Water Jetting Technology, Jeju, Korea, 2003, pp. 321–330.

[4] Borkowski J., Borkowski P. et al.: *Teoretyczne i doświadczalne podstawy intensyfikacji obróbki wysokoenergetyczną hybrydową strugą hydrościerną*, Grant KBN nr 8 T07D 02720, Koszalin, 2001–2003.

[5] Borkowski P.: *Chosen problems of surface machining with high pressure hydrojetting technology*, 7th Meeting of Machinery Construction Committee, PAN, Sci. Publ. Mech. Eng. Dept. Techn. Univ. Koszalin, 2002, No. 30, pp. 139–152.

[6] Borkowski P.: *Obróbka powierzchni wysokociśnieniową strugą wodno-ścierną*, Centrum Technik Proekologicznych, Koszalin, 2002.

[7] Borkowski P., Chomka G.: *Thermodynamics and kinetics aeration of high-pressure water-ice jet*, 7th Meeting of Machinery Construction Committee, PAN, Sci. Publ. Mech. Eng. Dept. Techn. Univ. Koszalin, 2002, No. 30, pp. 127–138.

[8] Borkowski J., Borkowski P., Chomka G.: *Thermodynamical aspects of high-pressure water-ice jet formation*, Archives of Civil and Mechanical Engineering, 2002, Vol. II, No. 1, pp. 35–46.

[9] Borkowski P.: *Physical basis of surface treatment with high-pressure cryogenic multi-phase liquid jet*, Archives of Civil and Mechanical Engineering, 2001, Vol. I, No. 1, pp. 19–37.

[10] Borkowski P.: *The sprinkler optimization used for highpressure hydroabrasive cleaning*, Modern Techniques and Technologies, Sci. Publ. Mech. Eng. Dept. Techn. Univ. Koszalin, 2001, No. 29, pp. 27–38.

[11] Borkowski P.: *Selection of peripheral equipment for small vessels corroded surface cleaning by high-pressure hydroabrasive jet*, Int. Conf. Water Jet Machining WJM, 2001, Cracow, pp. 149–158.

[12] Borkowski J., Borkowski P., Kowalewski A.: *Principles of modeling of the surface machining by highpressure abrasive water jet with genetic algorithm using*, Archives of Civil and Mechanical Engineering, 2001, Vol. I, No. 1, pp. 7–18.

[13] Borkowski P.: *Optymalizacja konstrukcji koncentrycznej dyszy wielootworowej z uwagi na użytkowe właściwości wysokociśnieniowego strumienia hydrościernego*, PhD Thesis, Politechnika Koszalińska, Koszalin, 1997.

[14] Dunsky C.M., Hashish M.: *Observations on cutting with abrasive-cryogenic jets*, 13th Int. Conf. Jetting Technology – Applications and Opportunities, Sardinia, 1996, pp. 679–690.

[15] Galecki G., Vickers G.W.: *The Development of Ice-Blasting for Surface Cleaning*, 6th Int. Symp. Jet Cutting Technology, Surrey, U.K., Paper B-3, 1982, pp. 59–78.

[16] Geskin E.S., Goldenberg B., Shishkin D., Babets K., Petrenko K.: *Ice based decontamination of sensitive surfaces*, 15th Int. Conf. Jetting Technology, Ronneby, 2000, pp. 219–228.

[17] Geskin E.S., Shishkin D., Babets K.: *Application of ice particles for precision cleaning of sensitive surfaces*, 10th American Waterjet Conf, 1999, Vol. 1, Houston, pp. 315–333.

[18] Hashish M., Dunsky C.M.: *The formation of cryogenic and abrasive-cryogenic jets*, 14th Int. Conf. Jetting Technology, Brugge, 1998, pp. 329–343.

[19] Hashish M., Miller P.: *Cutting and washout of chemical weapons with high-pressure ammonia jets*, 15th Int. Conf. Jetting Technology, Ronneby, 2000, pp. 81–92.

[20] Kiyohashi H., Handa K.: *A study of production of ice particles by the heat of vaporization of cryogenic liquefied fuels and their application in ice jets, and so on*, Int. Symp. New Appl. of Water Jet Techn. Ishinomaki, 1999, pp. 51–60.

[21] Liu B.-L., Liu L.-H., Wu L.: *Research on the preparation of the ice jet and its cleaning parameters*, 14th Int. Conf. Jetting Technology, Brugge, 1998, pp. 203–210.

[22] Liu H.T., Fang S., Hibbard C., Maloney J.: *Enhancement of ultrahigh-pressure technology with LN_2 cryogenic jets*, 10th American Waterjet Conf., 1999, Vol. 1, Houston, pp. 297–313.

[23] Matsuyama K., Ueno S., Masutani T., Nishiguchi K.: *Observation of water jet structure with a cantilever method for measurement of total pressure distribution*, 4th Pacific Rim Int. Conf. Water Jet Technology, Shimizu, 1995, pp. 127–138.

[24] Mazurkiewicz M., Olko P., Jordan R.: *Abrasive particle distribution in a high pressure hydroabrasive jet*, Int. Waterjet Symp. Beijing, 1987, pp. 4.1–4.10.

[25] Momber A.W., Kovacevic R.: *Principles of abrasive water jet machining*, Springler-Verlag, London, 1988.

[26] Oczoś K.E., Liubimov V.: *Struktura geometryczna powierzchni. Podstawy klasyfikacji z atlasem charakterystycznych powierzchni kształtowanych*, Wydawnictwo Politechniki Rzeszowskiej, Rzeszów, 2003.

[27] Shishkin D.V., Geskin E.S., Goldenberg B.: *Development of a technology for fabrication of ice abrasives*, 2001, WJTA American Waterjet Conf., Minneapolis, Paper No. 27, 2001.

[28] Spur G., Uhlmann E., Elbing F.: *Dry-ice blasting for cleaning: process, optimization and application*, Wear, 1999, (233–235), pp. 402–411.

[29] Summers D.A.: *Waterjetting Technology*, 1st ed., Chapman & Hall, New York, 1995.

[30] Truchot P., Mellinger P., Duchamp R., Kim T.J., Ocampo R.: *Development of a cryogenic waterjet technique for biomaterial processing applications*, 6th American Water Jet Conf., Houston, 1991, pp. 473–480.

Zasady obróbki powierzchni wysokociśnieniową strugą hybrydową

Obróbka powierzchni wysokociśnieniową strugą hybrydową jest najnowszą technologią o wzrastającej ostatnio popularności. Opiera się ona na wysokociśnieniowej strudze wodno-ściernej domieszkowanej cząstkami suchego lodu CO_2. Przedstawiono teoretyczne podstawy obróbki uwzględniające kinetykę i termodynamikę cząstek stałych wraz z ich rozkładami i ciśnieniami występującymi w strudze hybrydowej. Na podstawie wyników rozważań teoretycznych przeprowadzono badania, które pozwoliły wyjaśnić specyfikę bardzo skomplikowanego mechanizmu erozji powierzchni obrabianej wysokociśnieniową strugą hybrydową.

Direct shear strength of concrete in strip connectors

KAZIMIERZ FURTAK

Cracow University of Technology, Institute of Materials and Building
Structures, 31-155 Kraków, ul. Warszawska 24

The aim of the article is to present the author's proposals of calculating concrete ultimate direct shear strength f_{ctb} and fatigue direct shear strength f_{ctbf}. The effect of scale, important in investigating concrete strength, has been taken into account. The conclusions are valid for concrete class B 30–B 50, hole diameter $ø = 20$–40 mm and strip thickness $t = 12$–20 mm. The doubts about the diameter $ø$ and thickness t are important because of the effect of scale.

On the basis of tests performed by the author it can be stated that the formulae for concrete fatigue compressive strength cannot be applied directly to the description of fatigue strength f_{ctbf} in steel perfobonds. With these formulae the values of fatigue strength f_{ctbf} are underestimated for large numbers of load cycles N or overestimated values of f_{ctbf} for large values of N (which is particularly unfavourable) and underestimated for small N.

Concrete fatigue direct shear strength can be described by formula (9). The proposed way of calculating f_{ctbf} refers basically to the mean value. To define the characteristic (guaranteed) and design values it is proposed to use the same values of design factors as those adopted in determining concrete compressive strength.

1. Introduction

Steel–concrete composite structures have been used for over 100 years now. Recently their quantitative and qualitative development has been observed. This is also true for connectors which guarantee the interaction between the reinforced (most frequently) or pre-stressed (seldom) slab and steel girder. Initially the connectors were inflexible (rigid), next flexible, and recently also in the form of perfobonds [6, 9, 10, 13, 14] (Figure 1).

The fact that strip connectors have not been used for long accounts for their not being included in the composite structures' design standard valid at present [18] nor in norms established on the basis of Eurocodes [2, 3]. In the professional literature, however, there are formulae for carrying capacity design of these connectors. One group of solutions to the problem is based on the assumption that the concrete in perfobond opening works like a rivet in steel structures. That is why we have to know direct shear strength of concrete in order to design the carrying capacity of strip connectors.

Concrete direct shear strength f_{ctb} is not specifically defined. Testing of this strength of concrete is not included in PN-88/B-06250 norm [20] nor in other norms and instructions. This means that the shapes and dimensions of test specimens for determination of this feature are not specified either. It is common knowledge that concrete direct shear strength f_{ctb} is significantly larger than concrete shear strength,

adopted on the level of tensile strength. This was shown in concrete structures design norms PN-56/B-03260 [15] and PN-58/B-03261 [16], no longer valid. Neither did later norms PN-76/B-03264 [17] (replacing PN-56/B-03260 [15]) and PN-91/S-10042 [21] (replacing PN-58/B-03261 [16]) nor Eurocode EC 2 introduce the term of concrete tensile strength. Besides, serious discrepancy in concrete direct compressive strength results when calculation formulae given by different authors are used [11].
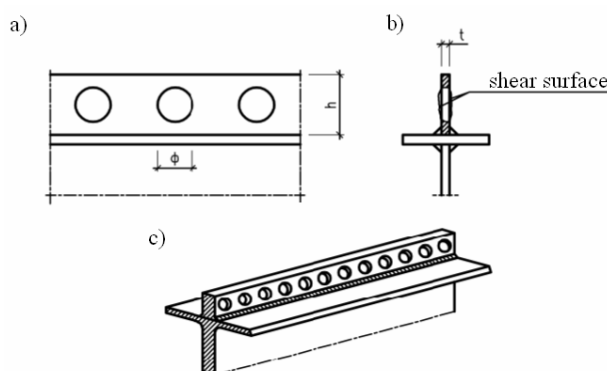

Fig. 1. Strip connector: a – longitudinal cross-section, b – transverse section, c – general view

The structures in which strip connectors are widely used are bridges [6, 8, 9, 10]. They have a considerable contribution to variable useful loads in total load, particularly in designing them for class A or B after PN-85/S-10030 norm [19]. This means that in the elements of these objects the phenomenon of material fatigue may take place, which refers also to connectors.

In the article, the author presents his own suggestions for calculating the direct shear strength of concrete. The effect of scale, important in concrete strength tests, has been included. Since strip connectors can be applied in various steel–concrete composite structures, including those under changeable loads, the quoted suggestions refer to ultimate and fatigue strengths. The author's solutions have been based on the results of his experimental tests.

2. Experimental tests

2.1. Test specimens and methodology

The tests were run on specimens whose dimensions have been shown in Figure 2. The specimens were two cubes connected monolithically by a cylinder of diameter and width matching the hole in the perfobonds used in composite structures. The whole test specimen was concreted simultaneously.

The lengths of cubes' sides were $a = 10$ cm and $a = 15$ cm. They corresponded to the cubes used for tests on concrete strength and to that end they were used at the sec-

ond stage of tests. After the direct shear test had been completed one cube was always used for determination of concrete compressive strength, the other one – tensile strength (by splitting).

Due to this test methodology concrete direct shear, compressive and tensile strengths were determined for each element (and so for the same concrete). This made it easier to find the dependencies between the tested strength characteristics of the same concrete.
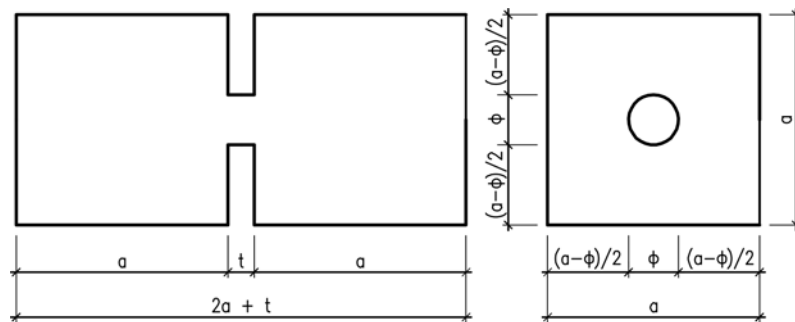

Fig. 2. Shape and dimensions of the specimen tested

The shape and dimensions of the cylinder (reduction of the area between the cubes) were: $\phi = 20$, 30 and 40 mm. Dimension t (clear distance equal to width of reduction between cubes) was: $t = 13$, 17 and 21 mm. This corresponded to the perfobond thickness $t = 12$, 16 and 20 mm, respectively. The difference of 1 mm was used to eliminate (or at least minimise) the friction of the specimen transferring the load during test.

The loads on the cylinder connecting the cubes were transferred by steel elements of the thickness equal to the width t, and the diameter of the loading surface was the same as that of cylinder (reduction) ϕ. This reflected well the conditions of concrete direct shear loading in the holes of the perfobonds.

2.2. Results of testing ultimate strength

The results of testing on direct shear strength of concrete have been shown in Figures 3–8. The vertical lines in bold represent the range of the results, while the asterisks refer to mean values. The mean value was calculated from 12–24 measurements, which made it impossible to show them individually in the figures.

In the figures, the shear diameter ϕ and concrete mean strength (compressive $\overline{f}_c$, tensile $\overline{f}_{ct}$ and geometric mean $\overline{f}_{tg} = \sqrt{\overline{f}_c \, \overline{f}_{ct}}$) have been adopted as the independent variables. No clear effect of the strip thickness was noticed and this is why this parameter has been omitted in test results.
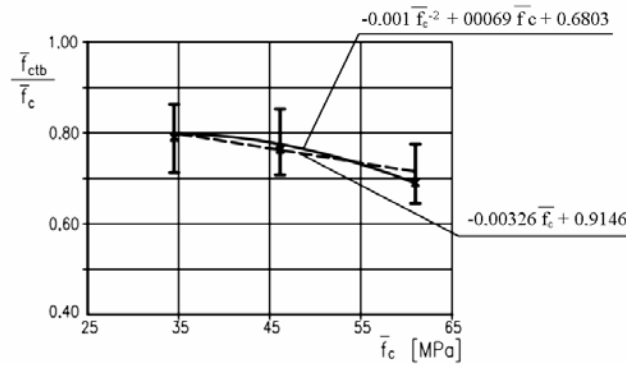
$$-0.001\,\overline{f_c}^{-2} + 00069\,\overline{f_c} + 0.6803$$

$$-0.00326\,\overline{f_c} + 0.9146$$

Fig. 3. $\overline{f}_{ctb}/\overline{f}_c$ versus $\overline{f}_c$

Figures 3 and 4 illustrate the effect of concrete mean strength $\overline{f}_c$ and shear diameter ϕ on the ratio of concrete mean direct shear strength $\overline{f}_{ctb}$ to concrete mean compressive strength $\overline{f}_c$, while Figures 5 and 6 show the effect of the same parameters ($\overline{f}_c$, ϕ) on the ratio of the strength $\overline{f}_{ctb}$ to concrete mean tensile strength $\overline{f}_{ct}$. Figures 7 and 8 present the effect of $\overline{f}_c$ and ϕ on the ratio of $\overline{f}_{ctb}$ to geometric mean $\overline{f}_{tg}$.

$$-0.004\Phi + 0.8670$$

$$0.0002\Phi^2 - 0.016\Phi + 1.04$$
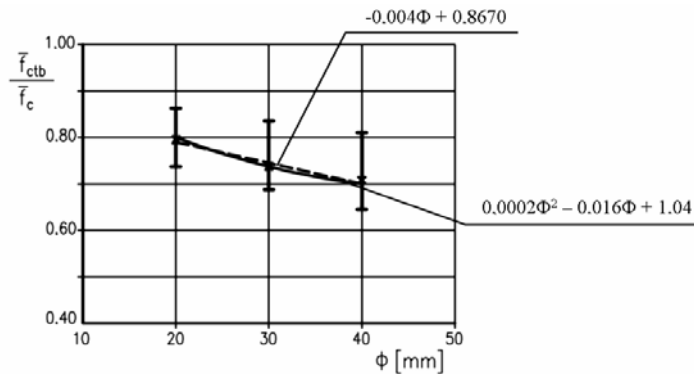
Fig. 4. $\overline{f}_{ctb}/\overline{f}_c$ versus ϕ

In all cases, the concrete relative (referred to concrete compressive and tensile strengths) direct shear strength $\overline{f}_{ctb}$ reveals a strong tendency to decrease with an increase in concrete strength ($\overline{f}_c$, $\overline{f}_{ct}$, $\overline{f}_{tg}$) and shear diameter ϕ. The approximately

linear change of $\overline{f}_{ctb}$ dependent on ϕ is worth noticing (in the range of ϕ equal to 20–40 mm, which actually covers a significant part of the range of practical applications).
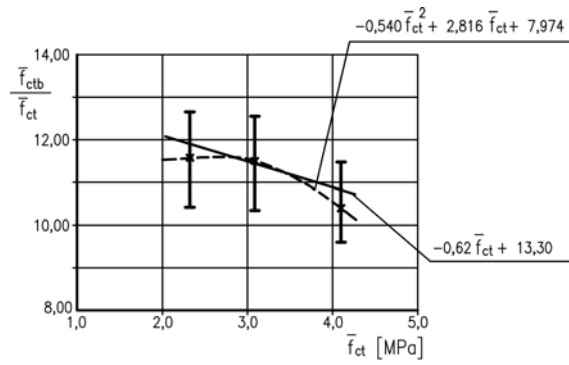

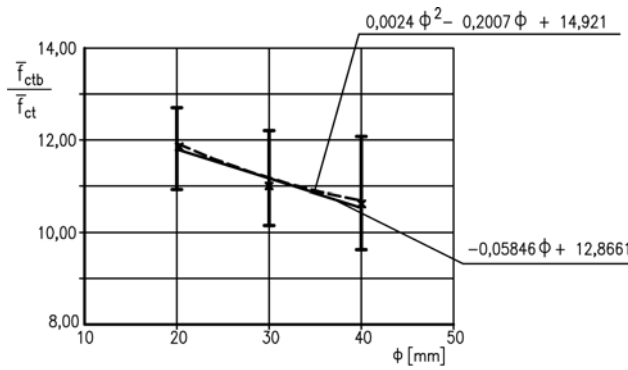Fig. 5. $\overline{f}_{ctb}\big/\overline{f}_{ct}$ versus $\overline{f}_{ct}$

Fig. 6. $\overline{f}_{ctb}\big/\overline{f}_{ct}$ versus ϕ
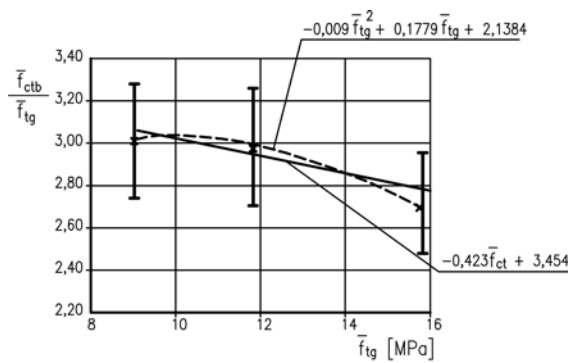
Fig. 7. $\overline{f}_{ctb}\big/\overline{f}_{tg}$ versus $\overline{f}_{tg}$
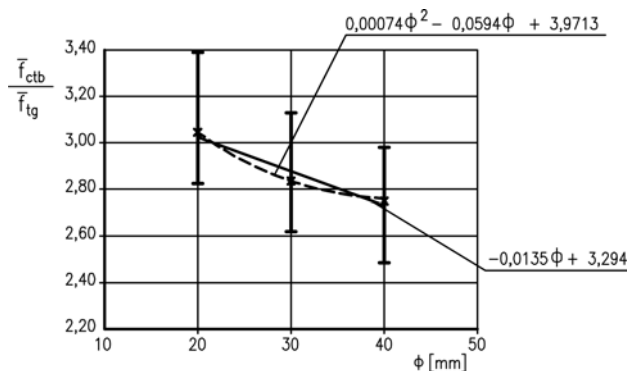
Fig. 8. $\overline{f}_{ctb}/\overline{f}_{tg}$ versus ϕ

The test results presented in Figures 3–8 can be described analytically (adopting linear regression and then the second-order polynomial) assuming the mean values (marked with crosses in the figures) as proper. The dependencies are represented by particular graphs shown in figures. In the formulae, the strength is expressed in [MPa], and the diameter ϕ in [mm].

2.3. Results of testing fatigue strength

The results of testing concrete fatigue resistance to direct shear f_{ctbf} have been shown in Figures 9–13. Figures 9–11 illustrate the dependence of κ on log N at constant values of stress ratio $R = P_{min}/P_{max} + \tau_{min}/\tau_{max}$, while Figures 12 and 13 show the dependence of log N on R at constant values of κ. κ denotes the ratio of the concrete fatigue resistance to direct shear $\overline{f}_{ctbf}$ to concrete ultimate resistance to direct shear $\overline{f}_{ctb}$ ($\kappa = \overline{f}_{ctbf}/\overline{f}_{ctb}$).
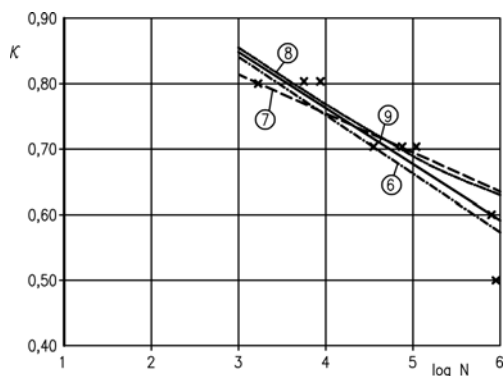

Fig. 9. Results of testing concrete fatigue direct shear strength for $R = 0.10$
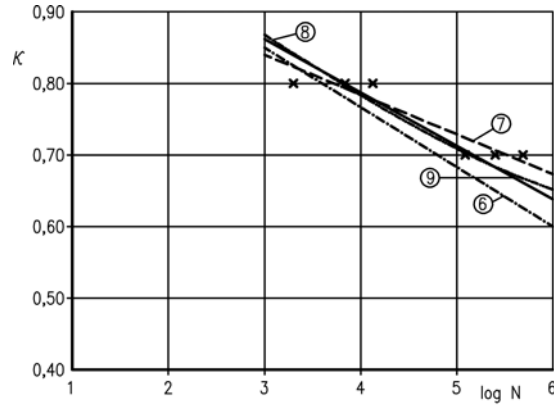
Fig. 10. Results of testing concrete fatigue direct shear strength for *R* = 0.20
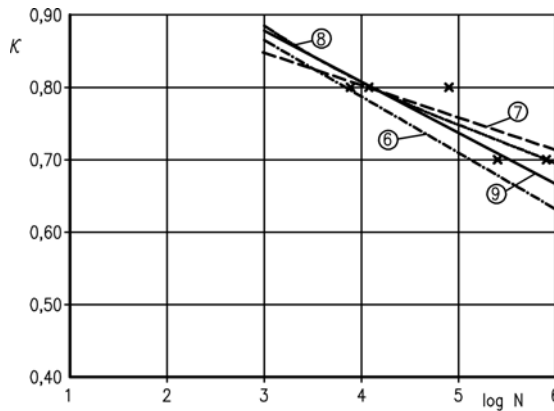

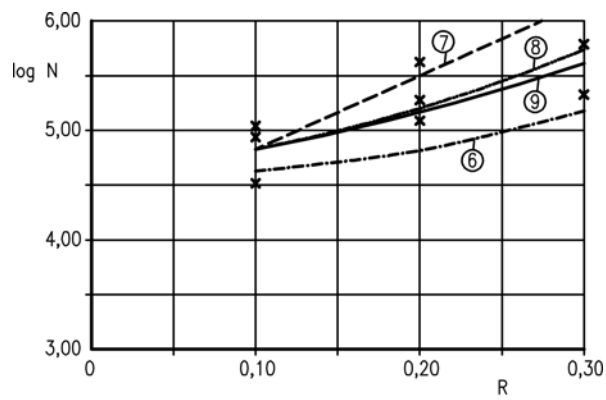Fig. 11. Results of testing concrete fatigue direct shear strength for *R* = 0.30

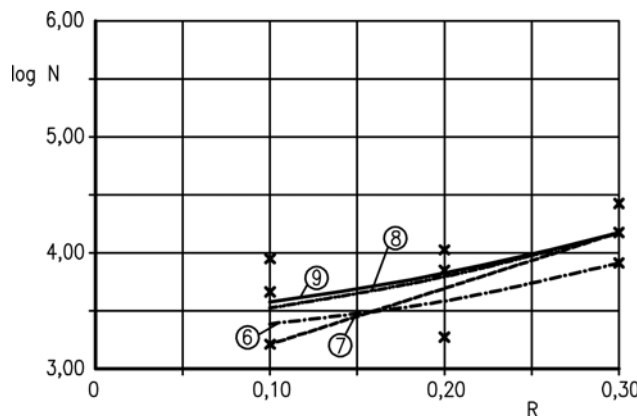Fig. 12. Results of testing concrete fatigue direct shear strength for *κ* = 0.70

Fig. 13. Results of testing concrete fatigue direct shear strength for $\kappa = 0.80$

3. Analytical description of concrete fatigue direct shear strength

Similarly as in [7], in order to describe concrete fatigue direct shear strength, three different dependencies have been adopted at random, which are often used in the description of concrete compressive and tensile strengths [1, 4, 5, 11, 12, 22]. The first one, proposed by Korczyński and Bieczeniewa [11], can be written in a general form:

$$\kappa = 1.10\left[1 - \frac{\log N}{6.3}\left(1 - \frac{1}{a - bR}\right)\right], \tag{1}$$

where:

κ – the ratio of mean fatigue strength $\overline{f}_{ctbf}$ to mean ultimate direct shear strength $\overline{f}_{ctb}$:

$$\kappa = \overline{f}_{cud} / \overline{f}_{cud}; \tag{2}$$

N – limit number of load cycles followed by fatigue wear,
R – stress ratio equal to the ratio of minimum stress τ_{min} – maximum stress τ_{max} in load cycle:

$$R = \tau_{min} / \tau_{max}, \tag{3}$$

a, b – coefficients determined during experiments.
The next proposal for describing fatigue strength adopted, for instance, in [1, 22] has a general form:

$$\kappa = c - d\,(1 - e\,R)\,\log N, \tag{4}$$

where c, d and e are the coefficients determined experimentally, while R and N stand for, as before, the stress ratio and limit number of load cycles.

The third proposition, given in [4, 5] and [12], refers to the description of concrete fatigue compressive and tensile strengths. It assumes a general form:

$$\kappa = 1.16\,N^A\,(1 + B\,R\,\log N), \tag{5}$$

where A and B are the coefficients whose values depend on initiating and critical stresses of concrete.

Based on the analysis of the results of the author's tests and those done by others the authors of the quoted formulae proposed the following mean values of the parameters in formulae (1) and (4): $a = 2.14$, $b = 1.14$, $c = 1.00$, $d = 0.0685$, $e = 1.00$. For average conditions $\sigma_i = 0.45\,f_c$, $\sigma_{cr} = 0.80\,f_c$ (σ_i – initiating stress, σ_{cr} – critical stress, f_c – concrete compressive strength) we obtain [4, 5]: $A = 0.049$, $B = 0.092$.

Having introduced the given values of the coefficients in formulae (1), (4) and (5) we finally obtain:

$$\kappa = 1.10\left[1 - \frac{\log N}{6.3}\left(1 - \frac{1}{2.14 - 1.14R}\right)\right], \tag{6}$$

$$\kappa = 1.00 - 0.0685\,(1 - R)\,\log N, \tag{7}$$

$$\kappa = 1.16\,N^{-0.049}\,(1 + 0.092\,R\,\log N). \tag{8}$$

It should be emphasized at the same time that the values of the coefficients A and B are determined irrespective of the results of concrete fatigue tests. That is why the results of experiments verify theoretical formula (8), while in the other two cases they were used only for determining the values of the coefficients.

The comparison of the results of experimental tests with the values of concrete fatigue direct shear strength described by formulae (6)–(8) has been shown in Figures 9–13. The numbers of lines in the figures correspond to the numbers of the formulae.

On the basis of the analysis of the test results we can propose calculating concrete fatigue direct shear strength as follows:

$$\kappa = 1.10 - 0.09\,(1 - 0.7\,R)\,\log N. \tag{9}$$

The proposition has also been included in Figures 9–13.

From the results of tests and results obtained by using the quoted formulae it can be stated that concrete fatigue direct shear strength $\overline{f}_{ctbf}$ is best described by formula (8)

or (9). Formula (6) gives underestimated values of $\overline{f}_{ctbf}$ for large numbers of load cycles N, while following formula (7) we arrive at overestimated values of $\overline{f}_{ctbf}$ for large N and underestimated ones for small numbers of cycles N.

4. Final conclusions and remarks

The problem dealt with in the article is concrete ultimate direct shear strength $\overline{f}_{ctb}$ and fatigue direct shear strength $\overline{f}_{ctbf}$ which can be adopted in the design of carrying capacity of strip connectors in steel–concrete composite structures. The conclusions are valid for concrete class B 30–B 50, hole diameter ϕ ranging from 20 to 40 mm and strip thickness t varying between 12 and 20 mm. The doubts as to the diameter ϕ and thickness t are important because of the significant effect of scale in concrete strength investigation.

On the basis of experimental tests it can be stated that the formulae for concrete fatigue compressive strength cannot be applied directly to the description of fatigue strength f_{ctbf} in steel perfobonds. With these formulae the values of fatigue strength f_{ctbf} are underestimated for large numbers of load cycles N or overestimated for large values of N (which is particularly unfavourable) and underestimated for small N.

The effect of scale is a separate problem. The numerical values of ultimate f_{ctb} and fatigue f_{ctbf} direct shear strengths of concrete in steel perfobonds are much higher than those quoted by valid norms and those valid in the past [6].

Concrete ultimate shear strength can be calculated from the formulae given in Figures 3 and 4. For the sake of linear dependencies they are recommended.

Concrete fatigue direct shear strength can be described by formula (9). However, it should be remembered that the values of the coefficients for this formula were determined on the basis of tests with a relatively small number of test specimens (the tests took several months anyway, which is due to the time-consuming fatigue tests) which made it impossible to apply a statistic analysis.

The proposed way of calculating f_{ctbf} refers basically to the mean value. For design purposes it is not the mean value of strength that is adopted but the design strength. In view of insufficient number of results of tests (performed by the author or other researchers) on the basis of which the statistical correlation between the mean, characteristic (guaranteed) and design values could be found, it is proposed to use the dependencies adopted in determining concrete compressive strength. The favourable verification of such approach was carried out for concrete bearing strength [8].

Adopting the given assumption we obtain $f = f_k / \gamma_c = 0.7786\, \overline{f} / \gamma_c$. In this general form f denotes design strength, f_k – characteristic strength, and $\overline{f}$ mean strength, while γ_c is a partial safety factor relative to concrete. The general formula refers to both ultimate and fatigue strengths.

References

[1] Aas-Jakobsen K.: *Fatigue of Concrete Beams and Columns*, Bulletin No 70-1, NTH Institutt for Betonkonstruksjoner, Trondheim, Sept. 1970.

[2] Eurocode No. 4: *Design of Composite Steel and Concrete Structures*, Part 1–1: *General Rules and Rules for Buildings*.

[3] Eurocode No. 4: *Design of Composite Steel and Concrete Structures*, Part 2: *Bridges*.

[4] Furtak K.: *Concrete strength under cyclic loads*, Civil Engineering Archives, Vol. XXX, No. 4, 1984.

[5] Furtak K.: *Ein Verfahren zur Berechnung der Betonfestigkeit unter schwellenden Belastungen*, Cement and Concrete Research, Vol. 14, 1984, pp. 855–865.

[6] Furtak K.: *Composite bridges*, PWN, Warszawa–Kraków, 1999.

[7] Furtak K.: *Concrete fatigue direct shear strength in strip connectors of composite elements*, Cement, Lime, Concrete, 3/2004.

[8] Furtak K., Sobczyk M.: *Concret ultimate resistance to pressure in strip connectors of composite structures*, Engineering and Building, 3–4/2002.

[9] Furtak K., Sobczyk M., Wąchalski K.: *A new generation of connectors in composite bridges*, Engineering and Building, 5/1998.

[10] Głomb J., Furtak K., Skoplak Z., Sobczyk M.: *The bridge over the Regalica river in Szczecin – some design aspects*, XLIX Conference KILiW PAN and KN PZITB, Krynica 2003.

[11] Korczinskij I.L., Bieczeniewa G.W.: *Strength of building materials under dynamic loads*, (in Russian), Literatura po stroitielstwu, Moscow, 1966.

[12] Lachiewicz-Złotowska A.: *The effect of dead and changing loads on concrete tensile strength*, PhD dissertation, Kraków, 1999.

[13] Leonhardt F., Andrä W., Andrä H.-P., Harre W.: *Neues vorteilhaftes Verbundmittel für Stahlverbund-Tragwerke mit hocher Dauerfestigkeit*, Beton- und Stahlbeton, 12/1987.

[14] Leonhardt F., Andrä W., Andrä H.-P., Harre W., Saul R.: *Zur Bemessung durchlaufender Verbundträger bei dynamischer Belastung*, Der Bauingenieur 62/1987.

[15] PN-56/B-03260: *Concrete and reinforced concrete bridges*, *Structural analysis and design*.

[16] PN-58/B-03261: *Reinforced concrete structures*, *Structural analysis and design*.

[17] PN-76/B-03264: *Concrete, reinforced concrete and prestressed structures*, *Structural analysis and design*.

[18] PN-82/B-03300: *Composite steel and concrete structures*, *Structural analysis and design*, *Composite squat beams*.

[19] PN-85/S-10030: *Bridges*, *Loads*.

[20] PN-88/B-06250: *Ordinary concrete*.

[21] PN-91/S-10042: *Bridges*, *Concrete, reinforced concrete and prestressed structures*.

[22] Tepfers R., Kutti T.: *Fatigue Strength of Plain, Ordinary and Lightweight Concrete*, ACI Journal, Vol. 76, No. 5, May 1979.

Wytrzymałość betonu na ścinanie bezpośrednie w łącznikach listwowych

W artykule zaproponowano własny sposób obliczania doraźnej f_{ctb} i zmęczeniowej f_{ctbf} wytrzymałości betonu na ścinanie bezpośrednie w łącznikach listwowych. Uwzględniono przy

tym efekt skali, ważny w badaniach wytrzymałościowych betonu. Podane wnioski są ważne w przypadku betonu klasy B 30–B 50, średnicy otworów ϕ od 20 do 40 mm oraz grubości listew 12–20 mm. Zastrzeżenia dotyczące średnicy ϕ oraz grubości t są ważne ze względu na efekt skali.

Na podstawie wyników własnych badań doświadczalnych można stwierdzić, że do opisu wytrzymałości zmęczeniowej f_{ctbf} w perforowanych listwach stalowych nie można wprost zastosować wzorów pozwalających obliczyć wytrzymałość zmęczeniową betonu na ściskanie lub rozciąganie. Korzystając z tych wzorów, uzyskuje się zaniżone wartości wytrzymałości zmęczeniowej f_{ctbf} dla dużych liczb cykli obciążenia N lub zawyżone wartości f_{ctbf} dla dużych wartości N (co jest szczególnie niekorzystne) i zaniżone wartości f_{ctbf} dla małych N.

Wytrzymałość zmęczeniową betonu na ścinanie bezpośrednie można opisywać wzorem (9). Podany sposób obliczania f_{ctbf} dotyczy w zasadzie wartości średniej. Aby określić wytrzymałość charakterystyczną (równą gwarantowanej) i obliczeniową, zaproponowano przyjmowanie takich samych wartości współczynników przeliczeniowych, jakie stosuje się, określając wytrzymałość betonu na ściskanie.

Planning of assembly sequences based on hybrid evolutionary algorithms

T. JANKOWSKI, B. REIFUR

Wrocław University of Technology, Wybrzeże Wyspiańskiego 25, 50-370 Wrocław

The paper deals with the planning of assembly sequences. An evolutionary algorithm for the planning of assembly sequence has been developed. Its use is illustrated by an example and the results obtained are discussed. The application of the algorithm to production process control can bring substantial benefits, which involves quick preparation of the system for performing manufacturing tasks and for the current control of the flow of the product in the system. As the assembly process cost and lead time are reduced, the efficiency of the product manufacturing increases.

Keywords: *sequences, genetic algorithm, assembly*

1. Introduction

The final stage of the technological process is assembly during which previously manufactured machine components are put together into assembly units, or lower-order assembly units are put together into higher-order assembly units and finally, into a finished product (machine). Assembly is carried out in accordance with a series of planned logical actions so that the assembly units and a complete product meet the specifications imposed by a designer.

The correct design of assembly process and its proper realization determine the performance of the intended functions by the product (a machine or a mechanism) and its service life. Since assembly is critically important and time-consuming, it should be properly prepared and realized.

One of the primary objectives of assembly design is to determine the most proper sequence of putting the components (units) together. The aim of planning of assembly sequences is to determine different orders in which the assembly operations can be performed and to evaluate the orders of determining the optimum sequence. The criterion according to which the assembly plans are evaluated is the total cost of the assembly process. Because of geometric, topological and technological constraints that are imposed it is difficult to develop an optimum assembly plan. The number of possible assembly plans depend exponentially on the number of parts the product is made of. A proper assembly plan reduces the number of base part reorientations and retooling and by combining manipulations into multimanipulation operations and the simultaneous attachment of several parts eliminates some operations whereby the number of needed assembly tools and hence the production costs are reduced.

It is very important, but difficult, to find an optimum assembly plan as part of tactical planning and operational control. Tactical planning and operational control are involved in the quick preparation of a production system for performing production tasks and in the current control of the flow of the product in the system. Therefore methods of a quick generation of assembly plans are required.

In the construction of a computer-aided technological process design system, two types of tasks can be distinguished [2, 3]:

• the development of a universal method allowing one to model and algorithmize whole processes and their structural components in a simple way,

• the development of a formalized technological language allowing one to write all the information in a form which can be fed into a computer.

To reduce the time required for designing such a complex process as assembly and to achieve positive economic results, computer techniques and analyses aided by expert systems, artificial neural networks and relational databases are more and more often employed. In the design and visualization of assembly processes, expert systems should collaborate with computer-aided design (CAD) systems, production planning systems (PPS) and computer-aided assembly process planning (CAAPP) systems.

2. Methods of generating assembly sequences

Among the current methods of generating assembly sequences one can distinguish four basic groups [2]:

1. Methods characterized by a three-stage procedure of building sequences. First, sequential relations between the finished product's components are generated on the basis of geometrical and topological information, taking all the geometrical and mechanical constraints into account. This can be done by analyzing the assembly operations or the disassembly of the finished product. The sequential relations are used to generate assembly sequences. Finally, the best sequence is selected according to the optimization criterion adopted.

2. Methods consisting in dividing the assembled unit into subunits and generating proper subsequences by applying simple rules.

3. Expert systems built for the assembly of specific, unique units.

4. Methods generating different product assembly sequence variants by modifying predefined sequences.

Considering the accuracy of the results obtained and the time in which they are obtained, i.e. the practical application of the different methods of generating assembly sequences, the methods can be divided into:

• algorithmic methods – yielding optimum (according to the criterion adopted) assembly sequences,

• heuristic methods – yielding good solutions in a reasonable time.

Solving the Assembly Sequence Planning Problem (ASPP) implies generating solutions, feasible assembly sequences. An assembly sequence is feasible if it satisfies

absolute constraints. Optimizing the ASPP involves selecting an optimum or near optimum feasible assembly sequence according to an objective function based on optimization criteria (Figure 1). Hybrid evolutionary algorithms were chosen for the optimization of ASPP because of their ability to handle large-scale problems and their flexibility in defining a fitness function.
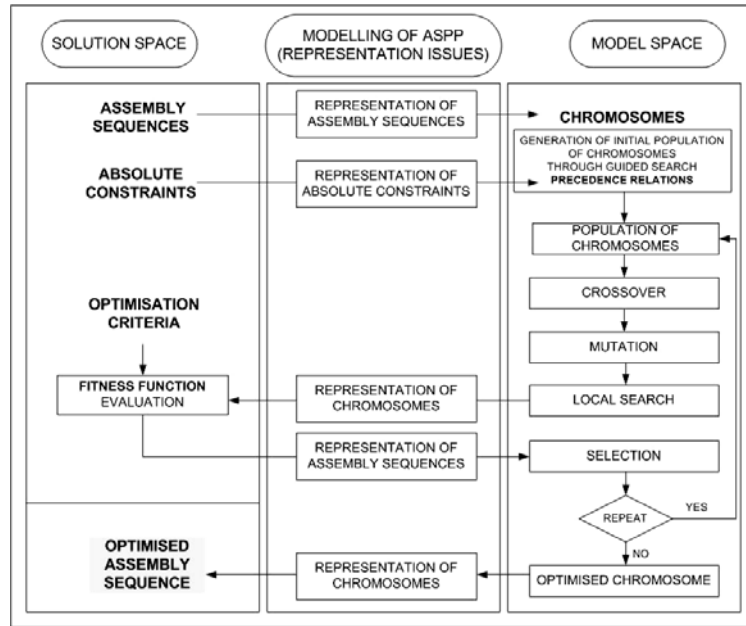

Fig. 1. The approach for Assembly Sequence Planning Problem

As regards the former methods, a set of realizable sequences is obtained mainly through an analysis of all the cuts in the graph of the assembled product's structure. In order to find an optimum sequence, one must use many criteria and estimations, often differently interpreted by different users. The optimum sequence is determined before the start up of the assembly process and the computation time is usually long. In the case of assemblies made up of a dozen or so parts, finding the optimum sequence is, combinatorially, a very difficult task. The number of assembly plans depend exponentially on the number of parts in the product. Hence a failure of the assembly stand or accidental damage to the assembled part forces the control system (e.g. a flexible assembly line) to stop the production process and determine a new assembly plan. Since such delays are unacceptable, the search for the best solution tends to be abandoned for heuristic procedures which quickly yield good (close to optimum) solutions.

Algorithmic methods include: the Homem de Mello method based on the decomposition of the assembled unit, the point Yager method, the method based on temporal logic laws and the method of limiting a combinatorial explosion [1]. Heuristic meth-

ods include: expert methods, methods based on unit breakdown drawing, methods based on fuzzy logic, the hierarchical Gu procedure, the three-stage heuristic of finding sequences and the evolutionary algorithm presented below.

3. Evolutionary algorithm

The evolutionary algorithm is applied here to the automated planning of assembly sequences. Evolutionary algorithms are computer systems for solving systems operating on similar principles as the ones observed in the evolution of living organisms. In order to design an evolutionary algorithm, the following components must be defined [4, 5]:

- a genetic representation of potential solutions,
- a method of generating a population of initial solutions,
- a fitting function for the evaluation of potential solutions,
- genetic operators,
- conditions for terminating the generation of successive populations,
- other permanent parameters (including the population size and the probability of applying genetic operators).

Representation – one of the key decisions made when applying evolutionary algorithms concerns the method of coding. The latter is specified by defining the representation between a point in the solution space (an assembly sequence) and a point in the representation space (chromosome). Binary representation is the basic method in genetic algorithms, evolutionary strategies are based on real numbers representation and in genetic programming mainly trees defining program structures are used.

The described here way of using the evolutionary algorithm for generating assembly sequences is based on integer representation (Figure 2). A chromosome (an assembly sequence) consists of natural numbers representing the particular parts of an assembled unit or the finished product.
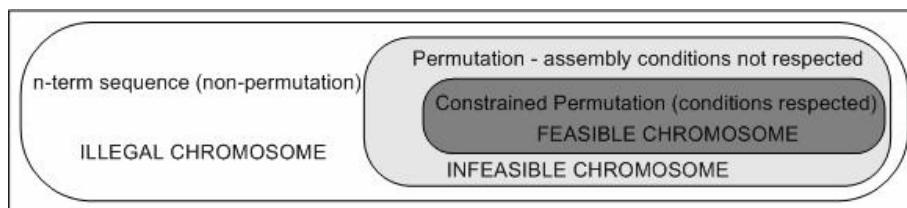

Fig. 2. Assembly sequence representation [1]

The aim of initiating a population is to generate a population with a specified size, from which the algorithm will start the process of evolution. Regardless of the way in which this is realized, allowable chromosomes, i.e. having a specific representation in the solution space, must be generated. The effectiveness of the process of evolution

can be significantly improved if a good initial population with a proper size is used. One should note that when well adapted chromosomes are generated by other methods, there is a danger that the evolution will be directed towards a local optimum. In the solution presented here, the initial population is generated randomly. The size of the population is one of the algorithm's parameters.

Crossever – the task of the crossover operator (Figure 3) is to recombine fragments of the parents' chromosomes and to generate new (offspring) chromosomes in this way. The algorithm considered incorporates three procedures for realizing the crossover operator: one-point crossover, two-point crossover and order-based crossover (transmitting the relative order of genes in a parent's chromosome to the descendant).
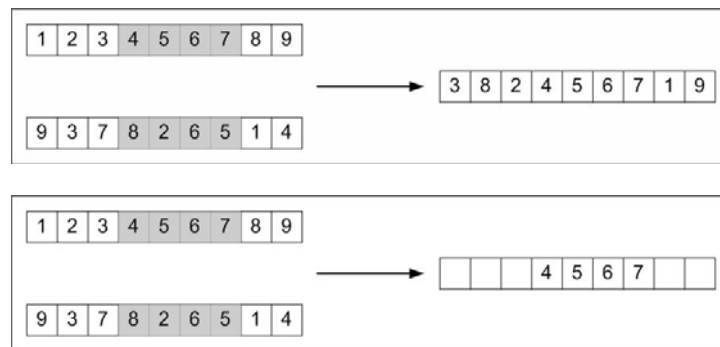
Fig. 3. Genetic operator – order crossover (OX)

Mutation – the mutation operator is responsible for the random introduction of changes into the chromosome. The algorithm incorporates two methods of realizing this operator (Figure 4): 1 – a mutation based on the transposition of the positions of two genes (an order-based mutation), which consists in the random selection of two elements in the chromosome and transposing their positions and 2 – a mutation based on the shift of a selected gene to another position in the chromosome (a position-based mutation), in which two genes are selected randomly and the second gene is placed before the first one.
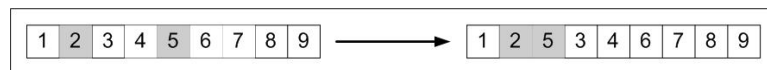

Fig. 4. Genetic operator – swap mutation

Selection – selection (carried out during the stages of reproduction and succession) results in the orientation of the algorithm towards solutions being an improvement over the hitherto obtained solutions. The aim of reproduction is to select parents for genetic operations: first a temporary population is created which is then subjected to

genetic operations resulting in a filial population. The algorithm incorporates three ways of reproduction: proportional (roulette), tournament and rank reproduction. Succession consists in the generation of a new base population, using individuals from the filial population and the old base population. In the presented application, two methods of succession are used: the total replacement method and the elite method (Figure 5).
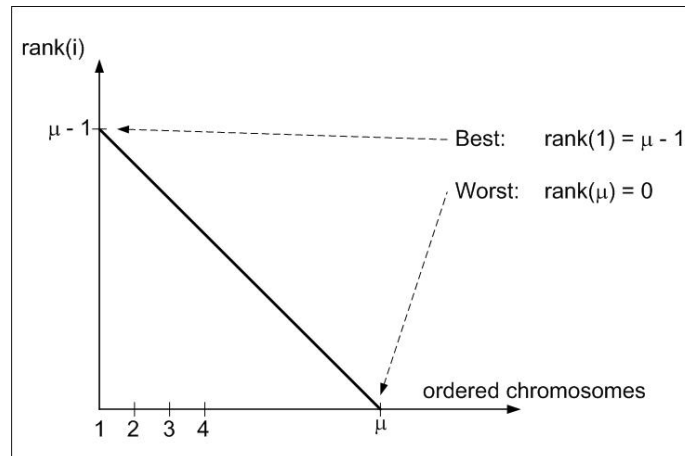

Fig. 5. Genetic operator – rank-based selection

The adaptation of chromosomes to the environment, i.e. how they meet the constraints stemming from the geometrical, topological and technological descriptions of the assembled unit and the technological process of assembly, is evaluated.

• First how the chromosome meets the geometrical constraints written in the antecedence matrix (created on the basis of the graph of relations between the parts) is evaluated.

• Then the minimization of reorientation of the base part, i.e. the assembly of the possibly largest number of parts under the current setting of the base part, is evaluated.

• Finally, the minimization of replacements of gripping devices, i.e. the assembly of the possibly largest number of parts by means of the current gripping device, is evaluated. Data on the selection of gripping devices for the particular parts are contained in a gripping device matrix.

Through such optimisation of the sequence one can minimize the total time needed for the assembly of a unit or the product, which has a direct bearing on the total cost of assembly.

4. Application of the algorithm

As an example, the evolutionary algorithm is applied here to generate an assembly sequence for the valve shown in Figure 6.
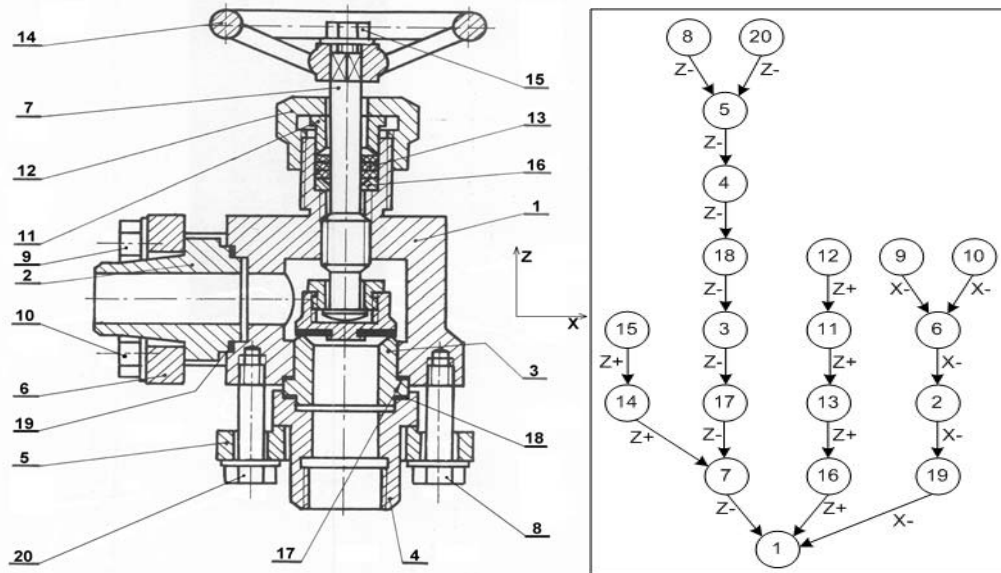
Fig. 6. Diagram of valve and graph of relations for particular valve parts and assembly directions

The valve is made up of 20 elements most of which are single parts, except for element 7 which is a subassembly consisting of four parts. The diagram of the valve was the basis for a graph of relations between the parts in the valve in the particular assembly directions ($X-$, $Z+$, $Z-$) which in turn was used to create matrices of constraints for the particular components of the valve.
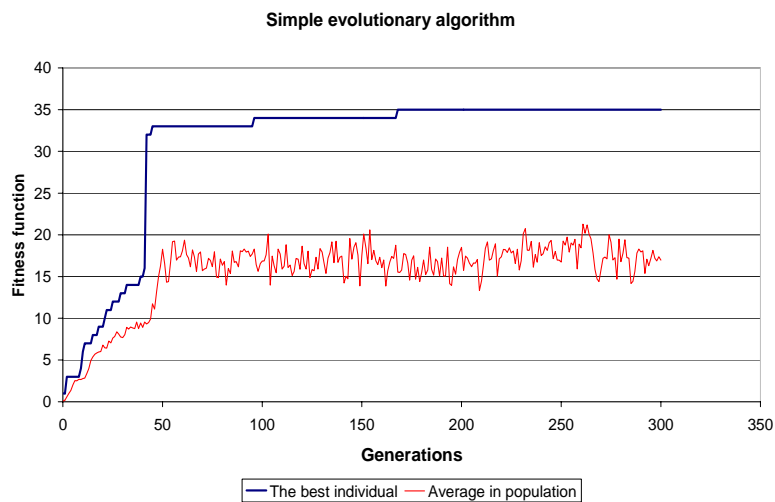

Fig. 7. Evolution of fitness function for simple evolutionary algorithm

On the basis of the matrices, the antecedence, the directions and the gripping devices the algorithm computes the adaptation function values for the particular chromosomes.

The adaptation function values as a function of successive algorithm iterations are shown in Figure 7. The results were obtained for the following algorithm parameters: population size – 40 individuals, crossover probability – 0.6 and mutation probability – 0.2, using the following operators: one-point crossover, position-based mutation, tournament reproduction and elite succession.

Hybrid evolutionary algorithm
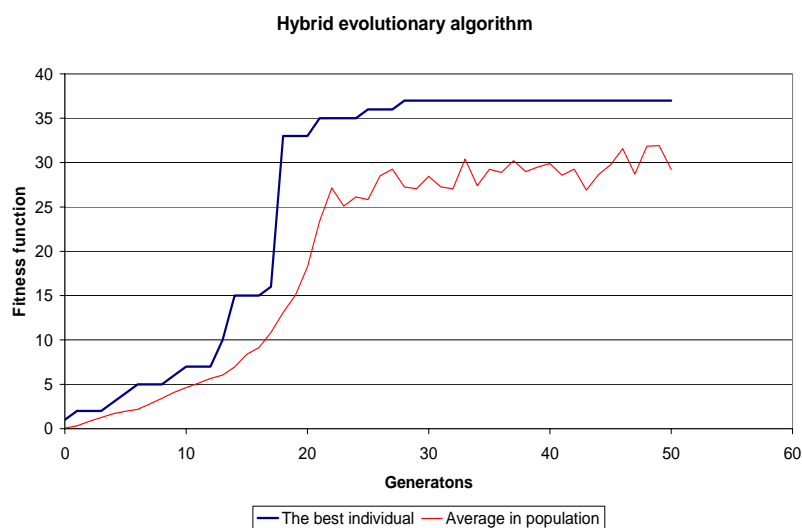
Fig. 8. Evolution of fitness function for hybrid evolutionary algorithm

5. Conclusion

The generation of variants of assembly sequences and the selection of an optimum plan of operations have been presented. Operational control involves the preparation of the system for the performance of production tasks in a short time and for the current control of the flow of the product in the system. The development of an optimum assembly sequence has a direct bearing on the costs of technological assembly. The application of fast algorithms, to which the evolutionary algorithm presented here belongs, to the operational control of the assembly process can bring substantial benefits.

References

[1] Marian Romeo M., Luong Lee H.S. Abhary Kazem: *Assembly sequence planning and optimization using genetic algorithms*, Part I. *Automatic generation of feasible assembly sequences*.

[2] Łebkowski P.: *Metody komputerowego wspomagania montażu mechanicznego w elastycznych systemach produkcyjnych*, Wydawnictwa AGH, Cracow, 2000.

[3] Van Holland W. Bronsvoort W.F.: *Assembly features in modeling and planning*, Robotics and Computer Integrated Manufacturing, 2000, (16), 277–294.

[4] Pawlak M.: *Algorytmy ewolucyjne jako narzędzie harmonogramowania produkcji*, Wydawnictwo Naukowe PWN, Warsaw, 1999.

[5] Arabas J.: *Wykłady z algorytmów ewolucyjnych*, WNT, Warsaw, 2001.

Planowanie sekwencji montażowych z wykorzystaniem hybrydowych algorytmów ewolucyjnych

Jednym z głównych zadań projektowania procesu technologicznego montażu jest ustalenie najwłaściwszej kolejności sekwencji montażowych, wyznaczenie różnych wariantów kolejności operacji montażowych oraz ocena tych wariantów pozwalająca ustalić sekwencję optymalną. Kryterium oceny powstałych planów montażu jest ostatecznie całkowity koszt procesu montażu. Właściwy wybór planu montażowego, eliminując pewne operacje, znacznie ogranicza liczbę reorientacji części bazowej, liczbę zmian narzędzi, łączenie zabiegów w operacje wielozabiegowe i jednoczesne przyłączanie kilku części. Zmniejsza się przez to ilość potrzebnych urządzeń montażowych i ostatecznie redukuje koszty produkcji. W artykule przedstawiono problem wariantowości sekwencji montażu oraz wyboru optymalnego planu operacji. Zastosowanie przedstawionego algorytmu w sterowaniu operacyjnym procesem produkcyjnym umożliwia osiągnięcie korzyści związanych z przygotowaniem systemu do wykonywania zadań produkcyjnych w krótkim czasie i do bieżącego sterownia przepływem wyrobu w systemie.

Assessment of surface topography of abrasive sheets by light scattering and self-shadowing methods

C. ŁUKIANOWICZ

Technical University of Koszalin, Racławicka 15-17, 75-620 Koszalin, Poland

J. IAQUINTA

French Public Works Research Laboratory, 58 Boulevard Lefebvre, F-75732 Paris Cedex 15, France

Abrasive instruments in the form of sheets and rolls are often used in industrial processes. Hence, the quality of the related work is entirely associated with the roughness of their surfaces. In order to characterize the topography of the latter, the optical techniques are employed. In the present paper, the methods based on light scattering and self-shadowing phenomena are presented. Unlike other procedures, such methods can be applied to very rough surfaces of inhomogeneous optical properties. Details about some experimental investigations are given for abrasive sheet samples with different grain sizes. The results suggest that the approaches proposed are really efficient in assessing the textural characteristics of abrasive sheets.

Keywords: *surface topography, abrasive sheets, light scattering, self-shadowing*

1. Introduction

Nowadays such instruments as grinding wheels, abrasive sheets and rolls are commonly used in manufacturing processes. Many important features of the abrasive instruments are determined by the topography of their surfaces [1]. Usually the latter is estimated by means of stylus and optical profilers [2, 3], which allow a close mapping of roughness [4]. However, operation of profilers is rather time-consuming. Sometimes, as an example of using or manufacturing the abrasive tools, a quick estimation of the surface topography may be necessary. Then the measurement of the speed is carried out rather than the exactness of the mapping.

Light scattering methods have been used for a long time to study the surface roughness [5, 6]. Generally, only smooth objects with high asperities ranging from ca. 1 to 2000 nm can be considered. Basically, such methods are adequate for manufactured surfaces. There are two reasons that restrict using these techniques for the abrasive instruments. First, the amplitude of surface roughness considerably exceeds the measuring range. Second, an assessment of topography by light scattering usually requires are optical homogeneity of a test surface. However, most abrasive instruments contain miscellaneous components, grains plus bond, and thereupon do not fulfill the basic assumptions.

Nevertheless, among the available light scattering methods, those exploiting self-shadowing phenomena can be used for very rough and optically heterogeneous surfaces.

The aim of this article was to present basic principles of evaluating the topography of surfaces based on light scattering and self-shadowing phenomena and to describe the experiments conducted. We think that these approaches are useful and reasonable to rough and heterogeneous surfaces. The methods mentioned besides abrasive machinery may typically be applied in stone and asphalt pavements of the roads, matured concrete, composite materials, etc.

2. General relations

The theories that describe light scattering by a rough surface usually assume the entire and direct illumination by the incident light. However, such situations are rarely encountered. Other parts of the surface itself may screen from some areas from the light (Figure 1). This phenomenon is called the surface self-shadowing [7, 8].

Let the light plane wave form the angle θ_i with a rough surface defined by $z = f(x)$ in the (x–z) plane. Consider the surface self-shadowing in the whole illuminated area. In geometrical optics approximation, we can write that the surface self-shadowing occurs if any of the following inequalities is satisfied at any point of the illuminated area:

$$- z'(x) = -\frac{df(x)}{dx} > \cot \theta_i \,, \tag{1}$$

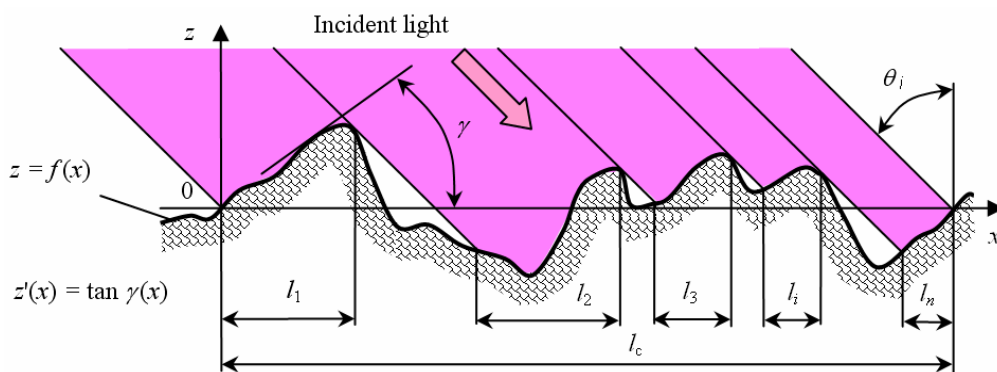$$z'(x) = \frac{df(x)}{dx} > \cot \theta_i \,. \tag{2}$$

Fig. 1. Determination of illuminated and self-shadowed surface areas

Equation (1) specifies the condition for the occurrence of the surface self-shadowing if the system of coordinates is defined as shown in Figure 1. The condition for the surface self-shadowing described by relation (2) is definite when the direction of the *x*-axis is reversed compared to Figure 1. Shadowed regions will appear on a rough surface when any of the relations (1) or (2) is satisfied.

The points on the surface can be illuminated or shadowed, depending on the angle of light incidence, height and slope of the surface. Estimation of the shadowed regions and the related segments l_i shown in Figure 1 is straightforward for periodical surfaces. According to [7] and [9], in a given point of the random surface, the probability $P(\theta_i)$ of its illumination by a plane light wave whose incidence angle is θ_i may be expressed as follows:

$$P(\theta_i) = \frac{\sum_{i=1}^{n} l_i}{l_c} = S(\theta_i, z') \int_{-\infty}^{\cot \theta_i} p(z')dz',$$

(3)

where l_i is the projection length of the illuminated regions of the profile $f(x)$ on the *x*-axis, l_c is the total length of illuminated regions along the *x*-axis, $S(\theta_i, z')$ is the shadowing function, z' is the derivative of the rough surface along the *x*-axis, and $p(z')$ is the probability density of the surface derivative along the direction *x*.

The shadowing function $S(\theta_i, z')$ may be interpreted as the probability of the plane light wave illuminating from the direction θ_i a given point of the rough surface wherein slope is equal to z'. This probability does not depend on the ordinate *z*, nor on higher-order derivatives. Given the rough surface, $S(\theta_i, z')$ is a function of the angle θ_i of light incidence and the first-order derivative $z'(x) = \tan \gamma$ only.

The shadowing function may take a more general form if we take into account the fact that surface self-shadowing can occur when the surface reflects light back (Figure 2). This kind of surface self-shadowing occurs if light reflected (or scattered) cannot be directly observed because neighbouring surface irregularities screen the eye or detector.

The two kinds of self-shadowing are shown in Figure 2. Region *A* is in the shadow regarding incident light, and region *B* (yet properly illuminated) is not seen by the observer or a photodetector.

Based on the above considerations we can conclude that the surface topography may be obtained by analysing the shape and size of the shadowed areas. In [10], a similar technique was applied to evaluation of the surface roughness on the inside surface of a small hole.

Other approaches also take advantage of shadowing phenomena to estimate the surface texture. For instance, in the methods based on the shadow-hiding opposition effect [11, 12] the surface is observed from a direction close to that of illumination (Figure 3). The angular distribution of light intensity is measured at small angles near

the retro-illumination direction. Results of the topography assessment of the abrasive sheets obtained by this method are reported in [13].
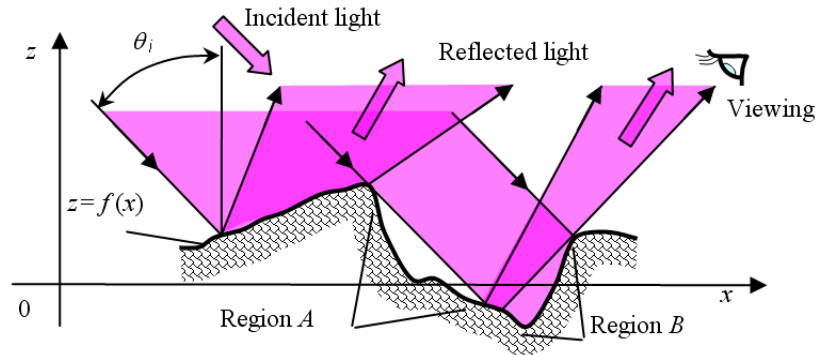

Fig. 2. Asperities casting shadows onto region *A* (where there is no direct illumination), and region *B* (reflecting light) is hidden from the sight
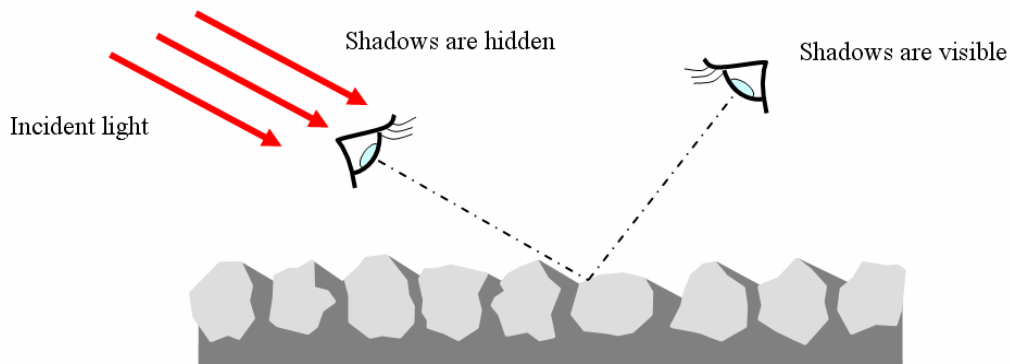

Fig. 3. The shadows are hidden if the direction of observation is close to that of lighting

The results of a topographic study for abrasive sheet samples are presented below. The investigations were conducted by means of light scattering and stylus methods.

3. Experimental investigations

The aim of the experiments was to obtain a quantitative information about abrasive surface topography by means of light scattering methods and to compare these values with those issued from the stylus. In optical measurements, the results were obtained using two methods that enable us to watch the shadows and bright areas on the sheet surfaces. These are microscopy with oblique illumination of the surface and dark-field microscopy.

3.1. Samples

Among the standards set for coated abrasives these of FEPA (Federation of European Producers of Abrasives) were chosen since in such a case a grit determines the range of grain dimensions [14, 15]. For instance, according to the definition of the F180 no more than 3% by mass of the grit can have a particle size > 90 μm and at least 94% must be > 53 μm. Unfortunately, it was difficult to have samples in the whole range from 12 to 2500 μm (grain size ranges from 1815 to 8.4 μm) as the roughest or the smoothest items are not common. Accordingly, only a few typical abrasive sheets were considered.

In order to prepare samples, small sectors (20 mm × 20 mm or 30 mm × 30 mm) were cut from 9 inches × 11 inches abrasive sheets. These products were originally designed for general industrial applications where greater backing strength is required, so in the next step the squares were glued on stiff aluminum plaques, painted in black to prevent corrugation and undesirable reflections.

Two sets of eleven samples were made: six of them (P1200, P600, P360, P240, P150 and P100) are from Carborundum Schleifmittelwerke GmbH (Germany), and the remaining five samples (P1000, P800, P400, P220 and P180) come from 3M (USA) in each set. All the samples of the 2nd set were additionally coated with gold for the sake of uniformity and to increase the reflection of light by the surface. The gold-coated items were used in optical investigations as reference samples.

3.2. Stylus measurements

The stylus operating for contact measurement of surface topography is a T8000 type of Hommelwerke (Germany) with the 3D HommelMap Basic software. This software can produce surface plots, contour maps, various statistical roughness parameters and other characteristics of the surfaces under test. The stylus profiler was equipped with a special stage that automatically shifts and positions the sample along the y-axis. The pick-up type TKL 300 without skid was used for collecting data. The measuring range of this pick-up is ±300 μm and the nominal radius tip of its stylus is 5 μm.

The size of the measuring areas is 2.5 mm × 2.5 mm for all the samples. A single profile contains 3971 points, and 251 different profiles were measured.

3.3. Optical set-ups

Two set-ups were operated for the optical assessment of surface topography. Both of them used the invert microscope Neophot 2 made by Carl Zeiss Jena, connected to a computer for image acquisition.

Samples were illuminated with a 100 W white light halogen lamp and the recorded images were analysed with the Image-Pro Plus v. 5.1 by Media Cybernetics (USA) software.

The first set-up allowed us to inspect the surfaces tested and take microscopic pictures. A simple mirror was used as well as the objective Planachromat 2.5×0.045. Images were obtained for oblique illuminations from one direction (with the angles of light incidence $\theta_i \approx 30^o$ and $\theta_i \approx 10^o$) by shifting and tilting the mirror. The configuration of the microscope illuminator and objective is presented in Figure 4.
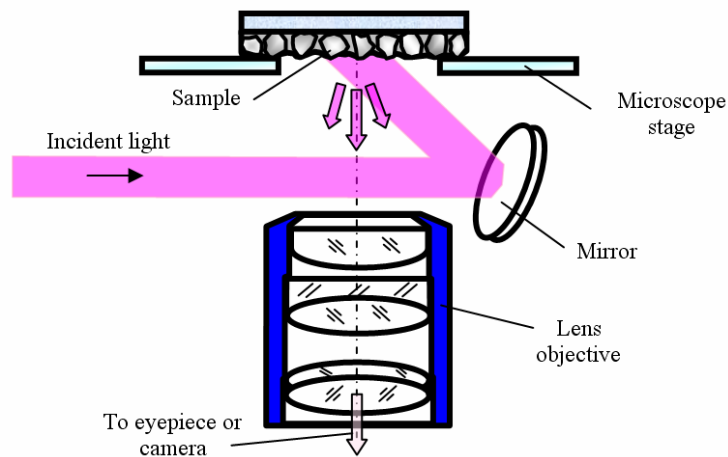

Fig. 4. Configuration of the microscope illuminator and objective
for viewing surface with oblique illumination

The second set-up allows us to look at the samples and to record dark-field microscopic images. The objective Planachromat 6.3×0.12 was utilized. The dark-field images are obtained for lighting at the same time from all directions with a parabolic mirror illuminated by a ring-shaped light beam. Figure 5 shows configuration of the microscope illuminator and objective for dark-field observations.
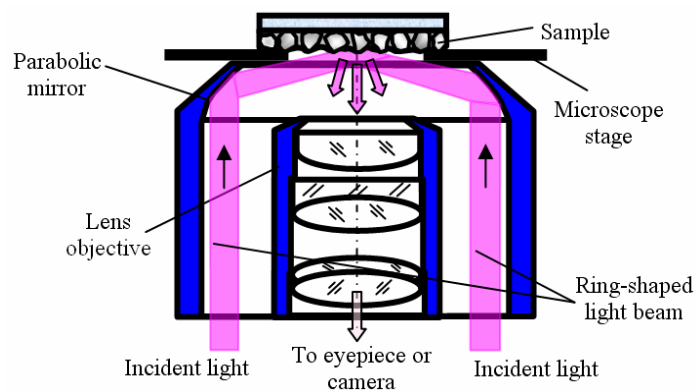

Fig. 5. Configuration of the microscope illuminator and objective for viewing surface in dark field

With these two arrangements the regions of the test surface, which reflect and scatter the incident light, can be seen within the space contained in the aperture angle of the microscope objective. The basic difference between the 1st and the 2nd optical set-ups lies in the way the surface is lit: in the former the sample is illuminated from one direction (which can be controlled), whereas in the latter the surface is illuminated from all the directions simultaneously (the angle of light incidence on the test surface is constant). Using the 2nd set-up we can rotate the microscope stage together with the test sample about the optical axis of the objective, but the images that can be seen in the eyepiece of the microscope are practically invariable. This is the major advantage of the dark-field method for an application to inhomogeneous surfaces. This is a significant result for the practical use of the method.

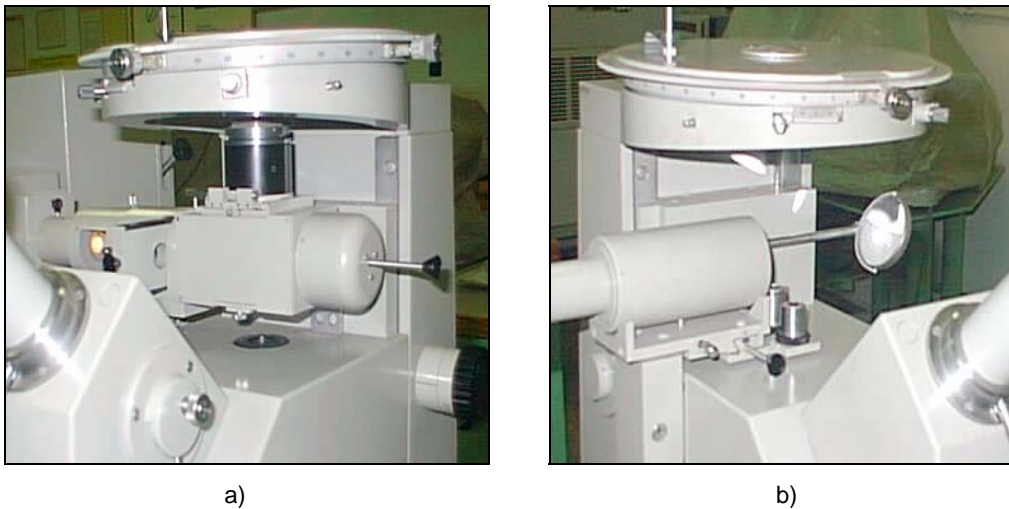a)   b)

Fig. 6. Views of the microscope illuminators and objectives for the first (a)
and the second (b) optical set-ups

Overall views of the microscope illuminators and objectives for both optical set-ups are shown in Figure 6.

3.4. Results

Experiments were conducted on the abrasive sheets with a stylus profiler and the two optical set-ups described above. Stylus measurements possibly provided the most comprehensive information about the actual topography of the surfaces; accordingly, these data will serve as reference in the rest of the study.

Figure 7 displays some results of the surface topography investigations of the abrasive sheets obtained by the stylus instrument. A 2500 μm × 2500 μm three-dimensional plot of the P180 (3M Wetordry) sample measured with the stylus profiler is

shown in Figure 7a. The values of the calculated surface parameters S_a, S_q and S_t are 18.3 μm, 23.7 μm and 181 μm, respectively. S_a is the arithmetic mean deviation of the surface and S_q is the root-mean-square deviation of the surface. S_t is the total height of the surface. Similar results were achieved for all the samples investigated.
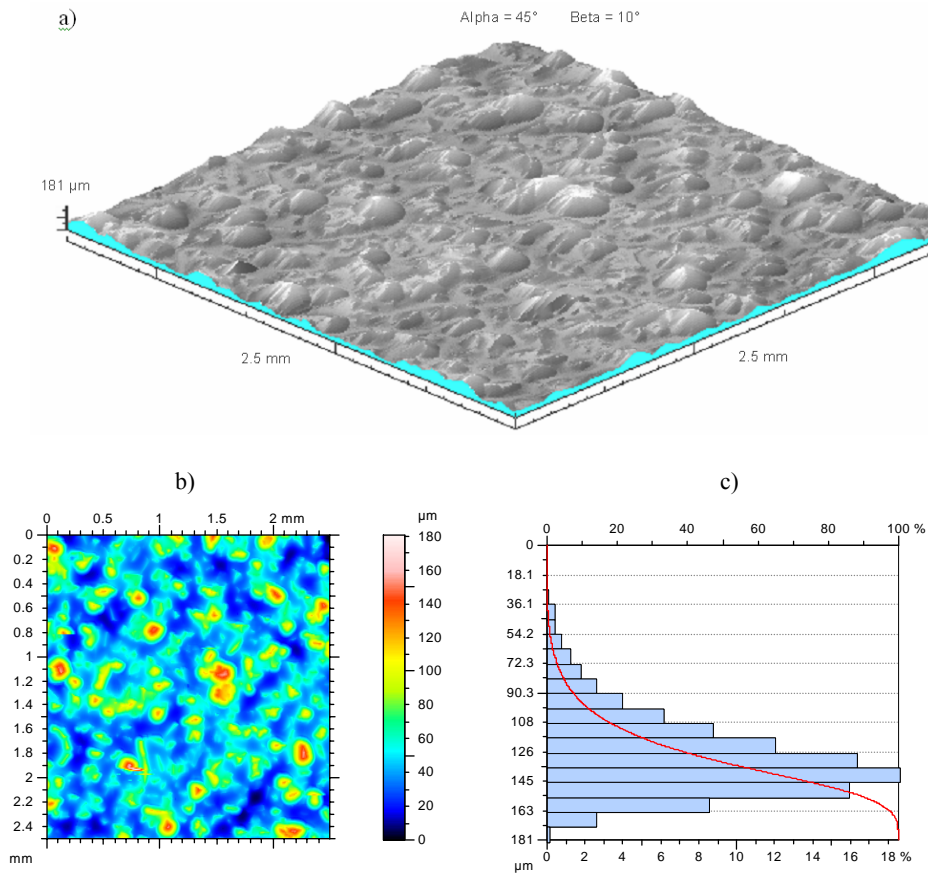

Fig. 7. Results of stylus measurements obtained for sample P180: (a) continuous three-dimensional representation of the surface, (b) greyscale map, (c) the Firestone–Abbott curve

The following figures illustrate the optical investigations of the abrasive sheets. In Figure 8, the results obtained by means of the 1st optical set-up with oblique illumination at various angles of light incidence are given. Figures 9 and 10 show the dark-field microscopic images obtained using the 2nd optical set-up.

An analysis of the microscopic images presented in Figure 8 indicates that their brightness increases at small angles of light incidence. In other words, the values of the probability $P(\theta_i)$ in Equation (3) are higher when the angles of light incidence are smaller. As a result from Figure 9, the dark-field microscopic images of the uncoated

samples are optically a little more inhomogeneous than the same images of the gold-coated ones.
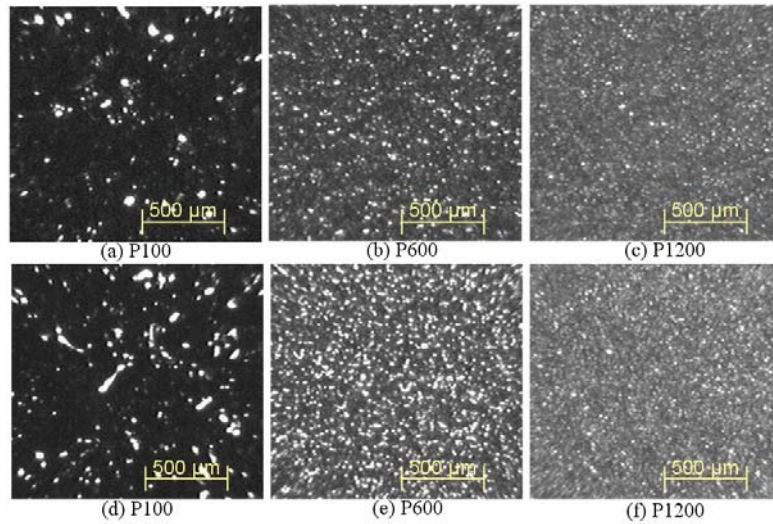

Fig. 8. Microscopic images of the surfaces P100, P600 and P1200 obtained using the first optical set-up with oblique illumination: (a), (b), (c) at the angle of light incidence $\theta_i \approx 30^o$ and (d), (e), (f) at the angle of light incidence $\theta_i \approx 10^o$
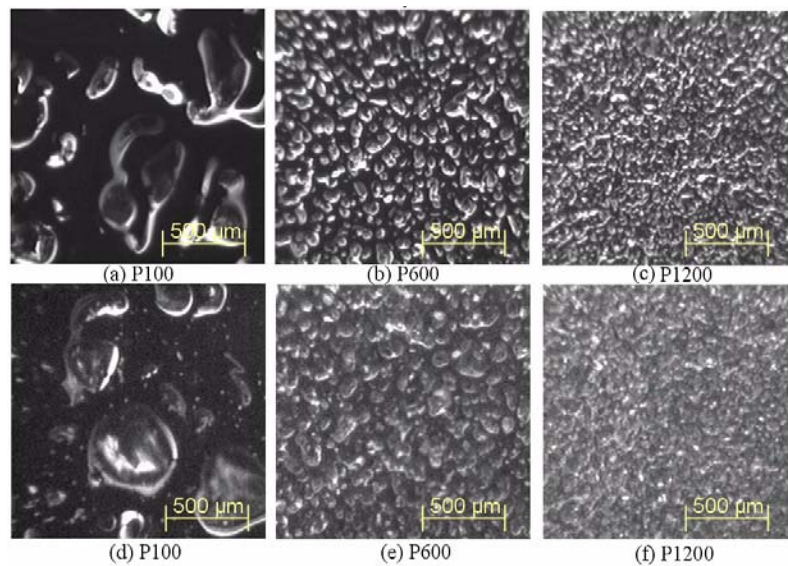

Fig. 9. Dark-field microscopic images of the surfaces for gold-coated (a), (b), (c) and uncoated (d), (e), (f) samples P100, P600 and P1200 obtained with the second optical set-up
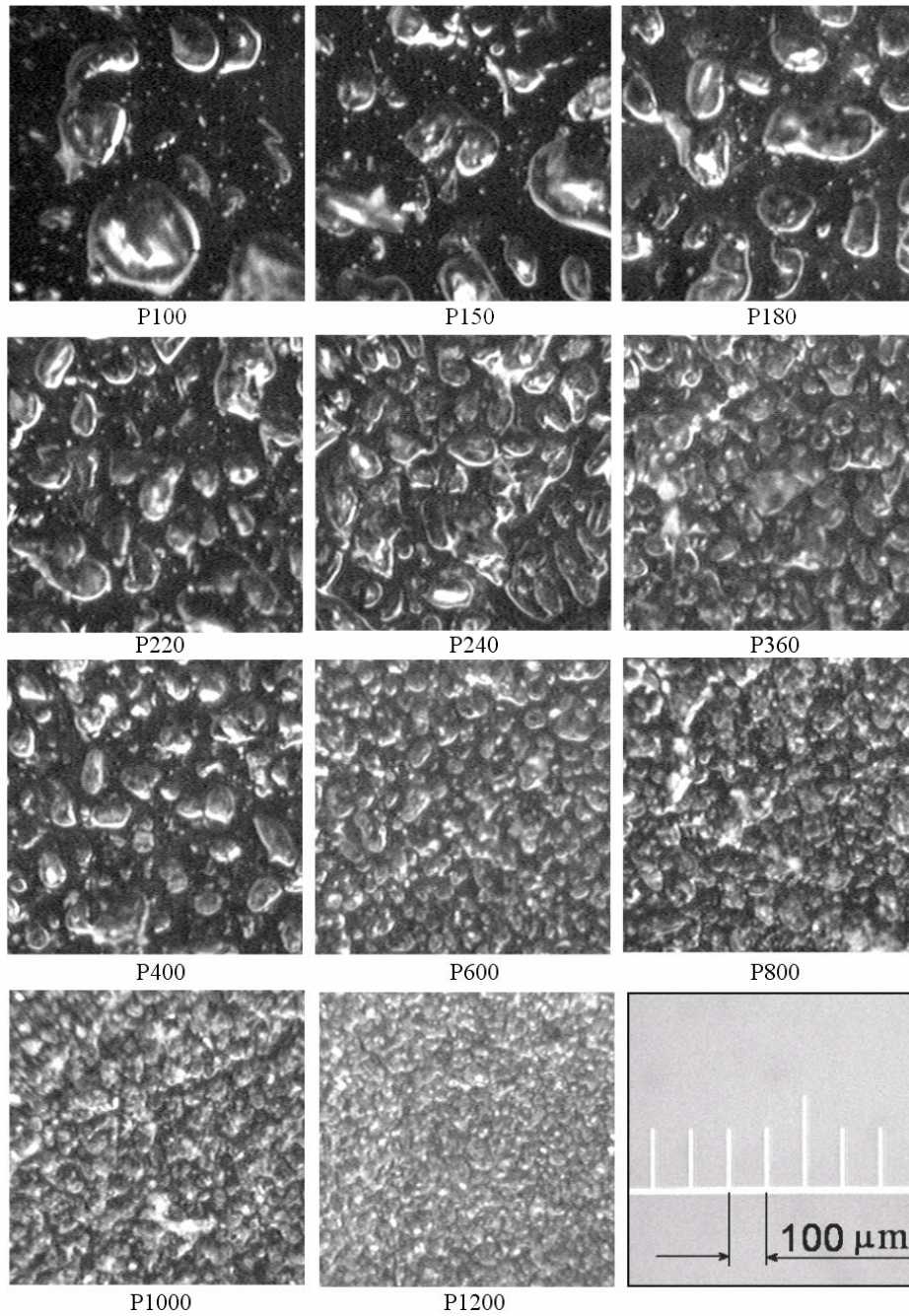
Fig. 10. Dark-field microscopic images of the surfaces obtained with
the second optical set-up for all samples

A quantitative assessment of the probability $P(\theta_i)$ determined by Equation (3) was based on the computation of the integrated optical density (IOD). We have assumed that the value of the IOD is proportional to the probability $P(\theta_i)$. Calculations of the IOD were made for all the microscopic images recorded by the first and the second optical set-ups. Such images obtained under the dark-field microscope for uncoated samples are shown in Figure 10, for example.

All the images were processed with the Image-Pro Plus program to obtain the IOD. The first step consisted in automatical finding and counting the bright spots (objects) that are visible in the image. The area and IOD of each bright object were calculated in the next step. The IOD is equal to the product of the object's area and average optical density of the object. The last procedure in our algorithm was to sum all the values of the object areas and IOD previously calculated for all the bright objects. For example, in Figure 11 a part of the image with the bright objects and final results obtained for the sample P150 are shown.

The IOD was computed only for the bright objects in the images whose optical density was larger than a given threshold. The threshold value was automatically calculated after analyzing the intensities of the objects and background. The values of the surface parameters measured by the stylus instrument and those of the IOD obtained by different optical techniques are given in the Table. In Figure 12, IOD values are plotted as a function of the mean diameter of the abrasive grains for three data sets. In each case, the correlation was estimated by the last square method.
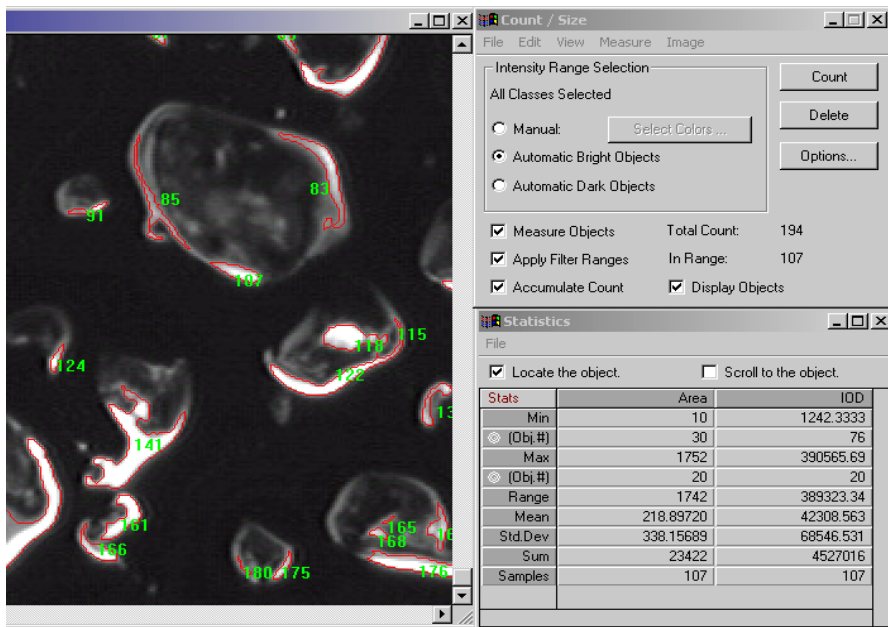

Fig. 11. Results of the analysis of the integrated optical density for the sample P150

Table. Results of measurements of the abrasive sheets

Grit No.	P100	P150	P180	P220	P240	P360	P400	P600	P800	P1000	P1200
d (μm)	162	100	82	68	58.5	40.5	35	25.8	21.8	18.3	15.3
S_a (μm)	33.4	27.0	18.3	18.7	19.0	13.1	10.4	7.24	7.67	7.59	4.30
S_q (μm)	43.1	33.9	23.7	23.8	23.9	16.5	13.5	9.27	9.71	9.53	5.46
S_t (μm)	454	349	181	173	164	114	107	76.3	77.7	77.2	54
IOD 30	1564	1784	1912	2082	2105	2152	2092	2437	2180	3435	4131
IOD 10	2488	2687	2805	3137	3217	4104	3706	6557	4198	5049	7757
IOD Du	4102	4659	4995	5458	5104	5511	6145	7373	7870	9200	10633
IOD Dc	4257	4527	4986	4861	6244	6920	7013	8814	7935	8499	10306

d is mean diameter of the abrasive grains;
S_t is total height of the surface;
S_a is arithmetic mean deviation of the surface;
S_q is root-mean-square deviation of the surface;
    IOD 30 and IOD 10 are integrated optical densities (in arbitrary units) measured in optical set-up with oblique illumination at angle of light incidence of 30° and 10°, respectively;
    IOD Du and IOD Dc are integrated optical densities (in arbitrary units) measured in the dark-field optical set-up for uncoated and gold-coated samples, respectively.
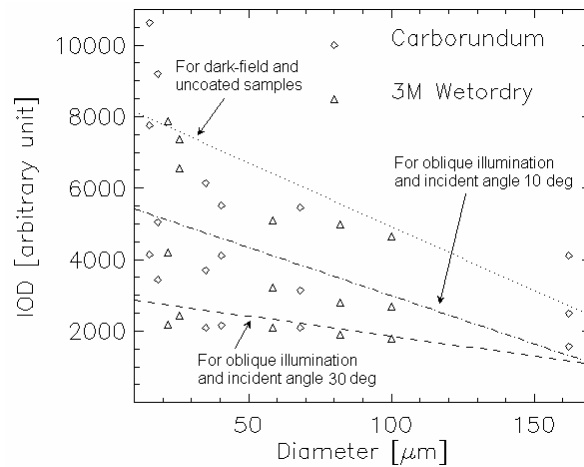

Fig. 12. Integrated optical density versus mean diameter of the abrasive grains for the surface images of the abrasive sheets obtained by different microscopic techniques

    IOD values in two sets of points were obtained for oblique sample illumination. For the third set of points the IOD measured by dark-field techniques was determined.
    Comparing these graphs we can presume that the dark-field microscopy is the most sensitive among the three optical methods investigated. The additional advantage of this technique is that the images recorded are independent of the sample rotation about the objective axis.

4. Conclusions

In this paper, we have described optical methods for assessing the surface topography characteristics. This approach may be regarded as an alternative to stylus instruments, basically for applications where a fast and global (not a profile) answer is sought.

The validation was achieved experimentally on the samples of abrasive sheets. However, there is evidence to claim that both light scattering and self-shadowing methods can be favourably applied to other strongly rough and inhomogeneous materials. Such surfaces include stones, pavements, concrete, asphalt roofing, composites, etc.

Dark-field microscopy proved to be an extremely promising and sensitive system. Integrated optical densities of bright regions, which are highly correlated with surface texture, were computed in dark-field images. We suppose that this measurement can be made, if needed, with a simpler set-up for practical uses.

References

[1] Dąbrowski L., Marciniak M., Oczoś K.E.: *Cutting surface of the grinding wheel as a component of tribological system*, Archives of Civil and Mechanical Engineering, 2002, Vol. II, No. 1, 47–59.
[2] Whitehouse D.J.: *Handbook of Surface Metrology*, Institute of Physics Publishing, Bristol, 1994.
[3] Stout K.J., Blunt L.: *Three-Dimensional Surface Topography*, Penton Pres, London, 2000.
[4] Oczoś K.E., Liubimov V.: *Struktura geometryczna powierzchni. Podstawy klasyfikacji z atlasem charakterystycznych powierzchni kształtowanych*, Oficyna Wyd. Politechniki Rzeszowskiej, Rzeszów, 2003.
[5] Bennett J.M., Mattsson L.: *Introduction to surface roughness and scattering*, Optical Society of America, Washington D. C., 1989.
[6] Stover J.C.: *Optical Scattering: Measurement and Analysis*, McGraw-Hill, New York, 1990.
[7] Bass F.G., Fuks I.M.: *Wave Scattering from Statistically Rough Surfaces*, Pergamon, Oxford, 1979.
[8] Ogilvy J.A.: *Theory of Wave Scattering from Random Rough Surfaces*, Adam Hilger, Bristol, Philadelphia and New York, 1991.

[9] Łukianowicz C.: *Podstawy pomiarów nierówności powierzchni metodami rozpraszania światła*, Wyd. Politechniki Koszalińskiej, Koszalin, 2001.

[10] Zhang Z., Bryanston-Cross P.J., Whitehouse D.J.: *Reconstructing a shadow pattern image of the internal surface of a small hole and estimating surface roughness from the image*, Optical Engineering, 1997, Vol. 36, No. 8, 2210–2215.

[11] Iaquinta J., Fouilloux A.: *Modeling of light scattering by rough surfaces with relevance to pavements monitoring sensors*, Optics and Lasers in Engineering, 2004, Vol. 41, Issue 5, 687–702.

[12] Iaquinta J., Fouilloux A.: *A differential scattering probe for monitoring road surfaces*, Measurement Science Review, 2003, Vol. 3, Sec. 3, 107–110, http://www.measurement.sk.

[13] Iaquinta J., Łukianowicz C.: *Inferring texture from shadows*, Int. Conf. Measurements 2005, Smolenice (to be published).

[14] ISO 6344-1:1998: *Coated abrasives - Grain size analysis* – Part 1: *Grain size distribution test*, ISO 6344-2:1998: *Coated abrasives - Grain size analysis* – Part 2: *Determination of grain size distribution of macrogrits P12 to P220*.

[15] 43-GB-1984 R1993: *FEPA standard for coated abrasive grains of fused aluminium oxide and silicon carbide*. http://www.fepa-abrasives.org

Ocena topografii powierzchni arkuszy ściernych za pomocą metod rozpraszania światła i samozacieniania powierzchni

Narzędzia ścierne stosowane w operacjach szlifowania często mają postać arkuszy lub taśm ściernych. Topografia powierzchni arkuszy i taśm ściernych jest ważnym czynnikiem określającym jakość tych narzędzi. Przedstawiono możliwości wykorzystania metod optycznych do szybkiej oceny topografii powierzchni arkuszy ściernych. W metodach tych wykorzystano zjawiska rozpraszania światła i samozacieniania powierzchni. W odróżnieniu od innych metod optycznych mogą one służyć do oceny powierzchni o niejednorodnych właściwościach optycznych i dużej chropowatości. Zamieszczone wyniki badań eksperymentalnych, wykonanych na arkuszach ściernych o różnych wymiarach ziaren ściernych, wskazują na dużą przydatność tych metod.

Some macro- and microstructural aspects of pad welded layer durability

G. PĘKALSKI, W. DUDZIŃSKI, U. SACHADEL

Wrocław University of Technology, Wybrzeże Wyspiańskiego 25, 50-370 Wrocław

J. ALENOWICZ

Poltegor Institute of Opencast Mining, Parkowa 25, 51-616 Wrocław

The results of macroscopic and microscopic investigation, hardness tests and abrasive wear out tests of different pad welded layers made with thirty nine kinds of electrodes are presented. Defectiveness of the layers was connected with a foreseen character of their wear out. The possibility of simplifying the chemical composition of electrodes without deterioration of application properties of pad welded layers was shown. The paper was focused on the investigation results of pad welded layers applied in opencast lignite mining and in power industry.

Keywords: *pad welded layers, structures, defects, hardness, abrasive wear*

1. Introduction

Methods of pad welding are applied in all the stages of exploitation, transport, preliminary processes and in lignite combustion. Bucket-wheel teeth in excavators, track links, digging chain links, discharge hoppers and other machine elements are pad welded. The layers are applied in coal pulverizers (e.g. plasters, pans). They are also used as the covering of screening pipes in energy boilers protecting them from erosion–corrosion. Pad welding technologies are used for the production of new elements (e.g. pad welding of bucket-wheel chute made of non-alloy steel, bucket teeth). More frequently, however, they are regeneration and maintenance technologies.

The review of pad welding electrodes offered by various producers (even limited to our own research) indicates that currently an important problem of exploiters is a rational choice of electrodes and pad welding methods in the context of their application and cost. At first pad welding was treated mainly as a method of increasing the resistance to the abrasive wear out. Currently it is known that it is one of a range of factors that should be considered while selecting a padding weld. For example, the character of wear out and its changeability in relation to time and temperature, resistance to erosion–corrosion, presence or lack of dynamic load threat, etc, should be taken into account.

It should be noticed that abrasive resistance is determined by the implementation of two major non-alternative directions. The first is ensuring high hardness of the padded layers. The other is producing a phase composition of a heterogeneous welding,

strictly determined for given wear out conditions [1]. The above implication is only approximate as high hardness is only one of the abrasive resistance measures. The padding weld structure does not depend exclusively on the chemical composition of electrodes but also on the pad welding conditions (kind of a base material and its preparation before welding, current, pad welding and self-cooling rate, the number and thickness of layers). The book [2] dealing with alloy cast iron (of chemical composition similar to some padding welds) contains information that in the case of three components of metallic matrix (without considering their per cent ratio and their form) the number of structure variants equals 70. Thus, the padding welds made with the same electrode in differing variants can reveal very different structures and, consequently, service conditions. Since 'many variables' affect macro- and microstructures of the padding welds, the forecasting of their service features is a sophisticated task which should be preceded by a 'laboratory strategy' implementation and comprehensive metallographic studies.

The article is based on the results of research carried or co-carried out by the authors. That is why the data presented in Table 1 are not the review of electrodes used in lignite industry. They only allow a comparison of electrodes as well as description and interpretation of the padding welds features analyzed for several years.

In papers [3–5], it was proved that a good starting point for the analysis of padding welds structure is their structure in equilibrium state. That is the reason for their classification into three groups (basic structures):

I. Layers of ferritic-pearlitic matrix.
II. Layers of alloy ferrite matrix.
III. Layers of alloy austenite matrix.

In conditions of not equilibrium self-cooling, they can obviously reveal other structures (ferritic, bainitic, martensitic or being conglomerates of various structures). They usually contain precipitates of intermetallic phase (mostly carbides).

Table 1. Kinds of electrodes for pad welding

Group	No.	Electrode designation	HRC padding weld hardness	Chemical composition [%]									
				C	Cr	Mn	W	Mo	V	Nb	Si	B	Other
1	2	3	4	5	6	7	8	9	10	11	12	13	14
I	1	EN-200	191 HB	0.15	0.01	0.59	–	–	–	–	0.36	–	–
	2	Lincore 40-O	40	0.2	3.5	1.5	–	0.4	–	–	0.7	–	Al=1.8
	3	CS-400	387 HB	0.35	2	–	0.2	–	–	0.15	–	–	Al=0.7
	4	EN-600	58–48	0.3	5.3	–	–	–	–	–	1	–	–
	5	EN600B	50–55	0.6	5.6	1.4	–	–	–	–	1.2	–	–
II	6	EstelMoNb60	67–60	5.3	2.9	1.3	–	7.7	–	–	1.5	–	–
	7	ENSW2MoB	63	0.9	5.4	1.6	2.2	6.8	–	–	1.1	–	
	8	PD11	60	2	7	–	12	3	2	–	–	–	–
	9	DPT6	52–44	3.9	7	–	–	–	1.2	–	2.9	–	–

1	2	3	4	5	6	7	8	9	10	11	12	13	14
II	10	WSER23 or E	48–45	0.9–1.1	7.5	–	11	–	–	–	0.6	0.3 –0.4	–
	11	DPS11	51	0.5	8.5	–		0.6	–	–	1	–	Ti=0.15
	12	EB3	>58	0.8	10	–	4	4	4	–	–	0.15	–
	13	DIPS14/3	61–58	4.3	10.1	–	–	–	1.2	–	3.7	–	–
	14	PMFeCr65	65	1	10.5	–	–	–	–	–	1	–	–
	15	PD9	62	4.2	10.5	3.2	–	0.2	1.2	–	–	2.8	–
	16	300X9T6	60–48	2.5	11.6	–	–	–	4.4	–	1.5	–	Ti=2.4 Al=0.2
	17	WJA	36	1.1	12	–	13	–	1.7	–	–	–	–
	18	DPS14	51	0.8	13	–	–	–	–	–	0.9	1.7	Cu=1.7
	19	PD1	44–38	0.8–1.4	15–18	–	–	–	–	–	–	–	–
	20	350H16	62–51	3.5	16	–	–	–	–	–	–	–	–
	21	382	62	4.7	17	1	–	–	–	–	–	–	–
	22	Castolin XHD–6715	64–31	3.5–4.0	17–23	–	6.0–9.0	6.0–9.0	–	6.0–9.0	–	–	–
	23	DPS47	62–51	3	18	–	–	1	–	–	–	–	–
	24	DPT6	57–51	2.9	18.6	1.8	–	–	–	–	1	–	–
	25	Cintrac 650C	61–36	2	19	2.5	7	5	1				
	26	DIPS9	55–41	4.2	20.5	1.4	–	0.2	–	–	–	–	–
	27	Gidur 65	58–48	5	21	–	6	8.5	–	7	–	–	–
	28	CN–O	60–40	5.98	21.1	1.36	–	–	0.7	–	0.39	–	Nb = 6.5
	29	EA	41	1.2	23	–	–	–	–	–	–	–	Ti = 1.2
	30	EP3600H2 4V9	65–67	5.5–6.0	24	–	–	–	10	–	–	–	–
	31	Abradur 64	52–34	7	24	–	–	–	–	7	–	–	–
	32	EH–UTC–02	58–33	3.5–5.0	26.0–30.0	4.6–6.0	–	1.7–3.2	–	–	1.5	1.0–1.6	–
	33	EstelMn60	61–37	5	31.6	3	–	–	–	–	1.7	–	Ni=0.3
	34	Abradur 58	52–34	3.6	32	–	–	–	–	–	–	–	–
	35	Castolin 6006	61–39	3.5–4.0	32.0–35.0	–	–	0.7–0.9	–	–	1.0–1.3	–	Ni=0.3–0.5
	36	PMFe60P	62–58	0.2	40.6	1.2	–	–	0.15	–	2.2	–	–
III	37	Lincore 15CrMn	41–36	0.4	16	15	–	–	–	–	0.25	–	–
	38	Manganese steel	45 (after cold work)	1.1	2	14	–	0.5	–	–	0.5	–	Ni=1.0
	39	DP11G12	54–32	1.1		13.2					0.6		

I – ferritic-pearlitic, II – alloy ferrite + carbides, III – alloy austenite + carbides.

2. Macroscopic defects of padding welds

Contrary to the welded joints, the presence of macroscopic defects (cracks) in padding welds is allowed in working conditions without dynamic loads. In Figures 1–5 and 7–8 macroscopic defects characteristic of pad welded layers are presented. The defects can appear as early as during formation of the layer. Usually they are cracks, pores and gas cavities formed in the process of pad welding and subsequent cooling (Figures 1–2 and 8). They can also be faults in weld penetration resulting from careless technology of pad welding (Figure 3). In the last case, there is high probability of low durability of the layer. In places of the lack of weld penetration there are macrocracks spreading in the form of a network in the padding weld (Figures 2, 4, 5).The cracks in the padding weld sometimes spread through the fused zone into the base material. This can make its regeneration impossible because of the range of the damaged area (padding weld and base material chipping) in early stages of service.
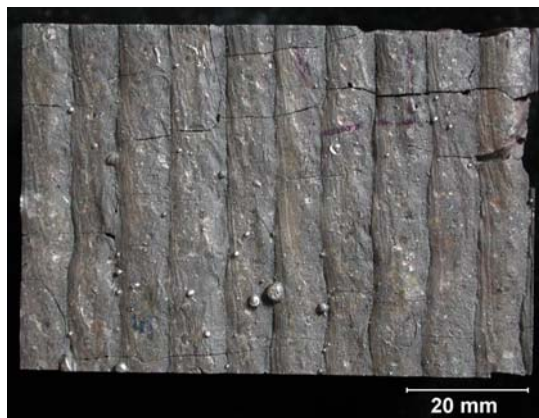
Fig. 1 [6]. Surface of CN–O padding weld before service (coal pulverizer).
Large cracks resulting from cooling after pad welding. This is characteristic
of the work without dynamic loads. Hardness at surface: 64 ± 2 HRC; thickness:
23 mm. This padding weld has survived 14500 working hours in the coal pulverizer

The surface of padding weld (three-layer surface), which has been working in abrasive wear out conditions without dynamic loads for 5500 hours since the regeneration pad welding is presented in Figure 2. Although there is a dense network of cracks penetrating also the base material (Figure 4), the padding weld has fulfilled its functions.

Further service of the construction element, including a padding weld with cracks in the base material, leads to the catastrophic condition of the device. The part of a sample taken from the coal pulverizer with a vast crack originating from the padding weld crack is presented in Figure 5. The separation of the base material parts X and Y revealed that the crack was caused by the material fatigue (Figure 6).

Fig. 2 [7]. Surface of CN–O padding weld after service (coal pulverizer). Three-layer padding weld, regenerated – 14500 working hours (5500 hrs after the last pad welding)

Fig. 3 [8]. Surface of the padding weld in ore crusher. The hardness at the padding weld surface: 591-613 HV_1. Double-layer padding weld – the foundation layer was made with 3302 (E_+C Termotec) electrode – applied in conditions of thermal shocks, loads and corrosion – the foundation hardness before hardening pad welding: ~200 HB and oxidation resistance to 600 ºC. The surface layer was made with self-shielding electrode AN4923 (4923 E_+C Termotec) of Ti, Mo and Cr. Although there is a foundation layer, the padding weld is highly cracked. On the surface there are visible weld penetration faults and cracks other than in Figure 1
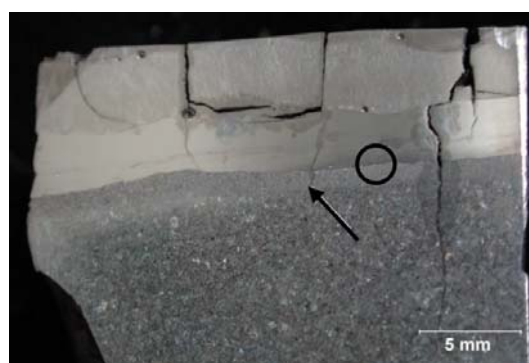
Fig. 4 [7]. Intersection of the sample presented in Figure 2 – deep cracks in the padding weld penetrating to the base material are visible. The lack of weld penetration is also noticeable. Etch. 5% HNO_3
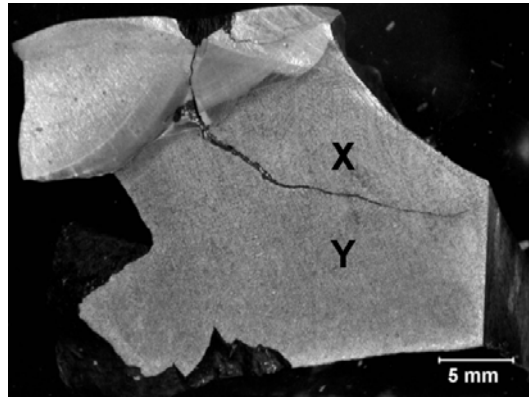
Fig. 5. A part of pad welded coal pulverizer pan. Cracks and chipping in the padding weld and blow holes in the weld penetration zone are visible. A large crack penetrates the base material
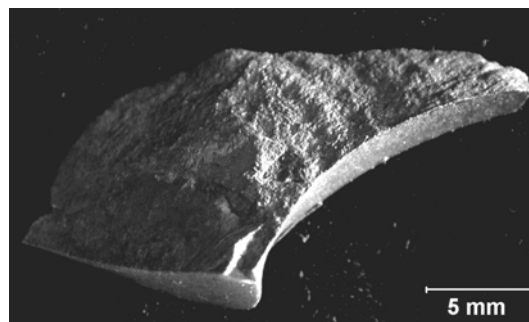
Fig. 6. Macroscopic picture of the fracture surface (part X – Figure 5). Multi-plane fatigue fracture in the padding weld is marked with the rest lines
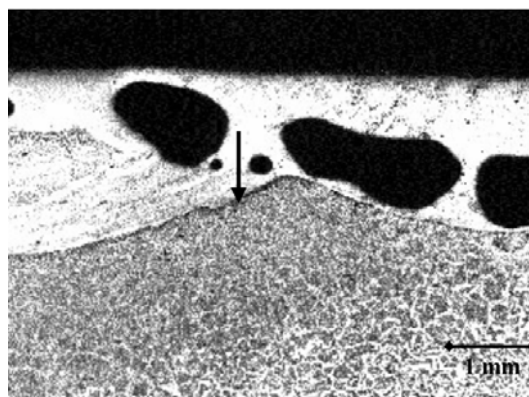
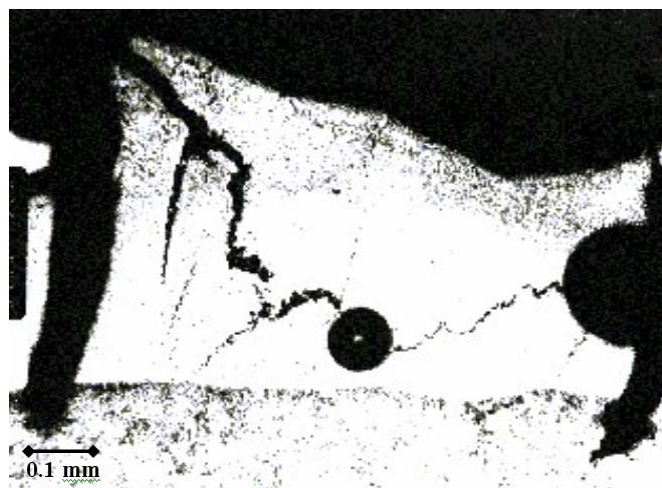Fig. 7 [9]. Blow holes in padding weld DIPS143 (bucket tooth). The arrow points at the local lack of weld penetration. Etch. 3% HNO_3

Fig. 8 [9]. Crack, chipping and blow holes in padding weld DPT-6. Under the operating loads the padding weld has cracked and its fragments are pressed into the base material (bucket tooth). Etch. 3% HNO_3

A dangerous macroscopic defect, resulting in the separation of a layer (a layer part) from the protected surface, is the lack of weld penetration between the padding weld and the base material. The lack of weld penetration was observed also between particular layers of the padding weld.

In most padding welds, there are blow holes, pores and slag inclusions. Their presence usually results from the application of humidified electrodes or fluxes and the presence of pollutants on the pad welded surface. However, the defects rarely are as intense and vast as in Figure 7. Over such intensity of defects, the padding weld durability is very low and wear out time is uncontrollable. Sometimes it is said that high resistance to abrasive wear out can be achieved by pad welding 'soft' materials (steel, cast steel) of low carbon content. The opinion is accompanied with the argument of their good metallurgic welding characteristics. As it is concluded from Figure 8, it is not adequate. The loads carried by the pad welded bucket tooth have resulted not only in fast padding weld cracking (a negative role of blow holes is noteworthy), but also in pressing the padding weld material into the base material and its large damage. Usually large differences in chemical composition of the padding weld and the foundation are the cause of the cracking. In such cases, plastic foundation layers (e.g. austenitic) should be applied. In order to illustrate the issue, characteristic macroscopic defects of padding welds in extreme forms are presented in Figures 1–4 and 7–8. Typically, when the technologies of pad welding are properly developed and repeatedly applied (and the electrodes are accurately selected) the damages are not so intense. The experience gained from the research carried out and service observations indicate that the most serious macroscopic defects are insufficient weld penetrations connected even with single cracks in the whole thickness of the padding weld. In such defect

conditions, there appears fast chipping of the pad welded layer, and thus, it does not fulfill the function of increasing durability of the protected construction element. In no case can the macroscopic defects observed on the external surface of the padding weld be hidden by putting a thin, masking surface layer. Another difficult issue is the ability to evaluate the suitability of padding welds for service on the basis of macroscopic observations (without applying the intersections for the tests). In case of doubts, it is necessary to carry out damaging tests using the most defected fragment of a padding weld.

3. Padding weld structures and their defects

The work [3] reveals that a good starting point of considerations concerning the padding weld structure are adequate ternary equilibrium diagrams. Such a point of view (for the most numerous group of padding welds Fe-Cr-C) is also expressed in [12, 13]. The analysis of the diagrams enables the determination of padding weld structures in equilibrium state and supposed types of carbides. It also makes forecasting of nonequilibrium structures existing in real padding welds reliable. For these reasons, whenever possible, the full annealing of the padding welds studied was conducted, comparing their structure and selected properties (hardness, resistance to abrasive wear out). The examples of padding welds cooled in still air and in the annealed state are presented in Figures 9–12.
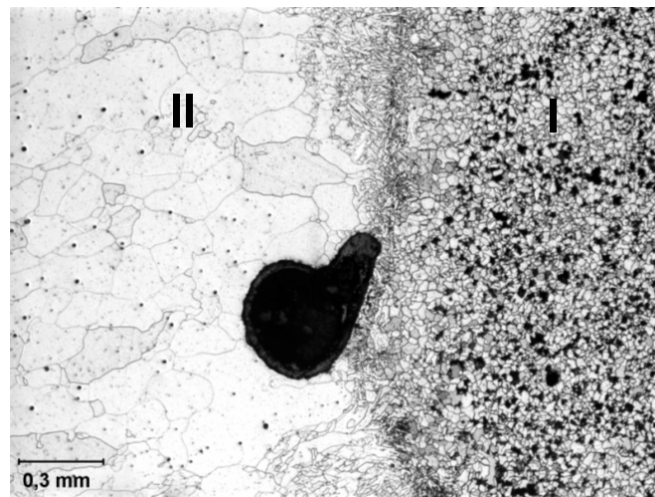
Fig. 9 [4]. Padding weld made with core wire Lincore 40-O – annealed.
I – base material, II – padding weld (ferrite grains with carbides M_3C and aluminium nitrides). Padding weld hardness: ~160 HV_{10}.
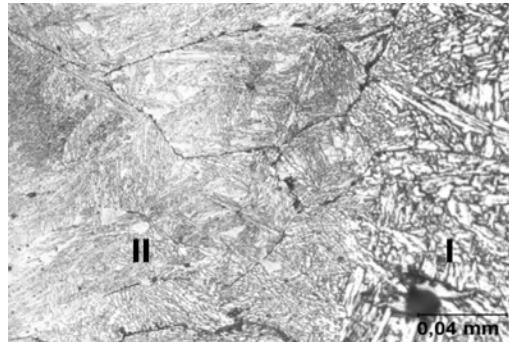Etch. 5% HNO_3. Light microscope

Fig. 10 [4]. Padding weld Lincore 40-O – after pad welding, cooling in still air. I – base material, II – padding weld (low-carbon martensite with bainite and quasi-eutectoid). Maximum hardness of the padding weld on the surface: ~480 HV_{10}. Etch. 5% HNO_3. Light microscope
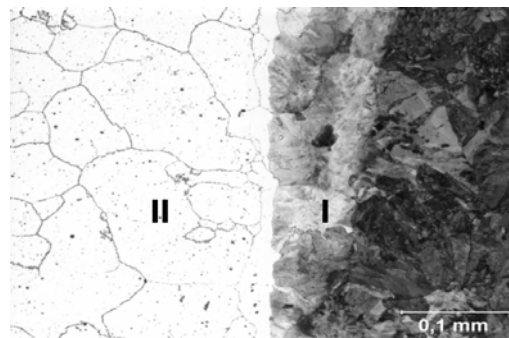

Fig. 11 [5]. Padding weld 15CrMn – annealed. I – base material, II – padding weld alloy austenite with carbide precipitates at grain boundaries and inside the grains. Etch. 3% HNO_3. Light microscope
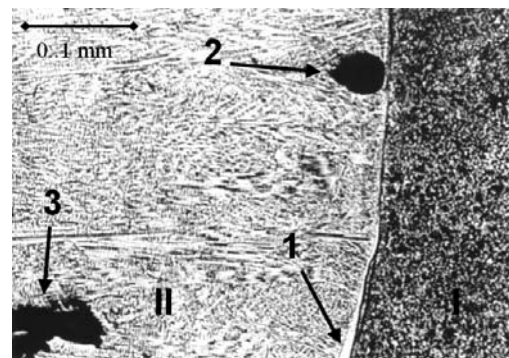

Fig. 12 [5]. Padding weld Lincore 15CrMn – after pad welding, cooling in still air. I – base material, II – padding weld. Dendritic structure of the padding weld consisting of austenite and carbides; 1 – solid solution area of heterogeneous thickness in the weld penetration zone; 2 – blow hole; 3 – final fragment of the crack of the 80% padding weld thickness. Etch. 3% HNO_3. Light microscope

The results of microscopic examination have shown that the structures of real pad-ding welds differ considerably from the structures after annealing. It is also obvious that the application of pad welded layers in the annealed state would not be rational because of low resistance to the abrasive wear out of ferrite (Figure 9) or austenite (Figure 11). In the case of austenitic structure (equilibrium), one should not count on strengthening owing to the plastic deformation or increase in the pad welded element durability, as it would not be high. Thus, the advantage of pad welded layers is their nonequilibrium structure. The rate of padding weld wear out should be close to the set value. It can be concluded from this assumption that it would be the most favourable if the padding welds structures were homogeneous throughout the whole thickness. However, such a structure has never been observed in real life conditions. This con-cerns mostly 'thick' padding welds (e.g. of a few centimeters thickness), where the changeable cooling rates, thermal interaction between the layers and chemical compo-sition differentiation cause the appearance of various structures.
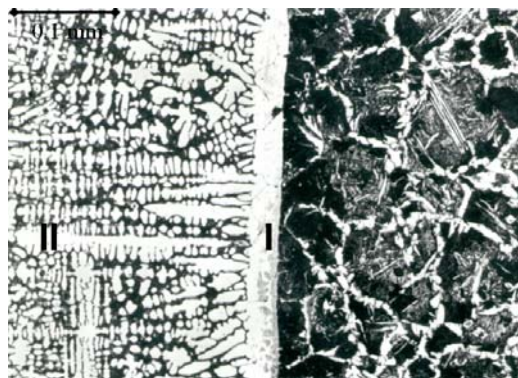

Fig. 13 [10]. Padding weld made with wire DIPS-9. I – narrow zone of alloy ferrite with single carbides; II – dendritic structure of the padding weld consisting of austenite and carbides. The microcracks in alloy ferrite zone are visible. Etch. 5% HNO$_3$. Light microscope

A frequent feature of pad welded layers is the presence of a narrow area of solid solution (ferrite or austenite) in the weld penetration zone on the padding weld side. In such areas, apart from solid solution grains there are usually single carbides. The pres-ence of such areas, especially if they are considerably thick and homogeneous (e.g. ~0.04 mm, Figure 13), should be considered as favourable as they are 'flexible foun-dation-intermediary microlayers' between the base material and hard, relatively brittle padding weld material. Unfortunately, the layers can contain microscopically identifi-able defects. They are characterized by heterogeneous thickness (locally non-existent) and the presence of microcracks, usually along carbidized grain boundaries (Figures 12 and 13). Getting further from the weld penetration zone the dendrites of the solid solution start to appear as well as carbides and solid solution mixtures (eutectic or eu-tectoid) in the interdendritic spaces. The mixtures typically include carbides of $M_{23}C_6$,

M_7C_3 or M_3C types (mostly alloy carbides, e.g. $(Cr, Fe, Mn)_7C_3$). In Figure 18 a structure without defects of solid solution + mixture type is presented. If the electrode for pad welding contains highly carbide forming elements, then the padding weld structure also contains simple carbides of M_2C and MC types (Figures 14–16, 19 and 20). When the padding weld contains enough carbon (when only high abrasive resistance is required) there are observed primary carbide precipitates in the padding
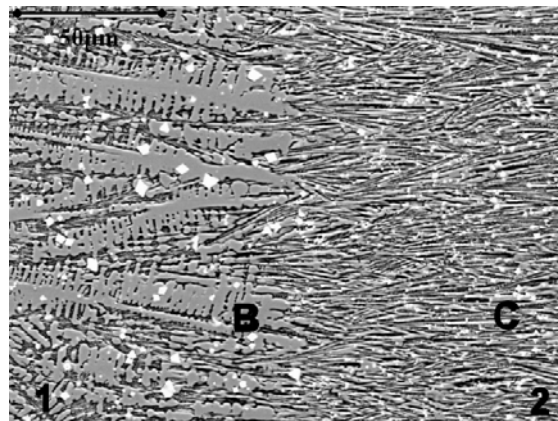
Fig. 14 [7]. Three-layer padding weld CN-O. The zone between the first (B) and the second (C) padding weld layers. Alloy ferrite dendrites with eutectoid mixture in interdendritic areas + NbC carbide precipitates (white). In zone B, the structure is similar to the structure in the weld penetrating zone presented in Figure 13. Good interlayer penetration; fine dendrites in zone C are visible.
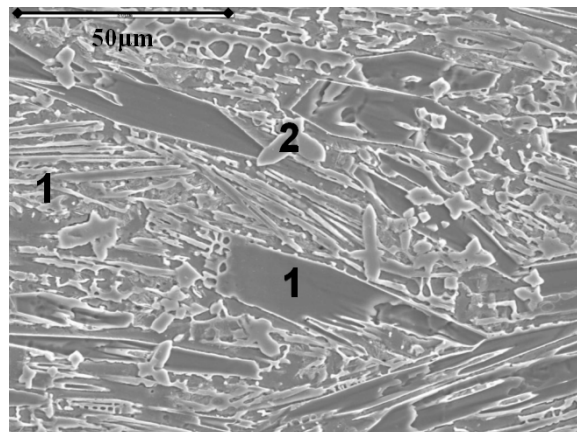Etch. electrolytically with chromic acid. SEM

Fig. 15 [7]. Surface layer of padding weld CN-O. Primary carbide precipitates (1) M_7C_3 {$(Cr,Fe,Mn)_7C_3$} and simple carbides (2) MC {NbC} in the mixture matrix [alloy ferrite + carbides]. Etch. electrolytically with chromic acid. SEM

weld structure (Figures 15 and 16). Their presence can also be a source of padding weld defects in the form of cracks on the interphase boundaries and cracking of the primary carbides themselves. In multilayer padding welds of dendritic structure, the structure differentiation can result from thermal interaction (intermediary weld penetrating zones) between particular layers (Figures 14 and 20). In the structure of the analyzed padding weld group, the most frequent defects are branched transcrystalline cracks and blow holes (Figure 12). Often the defects are local weld penetration shortages, sometimes connected with the presence of blow holes (Figure 9) and branched microcracks in the mixture zone or in interdendritic gaps (Figure 17). A separate and dangerous factor which has an impact on the padding weld hardness is the possibility of microcracks at the interlayer boundaries of primary carbide–padding weld matrix and primary carbides themselves (structure type presented in Figure 16). The number of primary carbides in padding welds is repeatedly highest in surface layers. Thus, the presence of cracks at the boundaries of large primary carbides results in their chipping from the padding weld matrix. In such a situation, instead of the increase in the padding weld durability, there appears its leap decrease connected with the presence of carbides.

The above description of padding welds structure is only one of the observed during our own research (appearing most frequently). From the results of microscopic examination it can be concluded that the padding welds can also have a structure of martensitic type or even more complex, e.g. solid solution, a mixture, martensite and carbides (Figures 10 and 20). The designation "martensitic type" means that martensite dominates in the padding weld intersection. However, in no padding weld has the presence of bainite, trostite or quasi-eutectoid been noticed together with martensite. In the case of martensitic structure, frequent defects are microcracks at the former austenite grain boundaries (Figure 10).
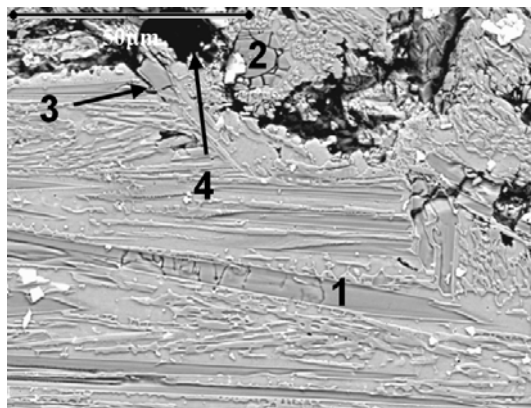

Fig. 16. Surface layer of padding weld CN-O after 5500 hours of work in coal pulverizer (compare Figure 15). Damaged padding weld area: 1, 2 – cracks in primary carbides; 3 – cracks on inter-phase boundaries; 4 – chipping. Etch. electrolytically with chromic acid. SEM
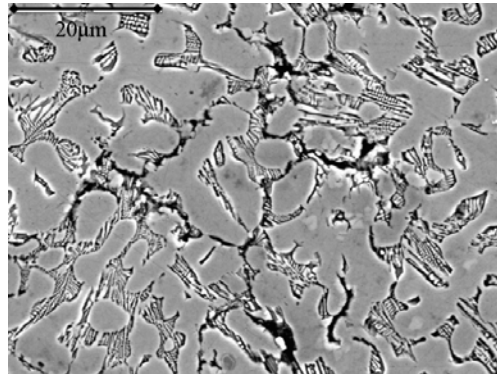
Fig. 17 [6]. Middle zone of padding weld as in Figure 15. Alloy ferrite with a mixture
of ferrite + carbides. Branched microcrack in interdendritic zones is visible.
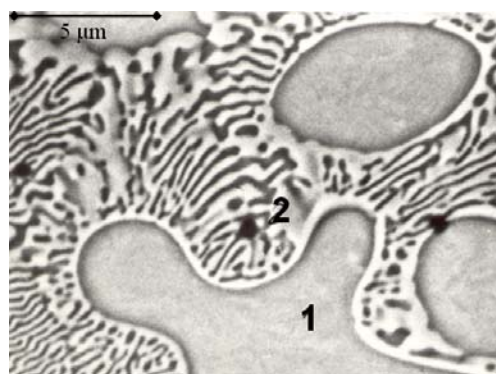Etch. electrolytically with chromic acid. SEM

Fig. 18 [10]. Padding weld made with powder wire PMFeCr65. Alloy ferrite grains (1)
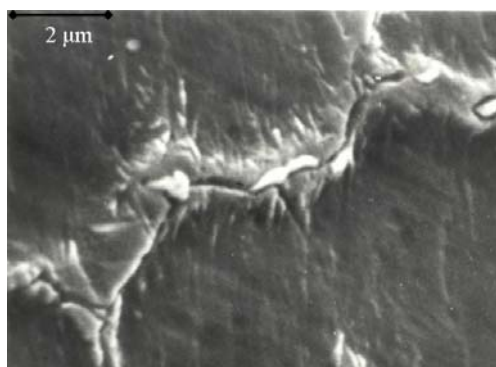and a mixture $[\alpha + (Fe,Cr)_7C_3]$ (2). Etch. electrolytically with chromic acid. SEM

Fig. 19 [10]. Padding weld ENSW2MoB. Molybdenum carbide precipitates at grain boundaries.
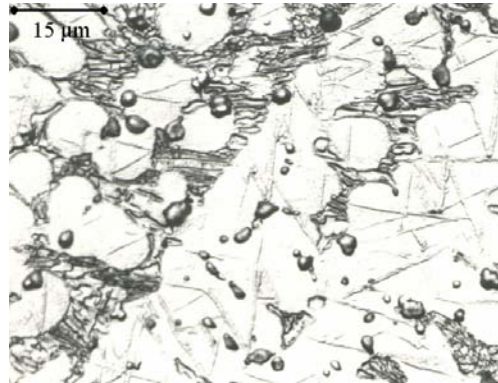Etch. electrolytically with chromic acid. SEM

Fig. 20 [11]. The structure of the middle zone of padding weld EP3600H24V9. Alloy ferrite grains,
fine-dispersive eutectics of lamellar structure and precipitates of fine (spherical) carbides VC.
Inside ferrite grains single martensite spines are visible. Etch. electrolytically. Immersion

Changeability of the structure types revealed during the microscopic examination
has to have an impact on the changeability of hardness at the padding weld intersec-
tion. The changeability, consequently, enables reliable forecast of the wear out rate.
Thus, the macroscopic observation results and detailed measurements of the hardness
at intersections including the padding weld with the base material (even without mi-
croscopic observations) enable the evaluation of the quality of pad welded layers.

4. Diagrams of hardness changes of padding welds

Selected results of hardness profiles on the cross-section of padding weld and base
material are presented in Figures 21–23. The 'drastically negative' results have been
eliminated. They included cases, where it was impossible to conduct measurements
because of macroscopic cracks of the padding weld (Figure 2) or cases with results
distribution exceeding those for electrode DPT-6 in Figure 22. In such cases, the pad-
ding welds should be found as defective and useless for application. The profile pre-
sented in Figure 21 should be analyzed in the context of microstructures presented in
Figures 9 and 10.

In Figure 21, changes in the padding weld hardness in the annealed state and after
cooling 'in pad welding conditions' are presented. The decrease observed in the thick-
ness at the padding weld layer (curve no. 1) should be ascribed to the decreasing ratio
of martensite while receding the measurement place from external surface of the pad-
ding weld. The shape of the measurement curve of the padding weld made with elec-
trode DPT-6, presented in Figure 22, has shown that full repeatability of the results
(full repeatability of the pad welded layer behaviour in service conditions) cannot be
expected even in case of applying the same electrode and pad welding technology. It
is noteworthy that the hardness profiles in the padding weld are quasi-stabilized,
which implies that the wear out process approximates to the stabilization.
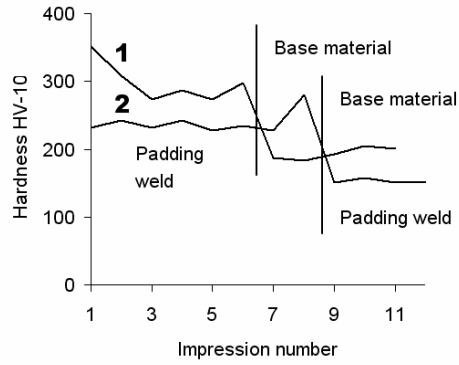
Fig. 21 [4]. Hardness profile in padding weld Lincore 15CrMn and in base material:
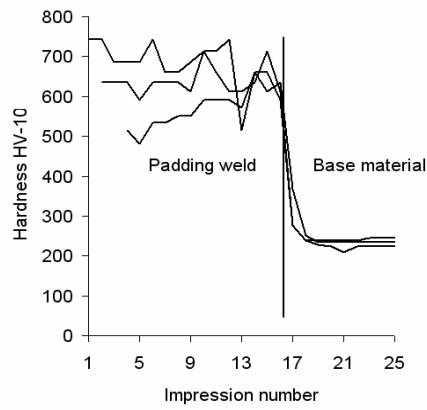1 – after pad welding, 2 – after full annealing

Fig. 22 [8]. Hardness profile in padding weld DPT-6 and in base material
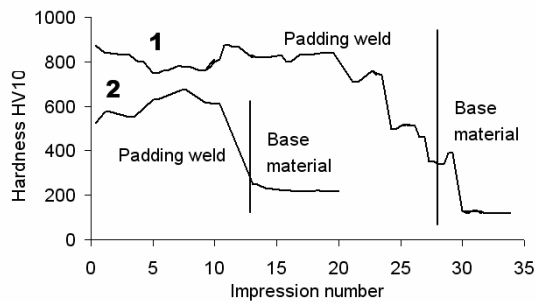
Fig. 23. [6]. Hardness profile in a three-layer padding welds:
1 – CN-O padding weld, 2 – EP3600H24V9 padding weld

In Figure 23, curve no. 1 presents the most frequently observed changeability of the padding welds hardness. The hardness has the tendency (as in Figure 21) to decrease when approaching the weld penetration zone. Curve no. 2, however, is a negative example, because as early as at the beginning of service the wear out rate will be high. It should decrease in the process of surface layers wear out, but it does not have to be the case in the presence of macro- and microscopic defects.

Summarizing, one can state that hardness measurements confirm the results of microscopic examinations and they constitute a measure of reliable forecast of the padding welds service behaviour.

5. Abrasive resistance of padd welded layers – examples

Papers [10, 14] present the results of studies on abrasive resistance for ten padding welds selected from those presented in Table 1. The tests were performed with the application of Haworth's device. Sandy gravel, medium clay and silty soil were used as abrasive materials. The humidity of the abrasive materials equalled 3.5% for medium clay and 5% for gravel and silty soil. Measurement distances of 2, 4, 8 and 10 km were set, and the average mass loss was calculated based on five tests. In order to illustrate the separate behaviour of the selected padding welds in a specific abrasive environment, the article presents only the results of tests made for padding welds DP11G12, DIPS-9 and EN600-B. Diagrams (Figures 24–26) compare also the abrasive wear out results for steel 38GSA. This results from the fact that the material (after thermal treatment) was used for the lining subjected to abrasive wear out. Such a presentation of the issue in the diagrams enables the evaluation of application efficiency of pad welded layers as a method of improving their resistance to the abrasive wear out. It also reveals that the thesis saying that 'there has not been elaborated any universal padding weld (electrode for pad welding) giving satisfactory effects in various abrasive environments' is true.
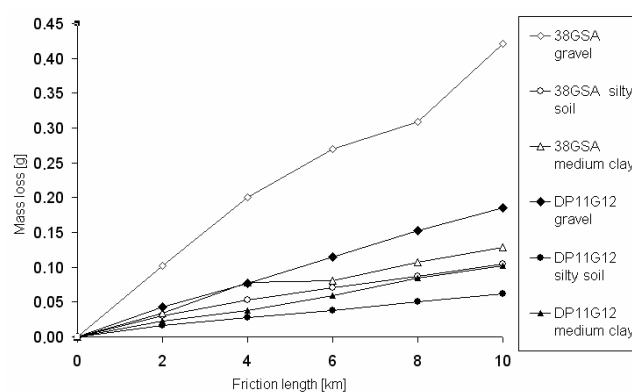
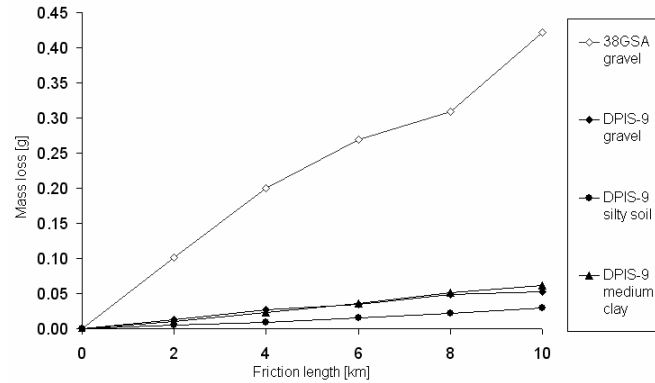

Fig. 24. Average mass loss [10, 14]
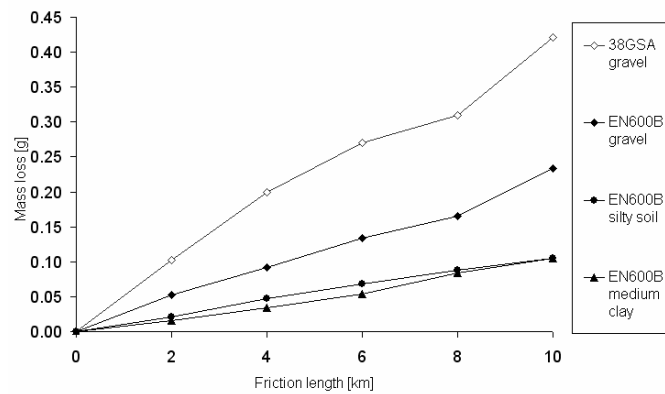
Fig. 25. Average mass loss [10, 14]

Fig. 26. Average mass loss [10, 14]

From Figures 24–26 it can be concluded that the application of each padding weld resulted in leap decrease in the abrasive wear out (mass loss). In the most difficult environment of gravel, the highest efficiency of all the examples presented had padding weld made with electrode DIPS-9. As compared to the two other abrasive environments (Figures 24–25) such a decisive statement is unwarranted.

6. Conclusions

The article presents and characterizes the types of macroscopic and microscopic defects appearing in padding welds. Moreover, the qualitative comparison of their structures and hardness changes accompanied by the forecast of service durability have been made. As the article has a character of a review it does not seem purposeful to include the enumeration and hierarchical order of the analyzed macro- and micro-

scopic features in the conclusions. Thus, the conclusions contain reflections and solutions resulting from many years of studies devoted to the padding welds. One of the reflections states that the elaboration of quantitative assumptions can be made (padding weld and base material defectiveness) for determined, possibly wide applications, for example for padding welds used in lignite excavating machines (as a basis for defining industry standards).

It should be stressed that chemical compositions of electrodes for pad welding are selected on the basis of prior service experiments and engineering intuition, applying the basic rules of material selection. In paper [15], it has been proved that an average engineer has a detailed knowledge of practical application of 50–100 engineering materials. Their real number (over 100000 currently available on the market) requires making choices on the basis of multicriteria optimization, i.e. applying the rules of material designing. The collected experience (including our own) can be a basis for the design of a system of material selection for pad welding. The system can help to reduce the number (over 50) of specific features of the material considered in material designing process. For example, the issue of the presence of primary carbides in the padding weld can be considered. It has just been proved that primary carbides can contribute to low service durability (cracks on the interphase boundaries, cracking of the carbides themselves – and as a consequence – their chipping instead of abrasive wear out, or the presence of primary carbides only in the surface layer of the padding weld). In our opinion, there is a possibility of designing an electrode which can be used for obtaining pad welded layers with the characteristics of padding welds with primary carbides of a considerably simpler chemical composition (in comparison with e.g. electrode Castolin XHD 6715 or CN-O) and equilibrium eutectic structure. Such solutions have already been offered but they have not caught the interest of our domestic industry. Naturally, it is not possible to design a universal electrode but electrodes designed for specific work conditions.

The application of pad welding processes can be limited in the forthcoming years. This is connected with the works carried out by the authors of the article concerning Hardox type steel [16]. The steel is produced in five varieties and combines high abrasive resistance with high durability and resistance to dynamic loads. The application of Hardox steel enables also the reduction in the weight and simplification of the construction compared to current solutions with pad welded layers. One type of the steel (Hardox 400) has been used instead of the pad welded plates of non-alloy steel for bucket wheel chutes of Polish construction in lignite excavators built for India. The process of the material wear out is monitored and compared with service behaviour of pad welded layers.

References

[1] Wojtkun F., Sołncew J.P.: *Materiały specjalnego przeznaczenia*, Wyd. Politechniki Radomskiej, Radom, 1999.

[2] Gierek A., Bajka L.: *Żeliwo stopowe jako tworzywo konstrukcyjne*, Wyd. Śląsk, Katowice, 1976.

[3] Pękalska L., Pękalski G.: *Budowa fazowa i struktury napoin stosowanych w górnictwie węgla brunatnego*, Węgiel Brunatny, Special Edition, 2000.

[4] Alenowicz J., Mendel S., Pękalski G.: *Badanie napoin drutem rdzeniowym Lincore 40-O stosowanym do regeneracji członów gąsienicowych koparek i zwałowarek*, Górnictwo Odkrywkowe, 2004, No. 1, pp. 29–32.

[5] Alenowicz J., Mendel S., Pękalska L.: *Badania metalograficzne napoin wykonanych drutem proszkowym Lincore 15CrMn*, Górnictwo Odkrywkowe, 2004 (paper to be published).

[6] Pękalski G., Dudziński W., Haimann K., Pękalska L., Sachadel U.: *Badania metalograficzne napoiny twardej wykonanej drutem CN-O firmy Welding Poland na bandażach i misie układu mielącego młyna RP-1043X*, Raport Instytutu Materiałoznawstwa i Mechaniki Technicznej Politechniki Wrocławskiej, 2003, No. 1.

[7] Pękalski G., Dudziński W., Haimann K., Pękalska L., Sachadel U.: *Ocena stopnia degradacji materiału rodzimego elementów układu mielącego młyna węglowego RP-1043X*, Raport Instytutu Materiałoznawstwa i Mechaniki Technicznej Politechniki Wrocławskiej, 2003, No. 2.

[8] Pękalska L., Pękalski G., Sachadel U.: *Makroskopowe i mikroskopowe czynniki trwałości napoin*, Proc. Conf. PIRE 2001, 2001, pp. 185–194.

[9] Haimann R., Dudziński W., Haimann K., Moll R.: *Zęby czerpaków koparek – przegląd rodzajów materiałów, przyczyny uszkodzeń*, Raport Instytutu Materiałoznawstwa i Mechaniki Technicznej Politechniki Wrocławskiej, 1994, No. 11.

[10] Pękalski G., Napiórkowski J., Pękalska L., Kamińska A.: *Napoiny o złożonej strukturze a zużywanie w masie ściernej*, Raport Instytutu Materiałoznawstwa i Mechaniki Technicznej Politechniki Wrocławskiej, 1997, No. 6.

[11] Pękalski G., Sobis T., Stram T., Widanka K.: *Makro- i mikroskopowe cechy struktur napoin Fe-Cr-C i Fe-Cr-C-V*, Proc. II Conf. *Metody Doświadczalne w Budowie i Eksploatacji Maszyn*, 1995, pp. 181–188.

[12] Bungart K., Kunze E., Horn E.: *Untersuchungen über den Aufbau des Systems Eisen-Chrom-Kohlenstoff*, Arch. f. Eisenhüttenweisen, 1958, No. 3.

[13] Kowalski M., Spencer P., Granat K., Drzeniek H., Lugscheider E.: *Phase relations in the C-Cr-Fe systems in the vicinity of the (liquid + bcc + $M_{23}C_6$, M_7C_3) invariant equlibrium – experimental determinations and thermodynamic modeling*, MetalKunde, 1995, 85, H5.

[14] Napiórkowski J., Pękalska L., Pękalski G.: *Structure of metal and its wear resistance in the soil*, Tribologia, 1998, No. 6, pp. 871–879.

[15] Dobrzański L.A.: *Podstawy nauki o materiałach i metaloznawstwo*, Materiały inżynierskie z podstawami projektowania materiałowego, WN-T, Warszawa, 2002.

[16] Capanidis D., Konat Ł., Pękalski G., Wieleba W.: *Możliwości zastosowania stali Hardox a ich struktury i wybrane właściwości*, Problemy Maszyn Roboczych, styczeń–luty 2005 (paper to be published).

Makro- i mikrostrukturalne aspekty trwałości warstw napawanych

Przedstawiono wyniki badań makroskopowych, mikroskopowych, pomiarów twardości i zużywania ściernego warstw napawanych wykonywanych z użyciem trzydziestu dziewięciu

gatunków elektrod do napawania. Przedmiotem szczególnego zainteresowania było powiązanie problemu wadliwości tych warstw z przewidywanym przebiegiem ich zużywania. Wskazano na możliwość znaczącego uproszczenia składów chemicznych elektrod (uproszczenia składu fazowego napoin) na podstawie prognozowania ich budowy wypływającej z analizy stosownych wykresów równowagi fazowej oraz struktur w stanie wyżarzonym. W pracach badawczych skoncentrowano się na warstwach napawanych wykorzystywanych w górnictwie węgla brunatnego i energetyce.